

THE DESIGN AND DEVELOPMENT OF AN ANTHROPOMORPHIC
CORONARY ARTERY NETWORK PHANTOM

To assist in the development and validation of novel imaging-related technologies

B. Huegen

THE DESIGN AND DEVELOPMENT OF AN ANTHROPOMORPHIC CORONARY ARTERY NETWORK PHANTOM

To assist in the development and validation of novel imaging-related technologies

By

B. Huegen

Master thesis in partial fulfilment of the requirements for the degree of

Master of Science
In Biomedical Engineering

At Delft University of Technology,
to be defended publicly on Tuesday, June 4 2024, at 1:00 PM.

Supervisors:

Prof. dr. J.J. van den Dobbelsteen

TU Delft

Prof. dr. B.H.W. Hendriks

TU Delft & Philips

An electronic version of this thesis is available at repository.tudelft.nl



ABSTRACT

Percutaneous coronary intervention (PCI) is one of the main medical procedures employed for the treatment of coronary artery disease. During this procedure, the coronary arteries are visualized using X-ray imaging. However, it only generates 2D images which can complicate several tasks, including assessing the lesion and correctly placing a stent. To overcome this limitation, researchers of Philips Research are developing technologies that allow the implementation of 3D imaging data derived from coronary CT angiography in the catheterization laboratory. Throughout the development, a coronary artery network phantom could serve as a beneficial tool. Such a phantom should be anthropomorphic and have realistic imaging and mechanical properties. Additionally, it should serve as a platform on which a basic PCI procedure can be performed. No commercially or academically developed phantom satisfies these criteria, thus the objective for this project was to design and develop an anthropomorphic coronary artery network phantom with realistic imaging and mechanical properties, which can be used to mimic both healthy and atherosclerotic human coronary arteries.

A material study was initially conducted to find the most suitable materials for the development of the phantom. During the first stage, the radiodensity of several materials was measured. Based on those results, and other factors such as safety, usability and durability, it was concluded that PlatSil Gel 25 would be used for the development of the arterial wall. Additionally, the heart and non-calcified lesions were to be made from VytaFlex 20 in combination with BaSO₄. The calcified lesions were to be made from PlatSil Gel 25 and also required the addition of BaSO₄ to increase their radiodensity. After the imaging tests, uniaxial tensile tests were conducted to measure the stiffness of PlatSil Gel 25 samples with different concentrations of PlatSil hardener. These results demonstrated that PlatSil Gel 25 has a comparable stiffness to that of healthy human coronary arteries in the longitudinal direction. When combined with the hardener, it can also mimic the stiffness of atherosclerotic coronary arteries.

After the material study, the coronary artery network phantom was designed and developed. The design comprises a simplified representation of the heart, and an arterial network that consists of the coronary artery network and a simplified representation of the arterial pathway distal to the aortic root. To manufacture the arterial network, a water-soluble 3D-printed mould was manually coated with PlatSil Gel 25 and subsequently dissolved in water. Due to the solubility of the mould, it was possible to manufacture a geometrically complex and hollow arterial network as a single part. Additionally, it was demonstrated that this manufacturing method can be used to include lesions within the arterial wall, and that its stiffness can be locally changed.

During the evaluation of the final phantom, its geometrical, imaging and mechanical properties were assessed and compared with the formulated requirements. Based on the results it can be concluded that the phantom meets many of the requirements. Furthermore, it was demonstrated that a guidewire can be inserted into the arterial network and manipulated up to the end of the left circumflex artery. Nevertheless, the evaluation also revealed some areas of improvement. Most notable are the improvements related to the imaging properties of the phantom. For example, the radiodensity of the arterial wall was slightly too high. In addition, the attenuation was not uniform throughout the parts of the phantom that contained BaSO₄, as was evident from X-ray and CT images.

In conclusion, this project demonstrated that the utilized manufacturing method and materials can be used to develop a healthy and atherosclerotic coronary artery network phantom, that possesses realistic geometrical, imaging and mechanical properties. Additionally, it has the potential to serve as a platform on which a basic PCI procedure can be performed. Nevertheless, several areas of improvement related to both the manufacturing method and phantom remain, which might form the foundation for a future project.

TABLE OF CONTENTS

ABSTRACT	II
LIST OF TABLES.....	IV
LIST OF FIGURES	V
LIST OF ABBREVIATIONS	VI
1. INTRODUCTION	1
2. DESIGN REQUIREMENTS.....	2
General	2
Imaging.....	2
Geometrical.....	3
Mechanical	4
Programme of requirements	5
3. PART I: MATERIAL STUDY	7
Material selection.....	7
Imaging properties	7
Mechanical properties.....	15
Conclusion	18
4. PART II: PHANTOM DESIGN AND DEVELOPMENT.....	19
Related studies	19
Conceptual design	20
Development of the coronary artery network phantom	21
Discussion	27
Conclusion	28
5. PART III: PHANTOM EVALUATION	29
General	29
Imaging.....	30
Geometrical.....	32
Mechanical	34
Discussion.....	35
Conclusion	36
6. DISCUSSION.....	37
7. CONCLUSION	39
REFERENCES	40
APPENDIX	44
Definitions of the arterial segments.....	44
Data processing script – uniaxial tensile test.....	45
Preliminary literature review.....	47

LIST OF TABLES

Table 1. Overview of the radiodensity of myocardium found in the literature.	2
Table 2. Overview of the required lumen diameter for different segments of the main arteries in the coronary artery network.	3
Table 3. Overview of the wall thickness of the LAD found in the literature.....	4
Table 4. Overview of the cardiac dimensions found in the literature.	4
Table 5. The acquisition parameters used during the preliminary imaging test.....	8
Table 6. The radiodensities of unenhanced cubic and cylindrical samples, made from Mold Max 30, VytaFlex 20, PlatSil Gel 25 and Dragon Skin 20.	11
Table 7. An overview of the additives, including the concentrations, that were used during the development of the final phantom.	30
Table 8. Results of the imaging test, conducted to assess the effect of certain additives on the radiodensity of PlatSil Gel 25 and VytaFlex 20.	31
Table 9. The required and actual radiodensity of the different parts of the phantoms.	32
Table 10. Overview of the required and actual lumen diameter of the different arterial segments of the final phantom.....	33
Table 11. The required and actual dimensions of the heart	34
Table 12. Results of the uniaxial tensile test, conducted to assess the effect of a colorant on the elastic modulus of PlatSil Gel 25.....	35
Table 13. Definitions of the arterial segments present in the final phantom based on Dodge et al. (1992), and a comparison with the reporting system of the American Heart Association (AHA).....	44

LIST OF FIGURES

Figure 1. An illustration that explains the partial volume effect.	8
Figure 2. The setup used for the preliminary imaging test.	9
Figure 3. A graph showing the relationship between the NaCl concentration of a solution and its radiodensity. The equation of the trendline: $y = 0.91x - 10.17$	9
Figure 4. The cubic and hollow cylindrical samples used during the unenhanced material test.	11
Figure 5. A graph that displays the relationship between the BaSO ₄ concentration and the radiodensity of samples made from VytaFlex 20. The equation of the trendline: $y = 15.4x - 51.0$	13
Figure 6. A graph that displays the relationship between the BaSO ₄ concentration and the radiodensity of samples made from PlatSil Gel 25. The equation of the trendline: $y = 14.2x + 218.4$	14
Figure 7. CT image of the contrast-enhanced PlatSil Gel 25 samples, illustrating the uneven attenuation throughout the individual samples. The concentrations of BaSO ₄ within the samples increases from left to right.	14
Figure 8. Overview of the setup used during the uniaxial tensile test.	15
Figure 9. A graph that displays the relationship between the output of the load cell and the applied tensile force.	16
Figure 10. A graph that displays the relationship between the hardener concentration and the elastic modulus of samples made from PlatSil Gel 25. The equation of the trendline: $y = 0.43x + 0.30$	17
Figure 11. The coronary artery phantoms of Mørup et al. (2022) and Stepniak et al. (2019), illustrated in the left and right image respectively.	19
Figure 12. A conceptual design of the final phantom.	20
Figure 13. Progression from the original to the final 3D model of the coronary artery network.	21
Figure 14. An overview of the arteries included within the coronary artery network. Note that this model still contained the septal perforating artery, however this branch was not included in the final phantom.	22
Figure 15. The progression of the arterial network from individual 3D-printed parts to a complete anthropomorphic network.	23
Figure 16. The progression of the heart from the original 3D model to the cast version.	24
Figure 17. Connecting the arterial network to the heart.	25
Figure 18. Overview of the four atherosclerotic phantoms.	26
Figure 19. Two X-ray images of the cannulated phantom. The guiding catheter was inserted up to the ostium of the LCA and the guidewire was subsequently advanced to the end of the LCx.	29
Figure 20. An overview of the sites within the coronary artery network at which the lumen diameters were measured.	33

LIST OF ABBREVIATIONS

AHA	American Heart Association
BaSO₄	Barium sulphate
CA	Cyanoacrylate
CBCT	Cone beam computed tomography
D	Diagonal artery
HU	Hounsfield unit
LAD	Left anterior descending artery
LCA	Left coronary artery
LCx	Left circumflex artery
LMA	Left marginal artery
MDCT	Multidetector computed tomography
NaCl	Sodium chloride
PCI	Percutaneous coronary intervention
PDA	Posterior descending artery
PVA	Polyvinyl alcohol
RCA	Right coronary artery
RMA	Right marginal artery
VOI	Volume of interest

1. INTRODUCTION

Coronary artery disease is one of the leading causes of mortality worldwide (Brown et al., 2024). During the progression of the disease, plaque typically accumulates within the tunica intima of the arterial wall. This process is commonly known as atherosclerosis and will lead to stenosis or a complete occlusion of the lumen. Since the coronary arteries are responsible for supplying the myocardium with oxygen, a significant reduction in the lumen size could result in myocardial ischemia. Percutaneous coronary intervention (PCI) is one of the main medical procedures to revascularize the coronary arteries. Between 2013 and 2017, approximately 3 million of these procedures were performed in the United States alone (Inohara et al., 2020). This shows the importance and extent to which this minimally invasive procedure is utilized.

The primary objective of PCI is to dilate a stenosed or open an occluded coronary artery. There are several medical techniques that could be utilized during the procedure, but the most common ones are balloon angioplasty and stenting. In order to visualize the coronary artery network, either single-plane or bi-plane X-ray imaging is utilized in combination with contrast injections. This imaging procedure is commonly known as coronary angiography. One of the major limitations associated with this procedure is that it can only generate 2D images. This can complicate several tasks, including assessing the lesion, correctly placing the stent and guiding the medical equipment, which in turn can increase the risk of adverse events after stent implantation (Campbell et al., 2015; Collet et al., 2021). To overcome this limitation, researchers from the Image Guided Therapy and Ultrasound Devices & Systems department of Philips Research are developing technologies that allow the implementation of 3D imaging data derived from coronary CT angiography in the catheterization laboratory.

Throughout the development and validation of these novel technologies, a coronary artery network phantom could serve as a beneficial tool. The use of such a phantom would reduce the use of animal and human tissue, providing a more ethical alternative. Furthermore, it could provide a controlled and standardized testing environment. It is important that such a phantom is anthropomorphic and mimics both the imaging and mechanical properties of in vivo human tissue. Additionally, it should serve as a platform on which a basic PCI procedure can be performed. To the best of the author's knowledge and those involved in the project, there is currently no commercially available phantom that satisfies the aforementioned criteria. As for academically developed phantoms, the one made by Stepniak et al. (2019) could be considered the most advanced phantom, but still has several limitations. As a result, the following objective has been formulated for this project:

Design and develop an anthropomorphic coronary artery network phantom with realistic imaging and mechanical properties, that can be used to mimic both healthy and atherosclerotic human coronary arteries.

The main purpose of this phantom is to aid the development and validation process of the novel technologies that are developed by researchers of Philips Research. Additionally, the phantom might be a beneficial tool for other researchers and developers, or serve as a training tool for medical students.

2. DESIGN REQUIREMENTS

This chapter will provide an overview of the design requirements used for the development of the coronary artery network phantom. The requirements were formulated through literature study and consultations with researchers from Philips Research. They are categorized as general, imaging, geometrical and mechanical requirements. Additionally, a distinction has been made between mandatory and optional requirements. All imaging and geometrical requirements are considered to be mandatory, since the primary purpose of the phantom is to serve as a tool for the development of imaging-related technologies. If possible, the phantom should also have realistic mechanical properties, especially if it is used as a platform on which a basic PCI procedure is performed. However, when compromises between requirements need to be made, the mechanical properties are considered to be less important and therefore optional.

GENERAL

In consultation with a few researchers from Philips Research it was determined that the phantom should at least consist of an aortic root, both coronary arteries and the two main branches of the left coronary artery (LCA), that is, the left anterior descending artery (LAD) and the left circumflex artery (LCx). Optionally, the phantom could include branches of the right coronary artery (RCA), LAD and LCx. Furthermore, a simplified representation of the heart and the arterial pathway distal to the aortic root should be included. The arterial pathway distal to the aortic root will be used to introduce medical equipment into the arterial network. The heart can act as a support structure for the coronary artery network and enhances the realism of generated medical images. Since the phantom also has to serve as a platform on which a basic PCI procedure (i.e., coronary angioplasty followed by stenting) can be performed, the arterial network should be hollow, watertight and allow the insertion of a guidewire into one of the coronary arteries. Testing and evaluation of the phantom might take place at a different location from where it is manufactured. As a result, the phantom should also be transportable and have a shelf life of at least one month.

IMAGING

X-ray-based imaging techniques are commonly employed during PCI. Thus, the arterial network and heart should match the degree of X-ray attenuation found in corresponding human tissues. Additionally, non-calcified and calcified lesions might be included into the phantom. These should also have a radiodensity comparable to that found in vivo. Prior to this project, a literature review was conducted in which the imaging and mechanical properties of human coronary arteries were evaluated. The literature review is included within this report and can be found in the appendix. Based on the findings of this review, the radiodensity, expressed as a Hounsfield unit (HU), for non-calcified (i.e., lipid-rich and fibrous lesions) and calcified lesions should be between 34 to 106 HU and 377 to 1160 HU respectively. It is important to note that the results for lipid-rich and fibrous lesions have been combined into one group (i.e., non-calcified lesions), since no decisive conclusion was reached regarding the significance in the difference between their radiodensities.

Table 1. Overview of the radiodensity of myocardium found in the literature.

Study	Sample size	Radiodensity [HU]
Nikolaou et al. (2004)	23	117 ± 28
Nieman et al. (2006)	13	73 ± 14
Okuma et al. (2014)	33	36.8 ± 6.2

Data is presented as mean ± SD.

The cardiac wall consists predominantly of myocardium. Therefore, the radiodensity of the myocardium will serve as a requirement for the whole heart. Table 1 provides an overview of the found literature. All included studies conducted their measurements at a tube potential of 120 kV, which is in line with the inclusion criteria of the preliminary literature review. Based on the mean results of the studies, the radiodensity of the heart should be between 37 and 117 HU.

Literature on the radiodensity of the arterial walls of healthy coronary arteries is very limited. During the preliminary literature study, no literature was found that met the inclusion criteria. Despite this, it is known that coronary arteries are difficult to differentiate from their surrounding (i.e., mainly myocardial tissue) on X-ray and CT images (Stepniak et al., 2019). The imaging requirement for the arterial walls will therefore be the same as for the heart. This range is also in accordance with the results of Mørup et al. (2022) and Clouse et al. (2008), although both studies did not use a tube potential of 120 kV during their measurements.

GEOMETRICAL

In order to ensure that the phantom closely resembles the shape of the tissues found in vivo, the design of the coronary artery network and heart should be based on 3D reconstructions from medical images. However, this requirement does not ensure that the different elements of the phantom are also properly sized. Therefore, additional requirements for the lumen diameter, arterial wall thickness and dimensions of the heart have been formulated. All these requirements are formulated as ranges, which are defined by a mean value \pm two standard deviations as found in the literature. Table 2 presents the required lumen diameter for different segments of the main arteries in the coronary network. These ranges are based on the results of Dodge et al. (1992). This study was chosen due to its extensive measurements and clear description of the results. Furthermore, a relatively high degree of accuracy and repeatability were observed within the study. Table 10 in the ‘Phantom evaluation’ chapter also contains the requirements for any optional branches included in the final phantom. The exact descriptions used to define each arterial segment are provided in the appendix.

Table 2. Overview of the required lumen diameter for different segments of the main arteries in the coronary artery network.

Segment	Lumen diameter [mm]
Right coronary artery	
RCA – 1	2.7 – 5.1
RCA – 2	2.4 – 4.4
RCA – 3	2.1 – 4.1
RCA – 4	1.2 – 3.2
Left coronary artery	
LCA	3.5 – 5.5
Left anterior descending artery	
LAD – 1	2.6 – 4.6
LAD – 2	1.5 – 3.5
LAD – 3	0.7 – 2.7
Left circumflex artery	
LCx – 1	2.4 – 4.4
LCx – 2	1.6 – 4.0
LCx – 3	0.4 – 2.8

*The ranges are based on the mean ($\pm 2*SD$) results for normal men with right cardiac dominance at the middle of each segment, as can be seen in table 6 of Dodge et al. (1992).*

The arterial wall thickness varies throughout the coronary artery network. Mimicking this in a phantom presents many difficulties during the development phase. The complete network will therefore have a single uniform wall thickness. Based on the results of Perry et al. (2013), the arterial wall should be between 0.7 and 1.5 mm thick. During this study, the wall of the LAD was measured in 227 subjects, all of whom were free of clinical coronary artery disease, hypertension, hyperlipidemia and diabetes mellitus. Additionally, the study showed a high degree of repeatability and the results corresponded well with those of Perry et al. (2008) and Gradus-Pizlo et al. (2001), as can be seen table 3.

Table 3. Overview of the wall thickness of the LAD found in the literature.

Study	Sample size	Wall thickness [mm]
Perry et al. (2013)	227	1.1 ± 0.2^1
Perry et al. (2008)	50	1.2 ± 0.3
Gradus-Pizlo et al. (2001)	29	0.9 ± 0.1

¹The requirement for the arterial wall thickness is based on this data.
Data is presented as mean \pm SD.

Only two studies were found that measured the length, breadth and thickness of the human heart. Both of these studies, Sultana et al. (2011) and Gupta et al. (2014), were conducted in South Asia on local subjects. It is important to take into account that Europeans are on average taller and heavier than people from South Asia, and that both weight and height have a significant effect on the cardiac dimensions (Pfaffenberger et al., 2013; Rodriguez-Martinez et al., 2020). To compensate for these differences, the requirement for each dimension is based on the largest mean value from the aforementioned studies. The length of the heart should therefore be between 92.3 and 132.7 mm, the breadth between 64.4 and 111.2 mm and the thickness between 48.6 and 74.2 mm.

Table 4. Overview of the cardiac dimensions found in the literature.

Study	Sample size	Length [mm]	Breadth [mm]	Thickness [mm]
Sultana et al. (2011)	38	96.2 ± 9.6	79.4 ± 7.8	61.4 ± 6.4^1
Gupta et al. (2014)	46	112.5 ± 10.1^1	87.8 ± 11.7^1	39.7 ± 11.7

Only the data for male donors is included in this table, since their hearts were larger than that of the female donors. ¹The requirements for the dimensions of the heart are based on these data.
Data is presented as mean \pm SD.

MECHANICAL

There are many mechanical properties that could be mimicked during the development of a phantom. However, this project focuses solely on the elastic modulus in the longitudinal and circumferential direction of the coronary arteries. The elastic modulus quantifies the relationship between the stresses applied during a medical procedure and the strain of the arterial wall. Therefore, it is a suitable mechanical property for a phantom that should also serve as a platform on which a basic PCI procedure can be performed. During the preliminary literature review, the elastic modulus of healthy and atherosclerotic human coronary arteries was evaluated. Based on these results, the elastic modulus in longitudinal direction of healthy and atherosclerotic human coronary arteries ranged from 0.28 to 2.94 MPa and from 0.40 to 5.63 MPa respectively. The elastic modulus in circumferential direction of both healthy and atherosclerotic coronary arteries ranged from 0.78 to 1.68 MPa and 1.13 to 4.11 MPa respectively. To mimic a realistic mechanical behaviour, the utilized tissue mimicking material should fall within one of these ranges.

PROGRAMME OF REQUIREMENTS

MANDATORY REQUIREMENTS

GENERAL

- The phantom should at least include the following structures:
 - Right coronary artery
 - Left coronary artery
 - Left anterior descending artery
 - Left circumflex artery
 - Aortic root
 - A simplified representation of the arterial pathway distal to the aortic root
 - A simplified representation of the heart
- The arterial network should be hollow.
- The arterial network should be watertight.
- The phantom should allow for the insertion of a guidewire into a coronary artery.
- The phantom should be transportable.
- The phantom should have a shelf life of at least one month.

IMAGING

- The radiodensity, expressed as a Hounsfield unit, of non-calcified lesions (i.e., lipid-rich and fibrotic lesions) should be between 34 to 106 HU.
- The radiodensity of calcified lesions should be between 377 to 1160 HU.
- The radiodensity of the heart should be between 37 and 117 HU.
- The radiodensity of the arterial wall should be between 37 and 117 HU.

GEOMETRICAL

- The design of the coronary artery network and heart should be based on 3D reconstructions from medical images.
- The lumen diameter for healthy segments of the main arteries of the coronary artery network should fall within the ranges presented in table 10.
- The arterial wall thickness for healthy segments of the coronary artery network should be between 0.7 and 1.5 mm.
- The heart should correspond with the following dimensions:
 - The length should be between 92.3 and 132.7 mm.
 - The breadth should be between 64.4 and 111.2 mm.
 - The thickness should be between 48.6 and 74.2 mm.

OPTIONAL REQUIREMENTS

GENERAL

- The phantom includes branches of the right coronary artery, the left circumflex artery and the left anterior descending artery, with realistic geometrical properties.

MECHANICAL

- The elastic modulus of the utilized material should be between 0.28 and 2.94 MPa, for a phantom that mimics the mechanical properties of healthy human coronary arteries in the longitudinal direction.
- The elastic modulus of the utilized material should be between 0.4 and 5.63 MPa, for a phantom that mimics the mechanical properties of atherosclerotic human coronary arteries in the longitudinal direction.
- The elastic modulus of the utilized material should be between 0.78 and 1.68 MPa, for a phantom that mimics the mechanical properties of healthy human coronary arteries in the circumferential direction.
- The elastic modulus of the utilized material should be between 1.13 and 4.11 MPa, for a phantom that mimics the mechanical properties of atherosclerotic human coronary arteries in the circumferential direction.

3. PART I: MATERIAL STUDY

The final phantom should meet the imaging requirements and preferably also the mechanical requirements as formulated in the previous chapter. A material study was conducted to find the most suitable materials for developing the phantom. During the first stage, the imaging properties of several materials were measured. Based on these results and other important factors, such as safety, usability and durability, several materials were selected for the development of the lesions, the heart and the arterial network of the phantom. The second stage focuses solely on measuring the mechanical properties of the material that will be used to develop the arterial wall. All the materials selected for this material study are either available in different stiffnesses, or can have their stiffness adjusted with an additive. Based on the results of the mechanical test, a conclusion can be drawn on whether the stiffness of the selected material can be adjusted to meet the mechanical requirements.

MATERIAL SELECTION

The two main types of materials that were tested are silicone and polyurethane. These are generally tougher and more durable when compared to other tissue mimicking materials such as agar, gelatine and PVA. This is an important consideration, since the coronary artery phantom would otherwise become too fragile. According to literature, the radiodensity of a solid block of silicone can be relatively high (Jin et al., 2022; O'Reilly et al., 2020; Steinmann et al., 2018). However, Stepniak et al. (2019) showed that the radiodensity of a hollow cylindrical sample (i.e. samples that mimic coronary arteries) could meet the requirement for the arterial wall, due to the partial volume effect. Based on the results of Jin et al. (2022), O'Reilly et al. (2020) and Steinmann et al. (2018), the radiodensity of polyurethane was expected to be near the lower end of the required range for the arterial wall. Furthermore, both silicone and polyurethane are available in a wide range of stiffnesses. This increased the chance that the mechanical requirements could be met.

The specific materials chosen for the material study were PlatSil Gel 25 and Dragon Skin 20 (both platinum-cured silicones), Mold Max 30 (a tin-cured silicone) and VytaFlex 20 (a polyurethane rubber). These were selected since they are either part of product series that are available in a wide range of different stiffnesses, or their stiffness can be adjusted using an additive. However, based on the technical data provided by the manufacturer, it was estimated that the stiffness of the chosen materials should already be near the required mechanical ranges. Furthermore, the materials are all commonly used at the lab where the phantom is developed. This made them suitable options for this project.

IMAGING PROPERTIES

The first stage of this material study is divided into the following three imaging tests:

- Preliminary imaging test
- Unenhanced material test
- Contrast-enhanced material test

During the preliminary imaging test, the radiodensity of different concentrations of sodium chloride (NaCl) solutions were measured. The results of this test were used to create a suitable environment for further testing, and to determine whether such a solution can mimic contrast-enhanced blood. The unenhanced material test was used to measure the radiodensity of the four selected materials, both as solid cubes and hollow cylinders. Finally, the contrast-enhanced material test was used to measure the radiodensity of one or more materials, in combination with an additive used to increase its X-ray attenuation. Such a contrast-enhanced material is at least necessary for replicating the radiodensity of calcified lesions, which demonstrate a high degree of X-ray attenuation.

PRELIMINARY IMAGING TEST

Due to the small size of the coronary arteries and limited spatial resolution of certain medical imaging devices, an effect can occur known as the partial volume effect. This effect occurs when multiple tissues or materials contribute to the same voxel and needs to be considered when testing the hollow cylindrical samples during the unenhanced material test. Figure 1 illustrates the partial volume effect. Due to this effect, the cylindrical samples need to be tested in an environment that has a similar radiodensity as found in vivo. The arterial wall is mostly enclosed by blood and the myocardium. Based on the results of Hagita et al. (2022) and Okuma et al. (2014), it can be concluded that a radiodensity of 40 HU could serve as a simplified representation of such an environment. The results of Nygren (2021) show that a NaCl solution can be used to replicate the radiodensity of this environment. Additionally, a completely saturated NaCl solution might be able to mimic the attenuation of contrast-enhanced blood. This would be an easy to obtain and cheap alternative that can be used in combination with the phantom, instead of an iodine contrast agent. Thus, the aim of this test is to find the relationship between the concentration of a NaCl solution and its radiodensity.

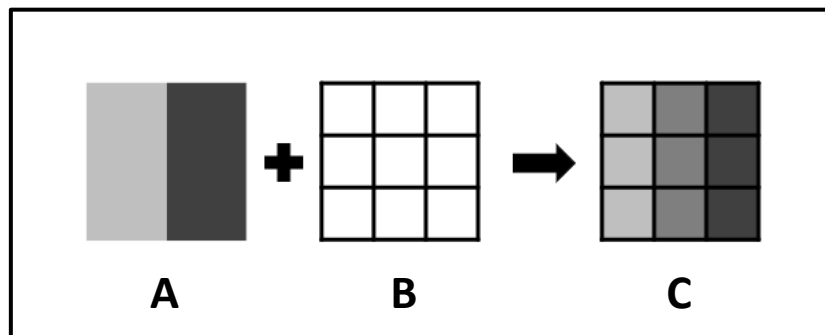


Figure 1. An illustration that explains the partial volume effect. (A) The actual radiodensity of the scanned object. (B) A 9x9 pixel grid, resembling the limited resolution of medical imaging devices. (C) The radiodensity as seen on a medical image. The radiodensities displayed in the pixels of the first and third column are true to the actual values. However, the second column displays an averaged radiodensity, due to the fact that two tissues with different radiodensities contribute to these pixels.

METHOD

In total, eight different NaCl solutions were made by dissolving extra fine pure table salt (JOZO salt) into demineralised water (Albert Heijn B.V.). The solutions ranged from 0 up to 350 g NaCl per litre demineralised water and increased in steps of 50 g. Next, a single 30 ml plastic cup was filled for each NaCl solution and placed in a 3D-printed holder. This holder was then placed inside of a CT-phantom. Cone beam CT (CBCT) images of this setup were acquired using the Azurion 7 M20 image-guided therapy system (Koninklijke Philips N.V.). Table 5 provides an overview of the acquisition parameters.

Table 5. The acquisition parameters used during the preliminary imaging test.

Acquisition parameters	Value
Tube potential	120 kV
Exposure	≈ 1250 μAs
Cine rate	30
Spatial resolution	0.648 x 0.648 x 0.648 mm

The images were analysed using 3D Slicer (www.slicer.org). A spherical volume of interest (VOI) of at least 1 cm³ was placed in the centre of each cup, away from the edges. The mean radiodensity of each VOI was rounded to the nearest integer and used for further analyses.

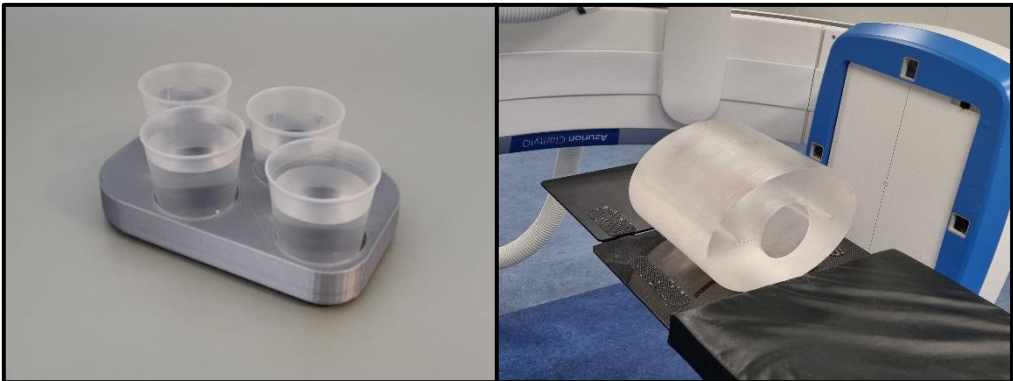


Figure 2. The setup used for the preliminary imaging test. (Left) Four different NaCl solutions placed inside of a holder. (Right) The CT-phantom placed at the isocentre of the C-arm of the Azurion 7 M20.

RESULTS

Figure 3 presents the measured radiodensity of the different NaCl solutions. Each datapoint represents the mean radiodensity of the spherical VOI placed in the centre of the cups. The graph also includes a linear trendline that is a best-fit for the data.

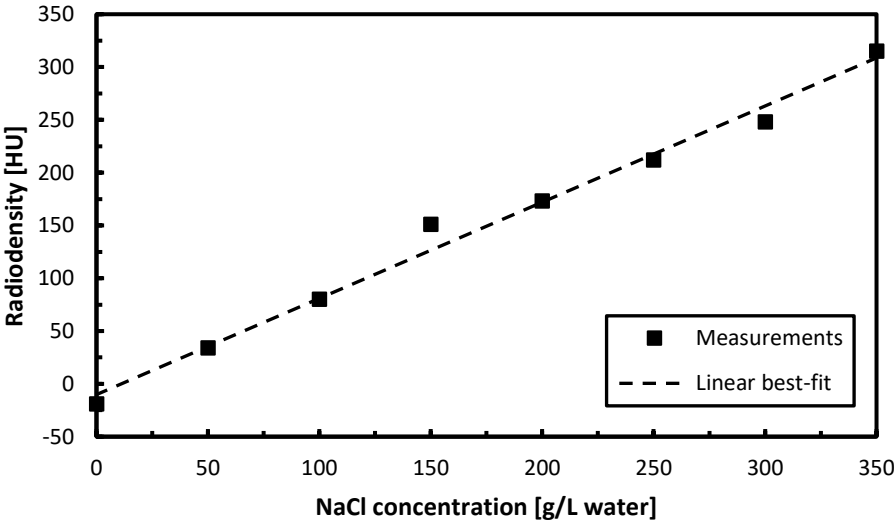


Figure 3. A graph showing the relationship between the NaCl concentration of a solution and its radiodensity. The equation of the trendline: $y = 0.91x - 10.17$.

DISCUSSION

The aim of the preliminary imaging test was to find the relationship between the concentration of a NaCl solution and its radiodensity. Based on the results it can be calculated that a NaCl solution of 55 g per litre demineralised water should have a radiodensity of approximately 40 HU. Therefore, such a solution can be used as a testing environment during the unenhanced material test of hollow cylindrical samples. Furthermore, an almost saturated NaCl solution (i.e., 350 g per litre water) has a mean radiodensity of 309 HU. During the preliminary literature study, it was found that the mean and median radiodensities within the contrast-enhanced coronary lumen across the included studies ranged from 276 to 364 HU. Based on these results it can be concluded that a NaCl solution can indeed be used to mimic the radiodensity of contrast-enhanced blood.

An important limitation of this test is the use of a CBCT scan to measure the radiodensities. Generally, a multidetector CT (MDCT) scan is considered the gold standard for such measurements (Silva et al., 2012; Yadegari et al., 2023). This is due to the fact that data obtained through CBCT are associated with a greater variability and therefore less reliable than those obtained with an MDCT scanner (Pauwels et al., 2015). Different studies, such as the one conducted by Razi et al. (2014) and Kamaruddin et al. (2016), do show a strong correlation between the data derived from CBCT and MDCT. Additionally, both studies also concluded that there was no significant difference between the data. However, the study conducted by Silva et al. (2012) did find a significant difference between the data derived from CBCT and MDCT. Since this project was limited to the use of CBCT, a comparison can be made with existing literature as an initial validation of the results. The obtained results are relatively similar to those of Nygren (2021), which is promising. Nevertheless, it is still recommended to validate the results using MDCT when possible.

UNENHANCED MATERIAL TEST

The aim of the unenhanced material test is to measure the radiodensity of the four selected materials. Both solid cubes and hollow cylinders (i.e. samples mimicking the coronary arteries) were measured during this test. Due to the small size of the cylindrical samples, the partial volume effect will have an influence on the results. This effect also occurs when measuring the radiodensity of real coronary arteries and should therefore be considered during the measurements. However, it also introduces a lot of variability. For example, factors such as the wall thickness of the samples, voxel selection and radiodensity of the environment all start to influence the results. The larger volume of the solid cubes allows for the determination of a mean radiodensity, without the influence of the partial volume effect. Thus, these measurements have a higher degree of reproducibility. Since both the measurements of the hollow cylindrical samples and solid cubes have their respective benefits, the results of the two were used to draw conclusions regarding the material selection.

METHOD

The following four materials were selected for this test:

- PlatSil Gel 25 (Polytek Development Corp.)
- Dragon Skin 20 (Smooth-On, Inc.)
- Mold Max 30 (Smooth-On, Inc.)
- VytaFlex 20 (Smooth-On, Inc.)

For each of these materials, five solid cubes and three hollow cylindrical samples were cast according to the instructions provided by the manufacturer. The cubes were 25 x 25 x 25 mm and cast using a 3D-printed mould. A vacuum chamber was used to remove any air from the uncured materials. The cylindrical samples have a uniform inside diameter of 4.5 mm and a target wall thickness of 1.1 mm.

These samples were made according to the same method employed for the development of the final phantom. The ‘Phantom design and development’ chapter explains this process in detail. Two hundred drops¹ SilTone Fresh Blood colorant (FormX B.V.) per kilo silicone were added to the cylindrical samples made from PlatSil Gel 25 and Dragon Skin 20. Ten drops EPTone Red colorant (FormX B.V.) and 30 g Aerosil thickener (FormX B.V.) per kilo polyurethane were added to the cylindrical samples made from VytaFlex 20. No additives were added to the samples made from Mold Max 30.

After casting, the cubes were placed onto a 3D-printed holder and the cylindrical samples were suspended in a container filled with a NaCl solution. This solution contained 55 g NaCl per litre demineralised water. Both setups were then placed inside of a CT-phantom. CBCT images of these two setups were acquired using the same imaging system and acquisition parameters that were used during the preliminary imaging test.

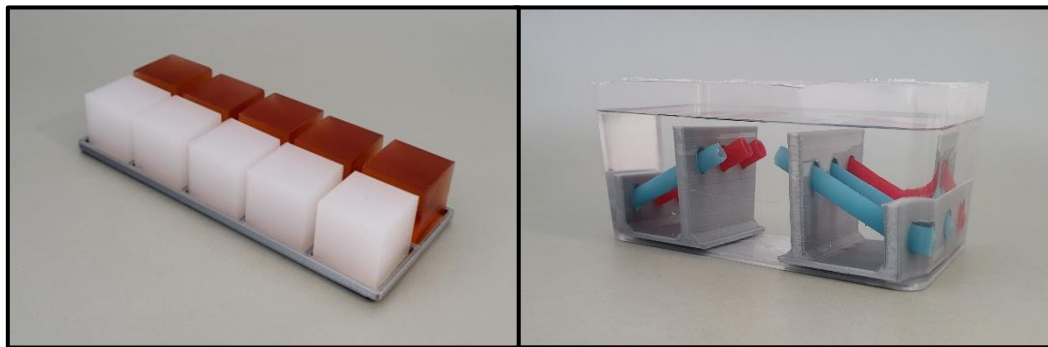


Figure 4. The cubic and hollow cylindrical samples used during the unenhanced material test.

The images were analysed using 3D Slicer. For the cubic samples, a spherical VOI of at least 1 cm³ was placed in the centre of each cube, away from the edges. The mean radiodensity of each VOI was rounded to the nearest integer and used for further analyses. For the cylindrical samples, 10 individual voxels located in the wall were selected per sample. The radiodensity of each voxel was rounded to the nearest integer and used for further analyses.

RESULTS

Table 6 presents the results for the unenhanced material test. The results of the cubic samples are based on the measurements of 5 VOI’s per material, while those of the cylindrical samples are based on the measurements of 30 individual voxels per material.

Table 6. The radiodensities of unenhanced cubic and cylindrical samples, made from Mold Max 30, VytaFlex 20, PlatSil Gel 25 and Dragon Skin 20.

Material	Radiodensity [HU]	
	Cubic samples	Cylindrical samples
Mold Max 30	264 ± 14	232 ± 19
VytaFlex 20	-48 ± 9	-27 ± 11
PlatSil Gel 25	191 ± 13	168 ± 26
Dragon Skin 20	179 ± 12	152 ± 15

Data is presented as mean ± SD.

¹ The amount of colorant is expressed in drops, since the actual quantity used, was too small to be accurately weighed.

DISCUSSION

The aim of the unenhanced material test was to measure the radiodensity of the four selected materials. The results for the solid cubic samples are rather similar to the results of Jin et al. (2022), O'Reilly et al. (2020) and Steinmann et al. (2018), both in terms of absolute values as well as how the values of the different materials relate to each other. This is a promising indication of the validity of the results in this study. Furthermore, the radiodensity of the cylindrical samples made from Mold Max 30, PlatSil Gel 25 and Dragon Skin 20, all decreased compared to the results of their solid cubic counterparts. In contrast, the radiodensity of the cylindrical samples made from VytaFlex 20 increased. This result was to be expected, because of the partial volume effect and the radiodensity of the environment compared to that of the samples.

Some of the materials required additional additives in order to facilitate the manufacturing process of the cylindrical samples. For this test, it was assumed that the additives did not have a significant effect on the radiodensity of the materials. The results appear to support this assumption. However, it should be validated during the evaluation of the final coronary artery phantom.

None of the materials directly meet the imaging requirements for the arterial wall (i.e., a radiodensity between 37 and 117 HU). One option could be to use VytaFlex 20 in combination with an additive that increases its radiodensity. However, VytaFlex 20 also required an additional thickening agent and colorant when casting the hollow cylindrical samples. Furthermore, it has a long curing time and requires additional safety measures during casting, due to the potential health hazards. All these factors complicate the manufacturing process of the phantom drastically. Therefore, VytaFlex 20 will not be used for the development of the arterial network. Nevertheless, it can be used for the heart and non-calcified lesions, since the manufacturing process of these parts will be much less complicated. However, the radiodensity of the unenhanced VytaFlex 20 is too low to mimic the required imaging properties of the heart and non-calcified lesions (i.e. a radiodensity between 37 to 117 HU and 34 to 106 HU respectively). Thus, the material should be combined with an additive that increases its X-ray attenuation.

From the three remaining materials, Dragon Skin 20 has a radiodensity closest to the imaging requirement for the arterial wall. However, the difference between PlatSil Gel 25 and Dragon Skin 20 is small and the curing time of the former is considerably shorter. This makes PlatSil Gel 25 the more desirable option for the arterial wall. An additive could be used to decrease the radiodensity of PlatSil Gel 25, until it matches the imaging requirement for the arterial wall. However, it was decided to not use such an additive, due to the concern that this would make the coronary artery phantom too fragile. PlatSil Gel 25 will also be used to mimic the calcified lesions. The radiodensity of the unenhanced material is too low to meet the imaging requirement for calcified lesions, so the material should be combined with an additive that increases its X-ray attenuation.

CONTRAST-ENHANCED MATERIAL TEST

Based on the results of the previous test, it was concluded that VytaFlex 20 will be used to develop the heart and non-calcified lesions, and PlatSil Gel 25 for development of the calcified lesions. However, the radiodensity of both materials needs to be increased in order to meet the imaging requirements for the respective parts of the phantom. Barium sulphate (BaSO_4) is chosen for this purpose, since it is commonly used as a contrast agent for radiological examinations. In addition, it is occasionally used as an additive for the development of imaging phantoms, as shown by different studies, including those conducted by Litt & Brody (2001) and Lai et al. (2022). The aim of this test is to measure the radiodensity of contrast-enhanced VytaFlex 20 and PlatSil Gel 25.

METHOD

For each of the selected materials, five solid cubes with different concentrations of BaSO₄ (Thermo Fisher Scientific Inc.) were cast. The VytaFlex 20 samples ranged from 0.0 up to 10.0 g BaSO₄ per kilo polyurethane and increased in steps of 2.5 g. The PlatSil Gel 25 samples ranged from 0.0 up to 60.0 g BaSO₄ per kilo silicone and increased in steps of 15.0 g. The BaSO₄ was sieved once before adding it to the materials.

After curing, the cubes were positioned onto a 3D-printed holder and this setup was then placed inside of a CT-phantom. CBCT images of this setup were acquired using the same imaging system and acquisition parameters that were used during the preliminary imaging test.

The images were analysed using 3D Slicer. A spherical VOI of at least 1 cm³ was placed in the centre of each cube, away from the edges. The mean radiodensity of each VOI was rounded to the nearest integer and used for further analyses.

RESULTS

Figure 5 and 6 present the measured radiodensity of contrast-enhanced VytaFlex 20 and PlatSil Gel 25 respectively. Each datapoint in the graphs represents the mean radiodensity of the VOI placed in the centre of one cubic sample. Both graphs also include a linear trendline that is a best-fit for the data.

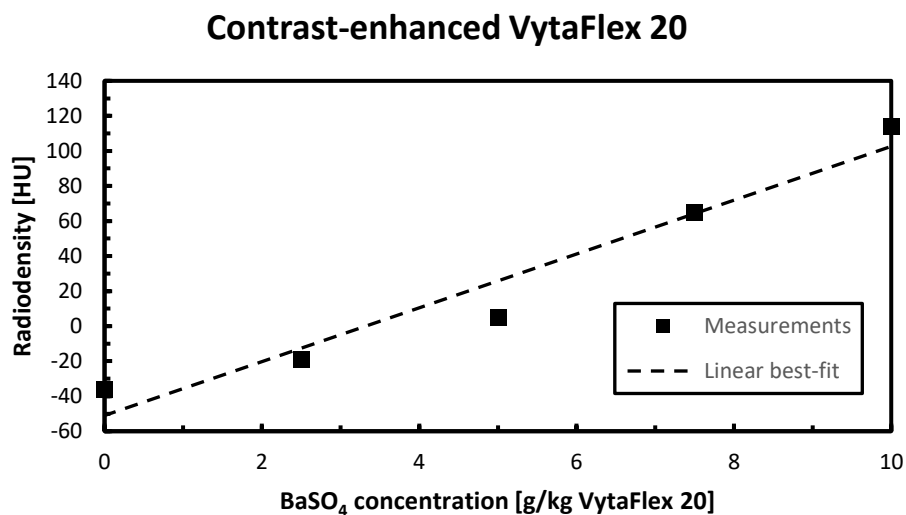


Figure 5. A graph that displays the relationship between the BaSO₄ concentration and the radiodensity of samples made from VytaFlex 20. The equation of the trendline: $y = 15.4x - 51.0$.

Contrast-enhanced PlatSil Gel 25

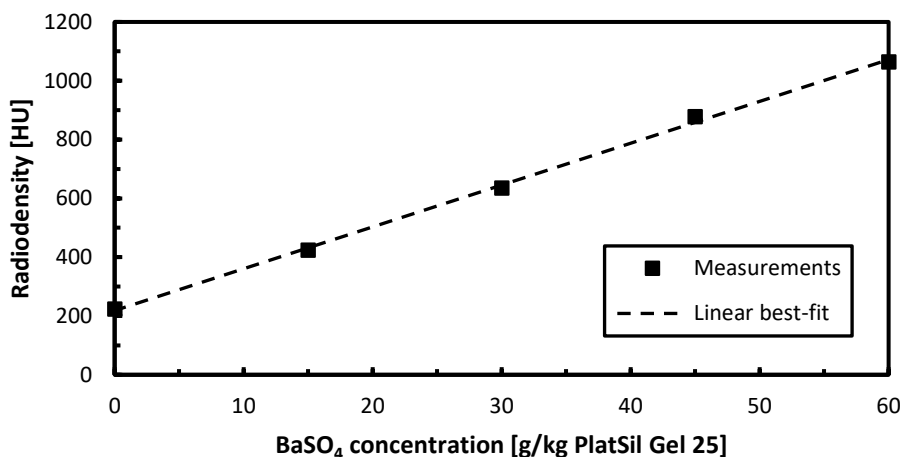


Figure 6. A graph that displays the relationship between the BaSO₄ concentration and the radiodensity of samples made from PlatSil Gel 25. The equation of the trendline: $y = 14.2x + 218.4$.

DISCUSSION

The aim of this test was to measure the radiodensity of contrast-enhanced VytaFlex 20 and PlatSil Gel 25. Based on the results it was concluded that contrast-enhanced VytaFlex 20 can be used to mimic imaging properties of the heart and non-calcified lesions (i.e. a radiodensity between 37 to 117 HU and 34 to 106 HU respectively). Contrast-enhanced PlatSil Gel 25 could be used to mimic the radiodensity of calcified lesions (i.e. between 377 and 1160 HU). However, it is important to note that the attenuation was not uniform throughout the individual samples, as can be seen in figure 7. This could be due to the fact that the BaSO₄ grains were still too large and unevenly dispersed throughout the samples, leading to an uneven concentration in each voxel. Extra care should be taken to prevent this during the development of the final phantom.

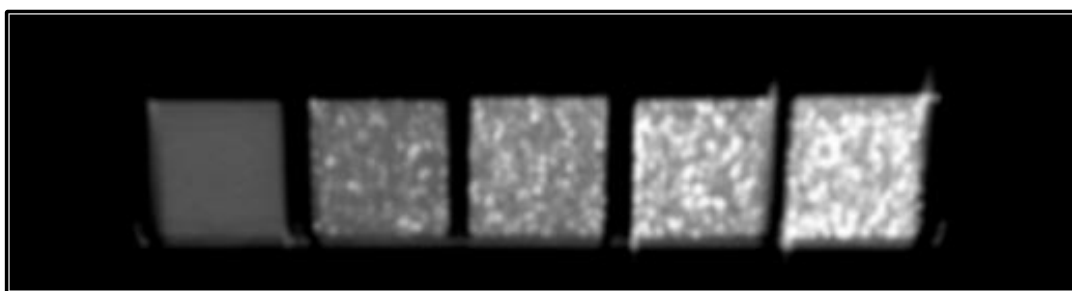


Figure 7. CT image of the contrast-enhanced PlatSil Gel 25 samples, illustrating the uneven attenuation throughout the individual samples. The concentrations of BaSO₄ within the samples increases from left to right.

MECHANICAL PROPERTIES

The previous part of this material study, focused on measuring the imaging properties of different materials. Based on the results, it was concluded that PlatSil Gel 25 will be used for the development of the arterial network. Preferably, the arterial wall should also meet the mechanical requirements as formulated in the previous chapter. During this part of the material study, the elastic modulus of PlatSil Gel 25 in combination with different concentrations of hardener will be measured. The results of this test were used to conclude whether the stiffness of PlatSil Gel 25 can be altered to meet the various mechanical requirements.

UNIAXIAL TENSILE TEST

A uniaxial tensile test was conducted, in order to measure the stiffness of PlatSil Gel 25 in combination with different concentrations of hardener. Dumbbell shaped samples were used during the measurements, since these can be cast with much less geometrical variability than hollow cylindrical shaped samples (i.e. samples that resemble arteries). Furthermore, it is assumed that no additive used for the development of the final phantom, apart from the hardener, has a significant effect on the stiffness of the PlatSil Gel 25 samples. This assumption should be validated after the development of the final phantom.

METHOD

Five dumbbell shaped samples were cast for each of the different concentrations of PlatSil hardener (Polytek Development Corp.). The concentrations ranged from 0 up to 500 g hardener per kilo PlatSil Gel 25 and increased in steps of 125 g. All tensile samples were cast using a 3D-printed mould, which dimensions corresponded to those of a type 1 dumbbell sample as stated by the ISO standard 37:2017 (*Rubber, vulcanized or thermoplastic – Determination of tensile stress-strain properties*). The minimum time between curing and testing was 16 hours, as recommended by the same ISO standard.

After fully curing, the samples were attached to a linear stage (Aerotech, Inc.) using a custom-made 3D-printed setup, as shown in figure 8. A 2 lbs load cell (FUTEK Advanced Sensor Technology, Inc.) was used to measure the forces applied to the tensile samples. This load cell was calibrated before the start of the measurements, using nine weights with a known mass. Figure 9 displays the calibration curve. The samples were slightly pre-tensioned, until any slack was removed. Each sample was then stretched up to 12.5 mm at a rate of 6 mm/min.

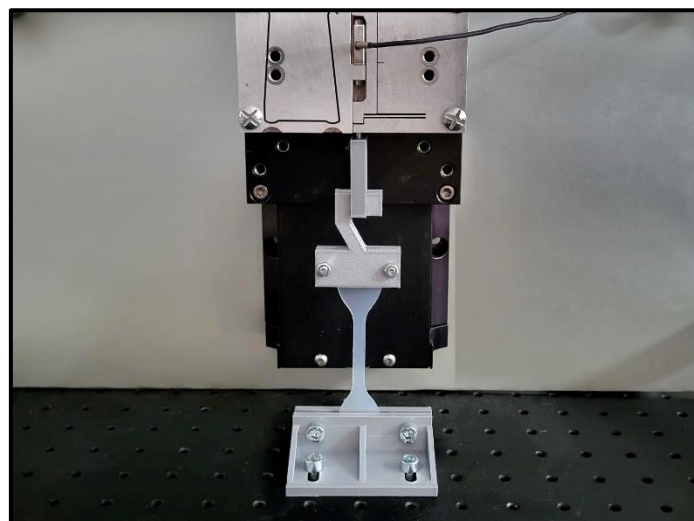


Figure 8. Overview of the setup used during the uniaxial tensile test.

MATLAB (The MathWorks, Inc.) was used to process the data obtained through the uniaxial tensile tests. The scripts are included in the appendix. A moving average filter was first applied to the force data of each measurement. Next, the true stress and true strain were calculated. The initial linear region of this true stress-strain curve (i.e. up to a true strain of 0.1) was then approximated by a first degree polynomial, which best fits the data in a least-squares sense. The slopes of the linear polynomials represent the elastic modulus of the samples and are used for further analyses of the data.

RESULTS

Figure 9 presents the calibration curve for the 2 lbs load cell used in the uniaxial tensile tests. Each datapoint represents the output of the load cell at a known tensile force. Based on these nine measurements, a linear relationship was established between the output of the load cell and the applied tensile force.

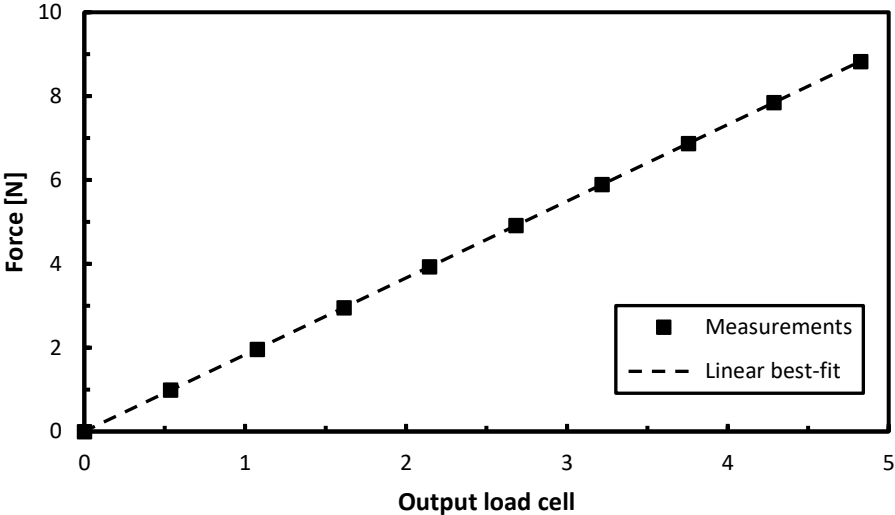


Figure 9. A graph that displays the relationship between the output of the load cell and the applied tensile force.

Figure 10 presents the measured elastic modulus of PlatSil Gel 25 samples with different concentrations of hardener. Each datapoint represents the mean elastic modulus calculated from five samples with similar concentrations of hardener.

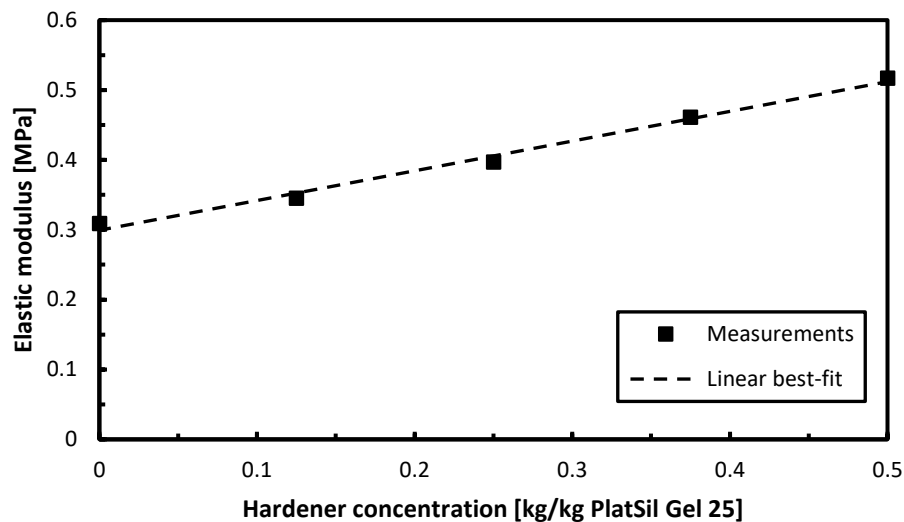


Figure 10. A graph that displays the relationship between the hardener concentration and the elastic modulus of samples made from PlatSil Gel 25. The equation of the trendline: $y = 0.43x + 0.30$.

DISCUSSION

In order to mimic the stiffness of healthy human coronary arteries in the longitudinal direction, the elastic modulus of the material should be between 0.28 and 2.94 MPa. Since PlatSil Gel 25 without hardener has an elastic modulus of 0.30 MPa, it can be concluded that it meets this requirement. To mimic the stiffness of atherosclerotic coronary arteries in the longitudinal direction, the elastic modulus of the material should be between 0.40 and 5.63 MPa. By combining PlatSil Gel 25 with the hardener, an elastic modulus of up to 0.51 MPa can be achieved, which meets this requirement. However, according to the manufacturer, the maximum concentrations of hardener used during these measurements should not be exceeded. It is therefore not possible to meet the imaging requirements for healthy and atherosclerotic coronary arteries in the circumferential direction, since these start at 0.78 and 1.13 MPa respectively. Furthermore, it is unknown whether the addition of the hardener changes the radiodensity of PlatSil Gel 25 significantly. For now, it is assumed that this is not the case. Nevertheless, it should be validated during the final evaluation of the phantom.

During the calculations of the elastic modulus, the strain was defined by the initial length and deformation of the narrow portion of the dumbbell shaped samples. However, this deformation was not directly measured. Only the displacement of the linear stage was directly measured, which corresponds to the deformation of the entire dumbbell shaped sample. Nevertheless, the displacement of the linear stage was used as an approximation for the deformation of the narrow portion of the samples. The justification was based on the fact that most of the deformation would indeed occur in this section instead of the wider ends, due to the higher local stresses. As a result of this approximation, the strain in the narrow portion of the samples is overestimated. This is a limitation of the measurement method and results in an underestimation of the actual elastic modulus.

CONCLUSION

During this material study, the imaging and mechanical properties of different materials and solutions have been measured. Based on the results, it was concluded that VytaFlex 20 in combination with BaSO₄ will be used for the development of the heart and non-calcified lesions, while PlatSil Gel 25 will be used to develop the arterial network and calcified lesions. However, for the calcified lesions, BaSO₄ needs to be added to make the material more radiopaque. Additionally, a NaCl solution can be used to mimic the radiodensity of regular and contrast-enhanced blood.

Uniaxial tensile tests were employed to measure the stiffness of PlatSil Gel 25 samples with different concentrations of hardener. The results demonstrated that PlatSil Gel 25 without hardener mimics the stiffness of healthy human coronary arteries in the longitudinal direction. If combined with a hardener, it can also be utilized to mimic the stiffness of atherosclerotic coronary arteries in the longitudinal directions. However, PlatSil Gel 25 cannot be used to mimic the elastic modulus of healthy and atherosclerotic coronary arteries in the circumferential direction, since it cannot be made stiff enough.

Throughout the development of the final phantom, additives might be used to facilitate the manufacturing process. For now, it is assumed that any additive besides BaSO₄ does not have a significant effect on the radiodensity of the materials. Additionally, it is assumed that any additive besides the hardener does not have a significant effect on the elastic modulus. These assumptions need to be validated during the final evaluation of the coronary artery phantom.

4. PART II: PHANTOM DESIGN AND DEVELOPMENT

This chapter describes the manner in which the final phantom is designed and developed. First, a short overview is provided of other studies that have developed coronary artery phantoms. This section discusses the main manufacturing methods employed by these studies. In addition, it identifies the manufacturing method most suited for the current study and outlines which changes will be made to improve upon this method. After that, the conceptual design of the phantom is presented. This concept is based on the requirements and provides an initial visual representation of the phantom and its various components. During the project it was used to communicate the idea with researchers from Philips Research and acted as a foundation for the final design. Finally, the development of the coronary artery network phantom is described in detail, followed by a discussion which mainly emphasizes future improvements to the manufacturing process.

RELATED STUDIES

Based on current literature, it appears that there are two main manufacturing methods employed for developing coronary artery phantoms. The phantom is either directly 3D printed using a flexible material, or a mould of the coronary arteries is printed and coated using a brush-on or dipping technique. Stepniak et al. (2020), Russ et al. (2015), Sommer et al. (2020) and Shepard et al. (2019) all tried to 3D print a coronary artery phantom, with varying degrees of success. Stepniak et al. (2020) employed several 3D-printing technologies, namely fused deposition modelling, stereolithography and PolyJet. The best result was acquired using stereolithography, although this still required the phantom to be printed piecewise. The three other studies were all able to 3D print a coronary artery phantom as a single part using the PolyJet technology. However, this printing technology was not available during this project. Furthermore, only a limited selection of materials is available for 3D printing and the properties of these materials cannot be altered using additives. It was therefore decided not to 3D print the phantom directly.

Chanda & Curry (2018), Mørup et al. (2022) and Stepniak et al. (2019) all 3D printed a mould of the coronary arteries and they coated this using a brush-on or dipping technique. Currently, the phantoms developed by Mørup et al. (2022) and Stepniak et al. (2019) appear to be the most advanced among those created using this manufacturing method. However, the LCA and RCA of these phantoms are not directly connected to each other. Additionally, no arterial pathway distal to the aortic root is included. It is therefore not possible to introduce medical equipment into these phantoms in a realistic manner. These limitations in the design of the phantoms likely stem from the fact that the mould needs to be removed after casting. In order to overcome these design limitations, a water-soluble 3D-printed mould will be used for the development of the current phantom. Contrary to the non-soluble moulds used by the other studies, a soluble mould should be relatively easy to remove, independent from the complexity of the final design.

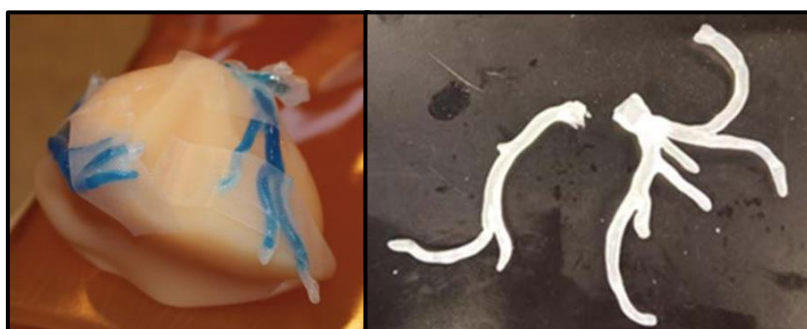


Figure 11. The coronary artery phantoms of Mørup et al. (2022) and Stepniak et al. (2019), illustrated in the left and right image respectively.

CONCEPTUAL DESIGN

The design consists of three parts, namely:

1. The coronary artery network
2. The simplified representation of the arterial pathway distal to the aortic root
3. The simplified representation of the heart

The coronary artery network and the arterial pathway distal to the aortic root should be hollow and connected to each other to form a closed arterial network. Medical equipment, such as a guidewire, can be introduced into this network through the pathway distal to the aortic root. The simplified heart should be a solid body representation of the four chambers and surrounding myocardium. The superior vena cava, pulmonary artery and pulmonary vein are excluded from this simplified representation. The heart will act as a support structure for the coronary artery network and enhances the realism of generated medical images.

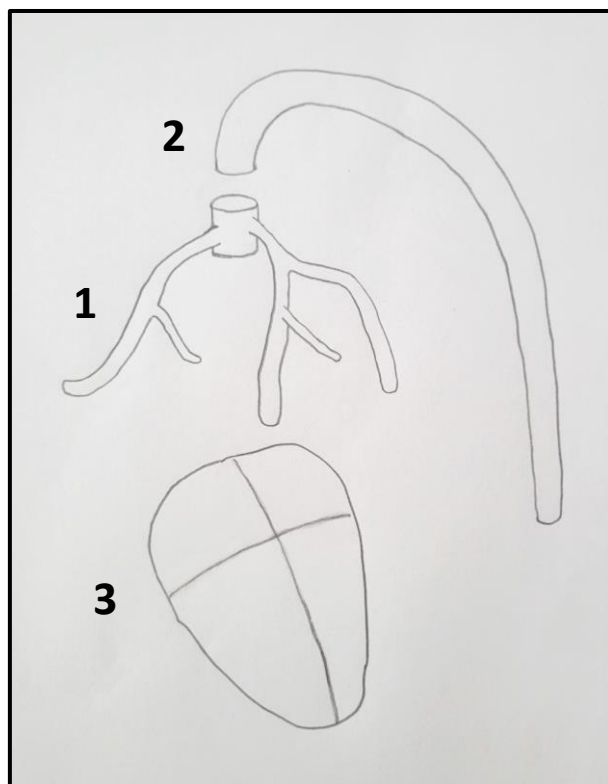


Figure 12. A conceptual design of the final phantom. (1) The coronary artery network. (2) The arterial pathway distal to the aortic root. (3) The heart.

DEVELOPMENT OF THE CORONARY ARTERY NETWORK PHANTOM

The development of the coronary artery network phantom was divided into three stages. First, the arterial network was developed. This arterial network consists of both the coronary artery network and the pathway distal to the aortic root. During the next stage, a heart was designed and cast. Finally, both parts had to be connected in order to finalize the phantom. This final phantom represents a healthy individual without atherosclerosis. In order to demonstrate whether these design and manufacturing methods can also be used to develop an atherosclerotic coronary artery phantom, four additional smaller phantoms were made. These smaller atherosclerotic phantoms either include a non-calcified or a calcified lesion, all located at different sites within the phantom. Furthermore, one atherosclerotic phantom was made with a stiffer silicone surrounding the lesion. This is to demonstrate whether it is possible to make a phantom which locally mimics the elastic modulus of atherosclerotic human coronary arteries in the longitudinal direction.

THE ARTERIAL NETWORK

The design of the coronary artery network is entirely based on a 3D model, which was reconstructed using CT scans of human coronary arteries. This 3D model was obtained through the database of Atlas of Human Cardiac Anatomy, University of Minnesota (www.vhlab.umn.edu/atlas). The database contained various models of the coronary arteries, all originating from different donors. Model 0109 was selected for this project, since the donor did not have any known cardiac conditions and had right cardiac dominance. The latter is important, since some of the geometrical requirements are also based on donors with right cardiac dominance. Additionally, all major arteries were present and the model was of high quality. Figure 13-A displays the original model. After selecting the model, it was refined using Meshmixer (Autodesk, Inc.). First, any mesh defects were repaired. After that, irrelevant branches were removed from the model to decrease its complexity, see figure 13-B. Finally, the entire surface was smoothed. The diameter of the coronary arteries decreased due to this smoothing operation, which was corrected for by extruding them in the normal direction. Figure 13-C displays the refined model and figure 14 provides an overview of the arteries included in the final coronary network. To preserve the general shape of the coronary artery network, no additional changes were made. After refining the model of the coronary arteries, a simplified aorta was designed using SolidWorks (Dassault Systèmes SolidWorks Corp.). The diameter of the aorta was determined by the distance between the RCA and LCA in the refined model. The shape was based on educational and medical images.

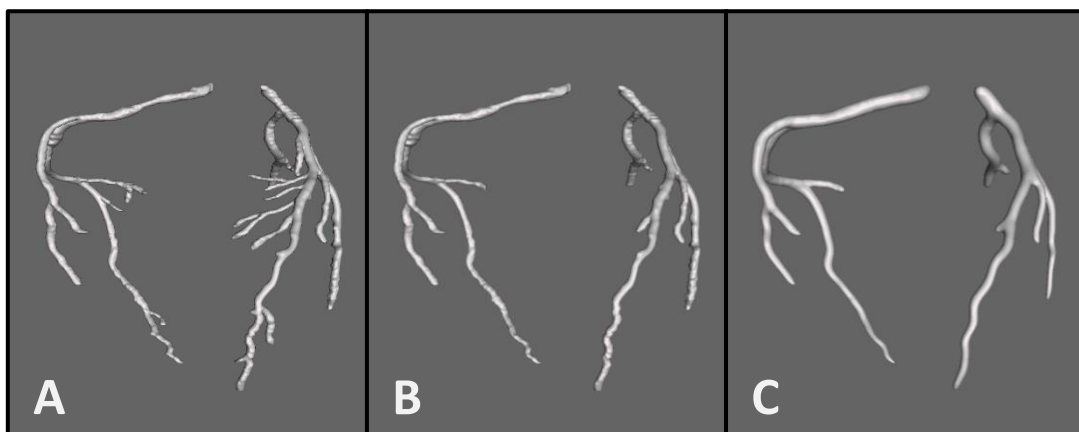


Figure 13. Progression from the original to the final 3D model of the coronary artery network. (A) The original model which was obtained through the database of Atlas of Human Cardiac Anatomy, University of Minnesota (www.vhlab.umn.edu/atlas). (B) The model after removing irrelevant branches. (C) The final model of the coronary artery network.

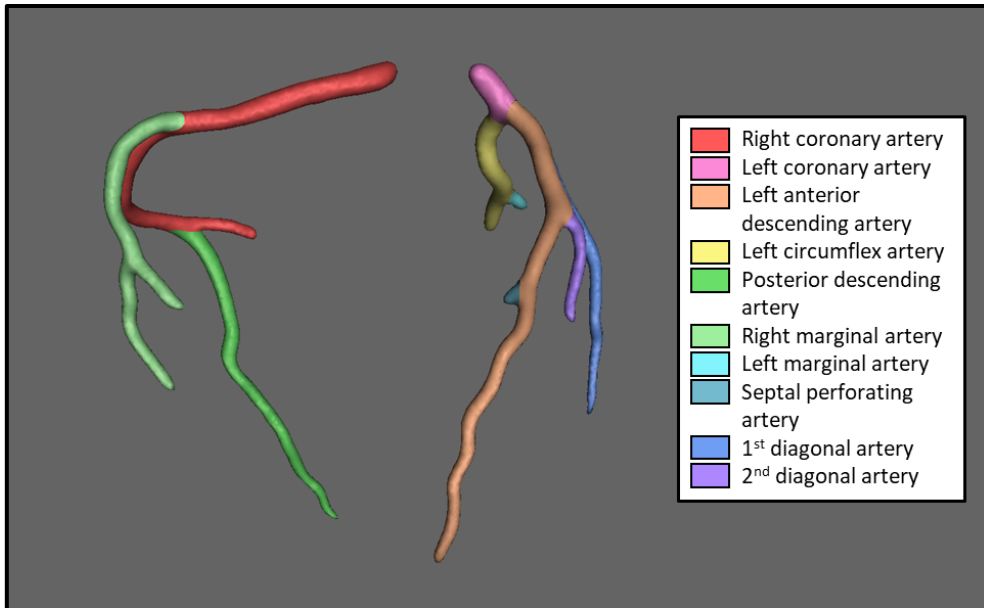


Figure 14. An overview of the arteries included within the coronary artery network. Note that this model still contained the septal perforating artery, however this branch was not included in the final phantom.

Once the complete arterial network was designed, it had to be 3D printed using a water-soluble filament, namely Ultrafuse BVOH (BASF 3D Printing Solutions GmbH). Printing with this type of filament is generally quite difficult, especially considering the complexity and intricacy of the arterial network. In order to successfully print the model, it was necessary to take several measures. First, a climate chamber was built to store the water-soluble filament. Due to its properties, the filament can easily absorb moisture from the air, which negatively impacts the printing quality. Using a climate chamber, it was possible to store the filament at a relative humidity of less than 20%. This prevented the filament from absorbing any significant amounts of moisture from the air. Next, the use of support during printing had to be minimized. Minimal support would not only result in better surface quality, but also reduces the chance of breaking the 3D-printed parts when removing the support. To accomplish this, custom tree support structures were generated using Meshmixer. Lastly, the model of the arterial network had to be printed piecewise. This results in a better printing quality and reduces the amount of support needed during printing.

All parts of the arterial network were printed on an UltiMaker S3 (Ultimaker B.V.). UltiMaker Cura 5.5.0 (Ultimaker B.V.) was used to slice the individual parts. A regular printing profile for generic PVA was used for slicing, which automatically configures the printing parameters. However, the infill density for all parts was adjusted to 100%. After printing, all support was carefully removed and the surfaces were smoothed using a fine sandpaper. The parts were then further smoothed, by dissolving a thin layer of the material with water, and dried in a custom climate chamber for at least 24 hours. Figure 15-A displays the individual 3D-printed parts of the arterial network after refinement. Once the individual parts were completely dry, they were glued together using Loctite 401 cyanoacrylate (CA) glue (Henkel KGaA). The arterial network was left to dry for 1 hour outside of the climate chamber, as CA glue cures upon exposure to moisture in the air. After 1 hour, the printed arterial network was placed back inside the climate chamber and left to cure for a total time of at least 24 hours. Figure 15-B displays the 3D-printed arterial network after gluing the individual parts together.

Once the CA glue had fully cured, the mould was adhered to a generic wooden stirring stick using hot glue. This wooden stick served as a handle during the casting process. Next, the diameter of different segments of the mould was measured using a digital calliper. These measurements were used to estimate the wall thickness of the arterial network during casting. Additionally, several of these measurements were also used to evaluate the lumen diameter throughout the coronary artery network of the final phantom, as can be seen in the 'Phantom evaluation' chapter. The Ease Release 200 (Smooth-On, Inc.) release agent was then sprayed onto the mould, before applying several layers of PlatSil Gel 25 with a brush. In order to increase the contrast between the silicone and the 3D-printed mould, 200 drops² SilTone Fresh Blood colorant were added per kilo silicone. Without the increased contrast it would be difficult to apply even layers to the mould, due to the colour and translucency of the silicone. After allowing a few layers of silicone to cure, the diameter of the same arterial segments was measured again. By comparing these results with the previous measurements, the wall thickness could be estimated. If necessary, more layers of silicone were applied to the mould, until the average arterial wall thickness was approximately 1.1 mm. Figure 15-C displays the cast arterial network, before dissolving the 3D-printed mould.

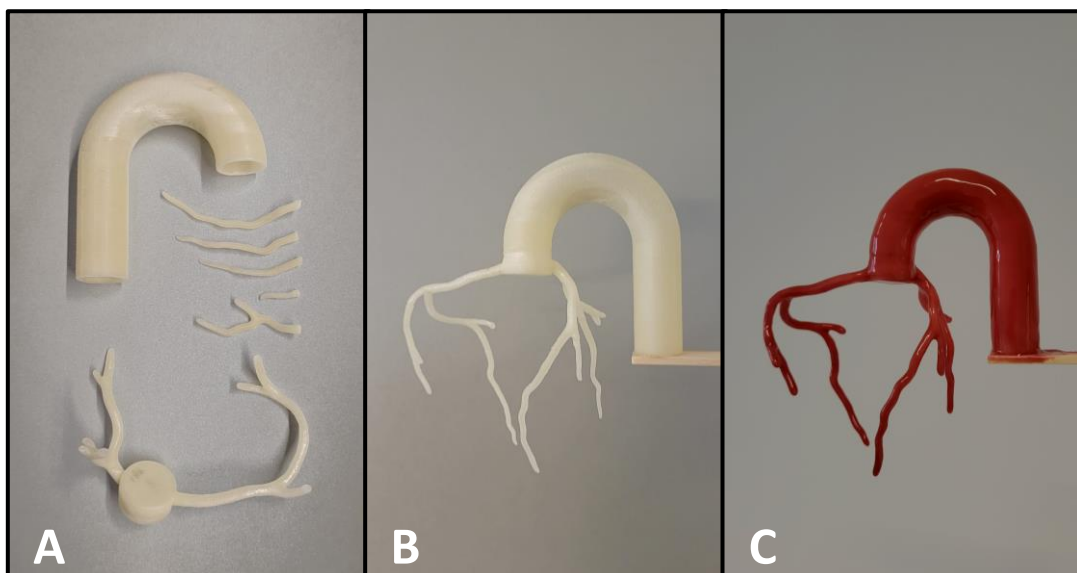


Figure 15. The progression of the arterial network from individual 3D-printed parts to a complete anthropomorphic network. (A) The individual 3D-printed parts of the network after refinement. (B) The final mould of the arterial network, after gluing all parts together. (C) The cast arterial network, before dissolving the 3D-printed mould.

Prior to demoulding the arterial network, the wooden stirring stick was removed from the mould. Subsequently, the cast network was immersed in water to dissolve the mould. This process was accelerated by using hot water. Additionally, the network was regularly manipulated to agitate the water inside of the small branches of the network. Furthermore, parts of the mould were manually broken into smaller pieces before immersing it in water. As a result, several pieces of the mould could be removed without requiring complete dissolution. Nevertheless, the entire demoulding process still required 1 to 2 weeks. During this process, the arterial network slowly fills itself with water while the mould dissolves. Due to the small size of the branches and the single open end, it is difficult to empty the network afterwards. This is similar to a straw that is filled with a liquid and closed on one end. Stepniak et al. (2019) solved this problem by making small holes in the distal ends of the arteries, so air can enter or leave the network. However, this irreversibly damages the phantom. An alternative

² The amount of colorant is expressed in drops, since the actual quantity used, was too small to be accurately weighed.

solution, utilized during this project, is to place the phantom inside of a vacuum chamber and subsequently draw a vacuum. This removes any liquid from the phantom. It is important to ensure that the open end of the network does not get immersed throughout this process, as otherwise, it will fill up again when the pressure is released. To prevent this, paper towels were placed underneath the phantom that absorb any liquid drawn from the network. This method can also be used to fill the phantom. The only difference is that the open-end of the network has to stay immersed throughout the whole process. Once the liquid was removed from the network, a generic silicone tube was glued to the open end using Sil-Poxy (Smooth-On, Inc.). This was done to increase the length of the arterial pathway distal to the aortic root.

THE HEART

Similar to the coronary arteries, the design of the heart is based on a 3D model obtained through the database of Atlas of Human Cardiac Anatomy, University of Minnesota. Model 0141 was selected, since the donor did not have any known cardiac conditions. This model was then refined using Meshmixer. First, any mesh defects were repaired. Then, the aorta, superior vena cava, pulmonary artery and pulmonary vein were removed from the model. Finally, the entire surface of the model was smoothed and its size was slightly reduced to better accommodate the arterial network. Figure 16-A and 16-B display the original and refined 3D model respectively. Subsequently, a mould of the heart was made with SolidWorks. The mould was printed with standard PLA filament (Ultimaker B.V.) on an Ultimaker S3 and Cura was used to slice the model. A regular printing profile for PLA was selected, which automatically configures the printing parameters.

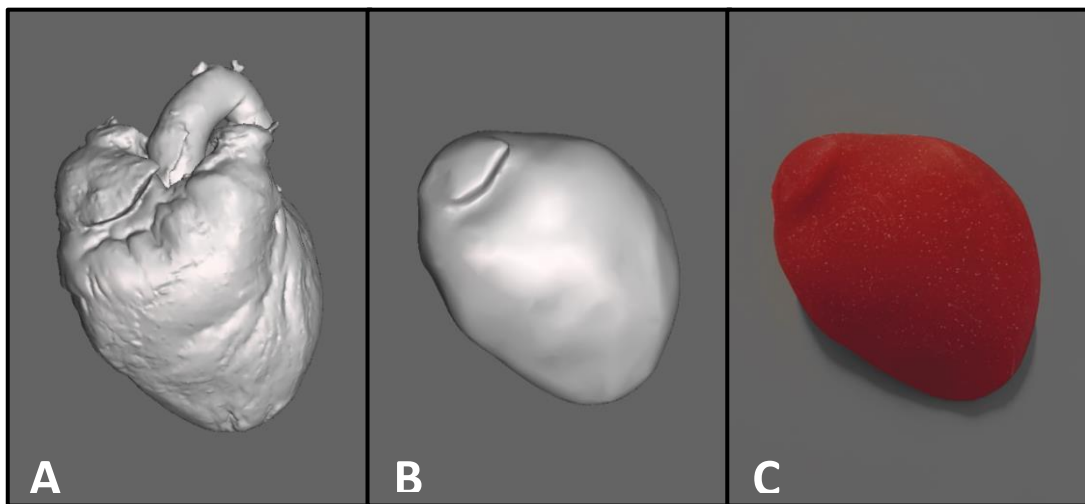


Figure 16. The progression of the heart from the original 3D model to the cast version. (A) The original model which was obtained through the database of Atlas of Human Cardiac Anatomy, University of Minnesota (www.vhlab.umn.edu/atlas). (B) The model after refinement. (C) The final cast heart.

Before casting the heart, the 3D-printed mould was coated with Ease Release 200. In order to increase the radiodensity of VytaFlex 20, 10.0 g BaSO₄ was added per kilo polyurethane. The BaSO₄ was sieved twice and mixed in with the polyurethane while being stirred continuously. According to the results of the material study, this would result in a radiodensity of approximately 100 HU. In addition, 10 drops EPTone Red colorant and 20 g Aerosil thickener were added per kilo polyurethane. The colorant was added purely for aesthetic reasons, however the thickener prevented the BaSO₄ from settling at the bottom of the uncured polyurethane. The need for a thickener was unexpected, as none was required during the casting of the polyurethane samples for the contrast-enhanced material test. Once the polyurethane was fully cured, the heart could be removed from its mould. Figure 16-C displays the cast heart.

CONNECTING THE ARTERIAL NETWORK AND THE HEART

For the final stage of the phantom development, the arterial network and the heart had to be connected to each other. Different adhesives, such as Sil-Poxy and URE-BOND 90 (Smooth-On, Inc.), were tested. However, none of these adhesives adhered strongly to both the silicone arterial network and the heart of polyurethane. During consultations with two different suppliers of casting rubbers, it was suggested to use a mechanical connection instead of a chemical one. Another suggestion was to use an additional material, which can serve as an interface between the silicone and polyurethane. Eventually, these two options were combined to form the following connection method. A power mesh fabric (Lijfgoed) was used as an interface between the silicone and polyurethane. Due to the thin mesh structure of the fabric, it was assumed that it would not be visible in CT and X-ray images. Furthermore, this material is elastic, which results in a slightly compliant connection between the arteries and the heart. First, the power mesh was cut into thin strips. Subsequently, the middle parts of these strips were adhered to the arterial network using Sil-Poxy. After the Sil-Poxy had fully cured, the arterial network was temporarily connected to the heart using sewing pins, see figure 17-A. This had to be done with care, to avoid any damage to the arterial network. The ends of the strips were then adhered to the heart using Loctite 401 CA glue. After the CA glue was fully cured, the sewing pins were carefully removed. Figure 17-B displays the final coronary artery phantom.

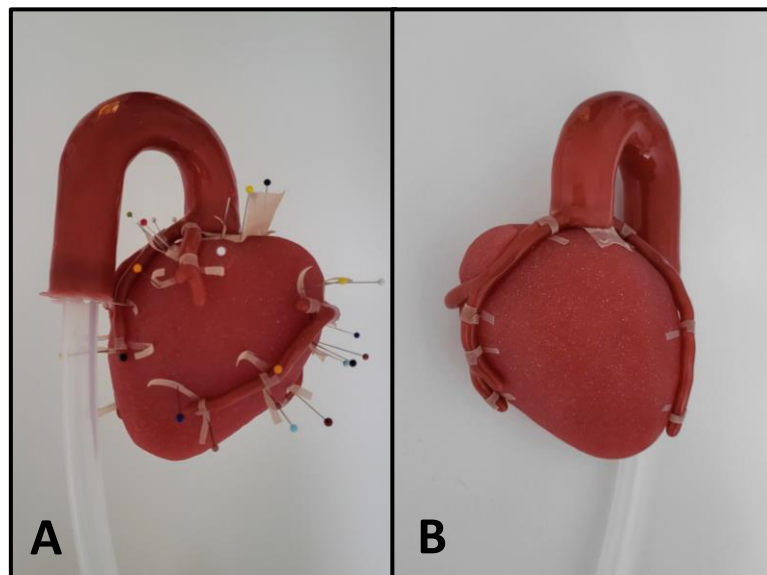


Figure 17. Connecting the arterial network to the heart. (A) The arterial network is temporarily connected to the heart using sewing pins. (B) The final coronary artery phantom.

ATHEROSCLEROTIC PHANTOMS

In addition to the coronary artery network phantom, four smaller atherosclerotic phantoms have been developed. Two of these phantoms represent the LCA, including its bifurcation into the LCx and the LAD, while the other two represent the RCA up to the point where it gives rise to the marginal branch. The design of these phantoms was based on the same 3D model used to design the coronary artery network phantom. After 3D printing the moulds for the atherosclerotic phantoms, stenoses of up to 60 % (i.e., a 60 % reduction of the lumen diameter measured across a single plane) were cut in them using round files, as can be seen in figure 18-A. Subsequently, lesions that matched the shape of the stenoses were cut from samples of polyurethane or silicone. The non-calcified lesions were made from VytaFlex 20, combined with 6.5 g BaSO₄ and 20 g thickener per kilo polyurethane. The calcified lesions were made from PlatSil Gel 25, combined with 500 g PlatSil hardener per kilo PlatSil Gel 25.

In addition, 200 drops³ of colorant and 40.0 g BaSO₄ were added per kilo silicone (i.e. the combined weight of PlatSil Gel 25 and hardener). According to the results of the contrast-enhanced material test, the non-calcified and calcified lesions should have a radiodensity of approximately 50 and 790 HU respectively. However, it should be noted that the partial volume effect did not influence the results of the contrast-enhanced material test.

The atherosclerotic phantoms were cast and demoulded in a similar manner to the coronary artery network phantom. After coating the moulds with a few layers of PlatSil Gel 25, the lesions were placed at the site of the stenosis to fill in the cavities. A few more layers of silicone were then applied to the moulds, until an estimated wall thickness of approximately 1.1 mm was reached. One of the atherosclerotic phantoms was made using two different solutions of silicone, to form a stiffer arterial wall surrounding the lesion. PlatSil Gel 25 in combination with 500 g hardener per kilo PlatSil Gel 25 was used at the site of the lesion, while PlatSil Gel 25 without hardener was used for the surrounding parts. Different colorants were added to the two solutions, in order to visualize the difference in stiffness. Figure 18-B displays the four atherosclerotic phantoms.

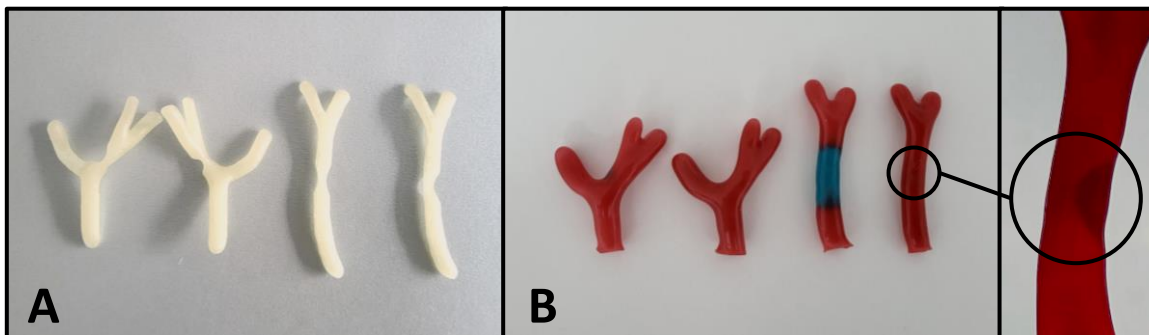


Figure 18. Overview of the four atherosclerotic phantoms. (A) The 3D-printed mould of the atherosclerotic phantoms with stenoses of up to 60 %. (B) The four cast atherosclerotic phantoms.

³ The amount of colorant is expressed in drops, since the actual quantity used, was too small to be accurately weighed.

DISCUSSION

Although the final phantom still had to be evaluated, it can be concluded that the use of a water-soluble mould reduces the design limitations when compared to a non-soluble mould. This is because a water-soluble mould can always be removed, regardless of the geometrical complexity of the design. As a result, it was possible to develop a single arterial network in which the LCA and RCA are each connected to the aortic root. In addition, a pathway distal to the aortic root was included in the phantom. Furthermore, this manufacturing method enables the inclusion of a lesion within the coronary arteries and to locally change the stiffness of the arterial wall.

Nevertheless, this manufacturing method currently has some important disadvantages, mainly that it is very time consuming and labour intensive. For example, the water-soluble mould required a lot of post-processing, due to the poor printing quality. Additionally, the mould was printed in several parts that had to be glued together. This all added a significant amount of time and labour to the manufacturing process. In order to reduce this, the 3D-printing quality should be improved. Stereolithography generally has a higher printing resolution compared to fused deposition modelling. So, one way to increase the 3D-printing quality, could be through the use of a water-soluble resin in combination with stereolithography. Nilsson et al. (2022) and Bisighini et al. (2022) are examples of two studies who employed this method to develop their water-soluble moulds.

Another inefficiency of this manufacturing process, was the use of a brush-on technique to coat the moulds. In the future, the brush-on technique could be replaced by a dip-spin coating technique. Instead of manually coating the mould with a brush, it is then entirely dipped in silicone. To obtain an even coating, the mould is rotated around one or two axes, while the silicone cures. Cortez et al. (2007), Arcaute et al. (2003), Arcaute & Wicker (2008) and Bisighini et al. (2022) all employed this technique during their studies. The use of such a technique should significantly reduce the labour and time.

The way in which the moulds were dissolved also had a large impact on the efficiency of the manufacturing process. Although the demoulding process was mostly passive, it still increased the overall manufacturing time with 1 to 2 weeks. It is well known that temperature and agitation impact the rate at which water-soluble moulds dissolve. While these factors were partially optimized during this project, there is still room left for improvement. For example, to continuously agitate the water inside of small channels, Nilsson et al. (2022) used an ultrasonic cleaner. In future projects, such an ultrasonic cleaner might be used in combination with hot water, to maximize the dissolution rate of water-soluble moulds.

Finally, connecting the arterial network to the heart proved to be quite challenging. It is currently unknown how this step can be made more efficient. However, each inefficiency should be addressed when trying to optimize the manufacturing process. Reducing the overall time and labour intensity will lower the threshold for using this manufacturing method. Such advancements could therefore lead to significant progression in the field of phantom development.

CONCLUSION

As described in this chapter, the arterial network of the phantom was manufactured by 3D printing a mould and applying several layers of silicone using a brush-on technique. A similar manufacturing method was used by Mørup et al. (2022) and Stepniak et al. (2019) to develop their phantom. However, these designs had limitations which likely stemmed from the type of moulds they utilized. To overcome these limitations, a water-soluble 3D-printed mould was used during this project. Contrary to the non-soluble moulds used by the other studies, a soluble mould can always be removed, independent from the complexity of the final design. Because of this, it was possible to manufacture a complex arterial network as a single part. Furthermore, it was shown that this manufacturing method can be used to include lesions in the arterial wall with a stenosis up to 60%. These lesions can be freely positioned at a specific site within the phantom during the manufacturing process. In addition, it is even possible to cast a different silicone surrounding the lesion, to locally change the mechanical properties of the arterial wall. Nevertheless, the manufacturing method still has some important disadvantages, mainly regarding the time consumption and labour intensity. So in conclusion, the use of a water-soluble mould can be considered an improvement on the manufacturing method, allowing one to develop a more complex design. However, many challenges remain and should be resolved in order to optimize the efficiency and encourage a more widespread adoption of this manufacturing method.

5. PART III: PHANTOM EVALUATION

At the start of this project, several mandatory and optional design requirements were formulated. These requirements acted as guidelines during the material study and development of the phantom, and formed the foundation for most of the decisions made throughout this project. However, it is important to evaluate whether the final phantom also meets these requirements. This chapter will provide a description of how the evaluation was conducted. It is divided into four main sections, which correspond to the requirement categories (i.e. general, imaging, geometrical and mechanical). Each section will provide in-depth details on the evaluation of the respective requirements and their results. These results are used to validate the phantom and identify potential areas of improvement.

GENERAL

According to the general requirements, the phantom should at least include a coronary artery network that consists of the LCA and RCA, the LAD and LCx. Optionally, branches of the RCA, LAD and LCx could be included into the network. The final phantom contains all the mandatory arteries, along with the posterior descending artery (PDA), a right and left marginal artery (RMA and LMA respectively) and the 1st and 2nd diagonal artery (D), as illustrated in figure 14. The phantom should also include a simplified heart, an aortic root and a simplified arterial pathway distal to the aortic root. These structures are also present in the final phantom.

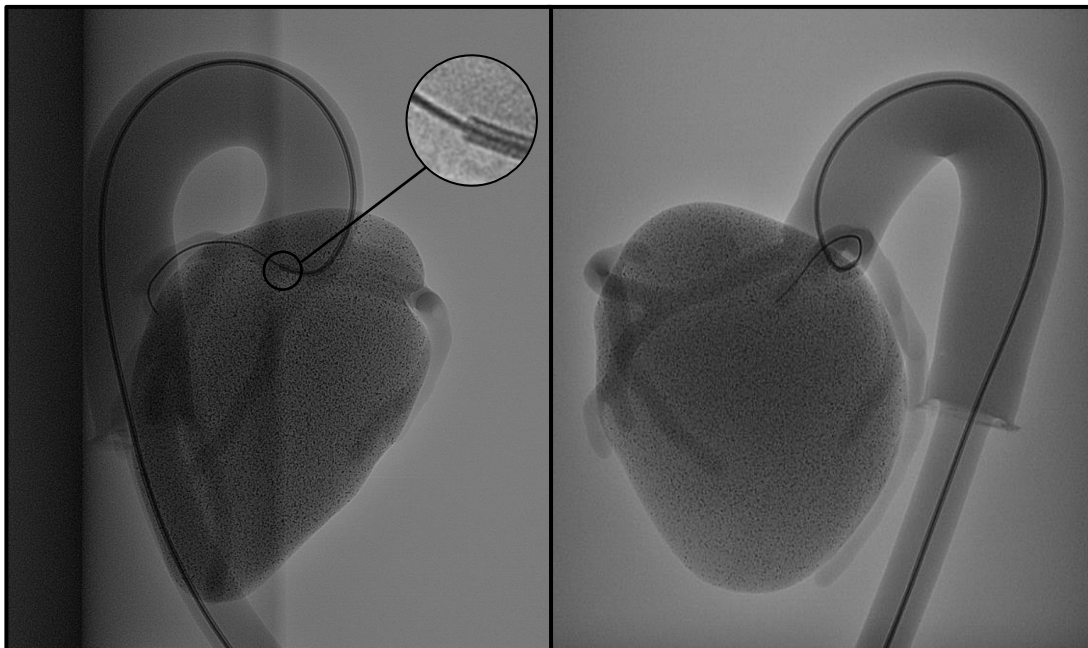


Figure 19. Two X-ray images of the cannulated phantom. The guiding catheter was inserted up to the ostium of the LCA and the guidewire was subsequently advanced to the end of the LCx. (Left) The transition between guiding catheter and guidewire is highlighted in this image. (Right) A demonstration of the foreshortening effect, which makes it difficult to estimate how deep the guidewire was inserted into the LCx.

Furthermore, the arterial network should be hollow, watertight and allow for the insertion of a guidewire into one of the coronary arteries. Based on the manufacturing method employed for the development of the arterial network, it is evident that the entire network is hollow. To evaluate the other two requirements, the phantom was first filled with an NaCl solution and closed off using a generic sealing clip. No leakage was observed, even during transportation of the phantom. Next, a guiding catheter was introduced into the arterial network and moved up to the ostium of the LCA. A guidewire was then advanced through the catheter and manipulated to the end of the LCx.

Figure 19 displays two X-ray images of the cannulated phantom. This test confirms that the phantom allows the insertion of a guidewire into the LCx, indicating its potential to serve as a platform on which a PCI procedure can be performed. The right X-ray image also demonstrates the foreshortening effect, a major limitation associated with 2D images. Due to the angle at which this image is taken, it is difficult to estimate how deep the guidewire was inserted into the LCx. One can contrast this with the left X-ray image, where the angle makes it easier to estimate the depth to which the guidewire was inserted. Finally, the phantom should be transportable and have a shelf life of at least one month. The phantom does not show signs of degradation at the time of writing, despite having been manufactured more than a month ago and transported multiple times. It is therefore concluded that the phantom can indeed be transported and stored for at least a month.

IMAGING

During the material study it was assumed that any additives used for the development of the phantom, except for BaSO₄, would not significantly influence the radiodensity. In order to test this assumption, several cubic samples were cast and measured using the same method as described in the unenhanced material test. Table 7 presents the additives that were used during the development of the phantom. The samples for this test were made from the same material and additive combinations as described in this table. It is important to note that no more than a single additive was added to each sample. In addition, samples of PlatSil Gel 25 and VytaFlex 20 without any additives were used as a reference.

Table 7. An overview of the additives, including the concentrations, that were used during the development of the final phantom.

Material	Additive	Additive concentration
PlatSil Gel 25	SilTone Fresh Blood colorant	200 drops ¹ /kg
	PlatSil hardener	500 g/kg
VytaFlex 20	EPTone Red colorant	10 drops/kg
	Aerosil thickener	20 g/kg

¹The amount of colorant is expressed in drops, since the actual quantity used, was too small to be accurately weighed.

After collecting the data from the measurements, a Shapiro-Wilk and Levene's test were conducted using IBM SPSS Statistics, version 28.0.1.1 (IBM Corp.). These tests assess the normality and homoscedasticity of the data respectively. Table 8 provides an overview of the results of these tests. The results of the Shapiro-Wilk test indicate that the distribution of all the individual data sets does not significantly differ from a normal distribution. Similarly, the Levene's test results indicate that equal variances can be assumed for all groups. Based on this, an independent samples t-test was conducted to compare the mean radiodensity of samples with an additive to that of the reference samples. The silicone colorant, hardener and polyurethane colorant did not significantly influence the radiodensity of the samples, as shown in table 8. However, the thickener significantly increased the radiodensity of the samples made from VytaFlex 20. The parts of the phantom that are made from VytaFlex 20 in combination with the thickener (i.e. the heart and the non-calcified lesions) may therefore exhibit a slightly increased radiodensity, when compared to the expected values based on the material study results.

Table 8. Results of the imaging test, conducted to assess the effect of certain additives on the radiodensity of PlatSil Gel 25 and VytaFlex 20.

Scan	Materials	Radiodensity [HU]	Shapiro-Wilk	Levene's test	Independent samples t-test
1	PG	159 ± 18	$W(5) = .883, p = .335$	$F(1,8) = .017, p = .900$	$t(8) = -.750, p = .475$
	PG + C _{SIL}	167 ± 16	$W(5) = .920, p = .532$		
2	PG	161 ± 17	$W(5) = .915, p = .500$	$F(1,8) = .050, p = .828$	$t(8) = -2.11, p = .067$
	PG + H	183 ± 16	$W(5) = .861, p = .232$		
3	VF	-59 ± 10	$W(5) = .901, p = .414$	$F(1,8) = .121, p = .737$	$t(8) = -.896, p = .396$
	VF + C _{PU}	-53 ± 9	$W(5) = .975, p = .905$		
4	VF	-59 ± 12	$W(5) = .943, p = .685$	$F(1,8) = .219, p = .653$	$t(8) = -2.96, p = .018^*$
	VF + T	-38 ± 11	$W(5) = .927, p = .575$		

PG, PlatSil Gel 25; VF, VytaFlex 20; C_{SIL}, silicone colorant; C_{PU}, polyurethane colorant; H, hardener; T, thickener. The radiodensity is presented as mean ± SD; * significant at $p < 0.05$.

To evaluate the imaging requirements, CBCT images of the phantoms were acquired using the same imaging system and acquisition parameters as used during the imaging tests of the material study. All phantoms were positioned inside of a CT-phantom and filled with an almost saturated NaCl solution (i.e. 350 g NaCl per litre water), to mimic the radiodensity of contrast-enhanced blood. After conducting the measurements, the images were analysed using 3D Slicer (www.slicer.org). To determine the radiodensity of the heart, one spherical VOI of at least 1 cm³ was placed in its centre. For the arterial wall, 30 individual voxels located within the wall were selected. The radiodensity of each voxel was rounded to the nearest integer and used for further analyses. This exact method was also used to determine the mean radiodensity of the arterial lumen and the non-calcified and calcified lesions. Despite the fact that no imaging requirement was formulated for the lumen, it is still important to validate whether the radiodensity is comparable to that of contrast-enhanced blood. This is due to the fact that it can also influence the other results because of the partial volume effect.

Table 9 presents the radiodensity of the individual parts of the phantom. The mean values are used to determine whether each part meets its requirement. The radiodensity of the heart lies within its required range. However, the attenuation was not uniform throughout the tissue, as can be seen in figure 19. The non-calcified and calcified lesions also met their respective imaging requirement. Only the arterial wall did not meet the requirement, as expected based on the results of the material study. Furthermore, the mean radiodensity of the lumen was 330 HU. During the preliminary literature study, it was found that the mean and median radiodensity within the contrast-enhanced coronary lumen across the included studies ranged from 276 to 364. These findings suggest that the radiodensity of the lumen realistically mimics that of contrast-enhanced blood. Lastly, it is interesting to note that the power mesh fabric, which was used to connect the arterial network to heart, was indeed not visible on the CT and X-ray images.

Table 9. The required and actual radiodensity of the different parts of the phantoms.

Anatomical part	Required radiodensity [HU]	Actual radiodensity [HU]
Heart	37 – 117	97 ± 63
Arterial wall	37 – 117	174 ± 19
Non-calcified lesion	34 – 106	37 ± 71
Calcified lesions	377 – 1160	797 ± 180
Lumen	276 – 364 ¹	330 ± 17

¹This range was not included as an official requirement, since the radiodensity of the fluid can be changed without affecting any properties of the phantom.

A green cell indicates that the arterial segment meets their respective requirement, while a red cell indicates the opposite; The actual radiodensity is presented as mean ± SD.

GEOMETRICAL

The design of the coronary artery network and heart had to be based on 3D reconstructions from medical images, in order to ensure that their shapes corresponded to those found in vivo. The database of Atlas of Human Cardiac Anatomy, University of Minnesota was used to obtain the original 3D models. The model of the coronary arteries was reconstructed from CT images of a 68 year old female donor, while that of the heart was reconstructed from CT images of a 24 year old female donor. Both did not have any known cardiac conditions. After selecting the models, they were refined using Meshmixer to obtain the final designs. Care was taken to preserve the original shapes of the models.

Additional requirements were formulated for the lumen diameter, arterial wall thickness and dimensions of the heart to ensure that these parts of the phantoms are correctly sized. Table 10 presents the required lumen diameter for different arterial segments within the network. Since no data was found on the lumen diameter of the RMA, no requirement for this branch was included in the table. The exact descriptions used to define the arterial segments are shown in the appendix. To evaluate this requirement, the diameter at the middle of each arterial segment⁴ within the 3D-printed coronary artery network was measured three times using a digital calliper. Figure 20 displays the exact sites within the network at which the diameters were measured. These measurements were performed during the development stage of this project, prior to casting the phantom, and should directly correspond to the lumen diameter. Table 10 presents the mean diameter for each segment. Based on these results it can be concluded that the lumen diameter of all main arterial segments meet their respective requirement. In addition, two out of four optional branch segments also meet their requirement.

⁴ Except for the D2 and LMA, since these were measured more proximally.

Table 10. Overview of the required and actual lumen diameter of the different arterial segments of the final phantom.

Segment	Required diameter [mm]	Actual diameter [mm]
Right coronary artery		
RCA – 1	2.7 – 5.1	4.5
RCA – 2	2.4 – 4.4	4.1
RCA – 3	2.1 – 4.1	3.6
RCA – 4	1.2 – 3.2	2.8
Posterior descending artery		
PDA ¹	1.4 – 2.6	2.8
Left coronary artery		
LCA	3.5 – 5.5	4.9
Left anterior descending artery		
LAD – 1	2.6 – 4.6	4.0
LAD – 2	1.5 – 3.5	3.5
LAD – 3	0.7 – 2.7	2.7
Diagonal branches		
D1 ¹	0.9 – 2.1	2.2
D2 ²	0.9 – 2.5	2.5
Left circumflex artery		
LCx – 1	2.4 – 4.4	4.0
LCx – 2	1.6 – 4.0	3.4
LCx – 3	0.4 – 2.8	N/A
Left marginal artery		
LMA ³	1.1 – 3.1	2.7

*The ranges for the arterial segments of the RCA, LCA, LAD and LCx are based on the mean ($\pm 2*SD$) results for normal men with right cardiac dominance at the middle of each segment, see table 6 of Dodge et al. (1992). The ranges for the other arterial segments are based on the mean ($\pm 2*SD$) results for normal men with medium branch sizes at the ¹middle, ²proximal third, or ³origin of a segment, see table 7 of Dodge et al. (1992). A green cell indicates that the arterial segment meets their respective requirement, while a red cell indicates the opposite.*

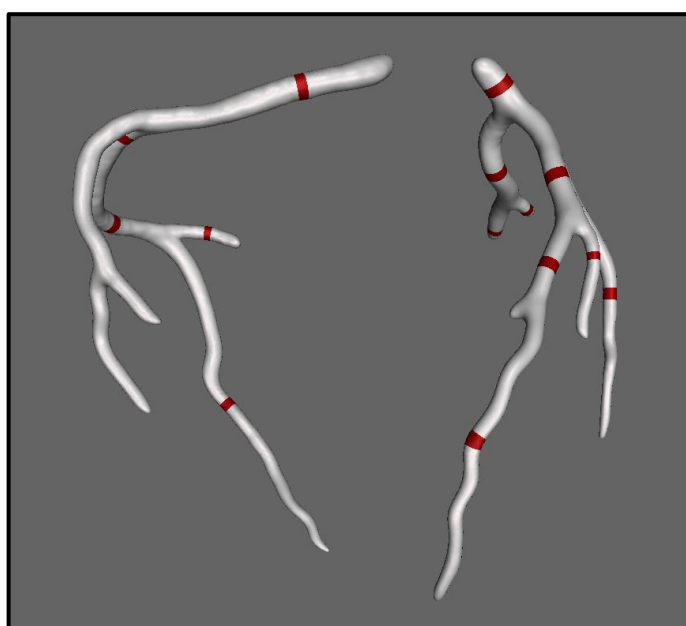


Figure 20. An overview of the sites within the coronary artery network at which the lumen diameters were measured

Besides the lumen diameter, a requirement was formulated for the wall thickness of the arterial network. To measure this directly, the phantom needs to be cut open, which would irreversibly damage it. Therefore, an additional phantom of only the coronary artery network was made, which would act as a substitute during the measurements. Since the same target wall thickness of 1.1 mm was used for the development of the additional phantom, it is assumed that the results will be similar to that of the real phantom. After casting the substitute phantom, it was cut open and measured at the same sites used for evaluating the lumen diameter, as shown in figure 20. For each of these sites, the walls opposite of each other were measured using digital callipers. This resulted in a total of 28 measurements. The average wall thickness was 1.3 ± 0.2 mm. According to the requirements, the wall thickness at each segment in the network should be between 0.7 and 1.5 mm. Twenty-five of the measurements fell within this range.

Lastly, the dimensions of the heart had to be evaluated. Table 11 presents the required and actual dimensions of the heart. The length is defined from the base up to the apex of the heart. The breadth and thickness are the widest and thickest part of the heart respectively. All dimensions were measured using digital callipers and met their respective requirement.

Table 11. The required and actual dimensions of the heart

Dimension	Required range [mm]	Actual measurement [mm]
Length	92.3 – 132.7	97
Breadth	64.4 – 111.2	84
Thickness	48.6 – 74.2	67

A green cell indicates that the dimension meets their respective requirement, while a red cell indicates the opposite.

MECHANICAL

Based on the results of the tensile test conducted during the material study, it was concluded that PlatSil Gel 25 is sufficiently stiff to mimic the elastic modulus of healthy human coronary arteries in the longitudinal direction. When combined with a hardener, it is even able to mimic the elastic modulus of atherosclerotic coronary arteries in the longitudinal direction. Nevertheless, PlatSil Gel 25 cannot achieve sufficient stiffness to mimic the elastic modulus in the circumferential direction of healthy and atherosclerotic coronary arteries. However, the material study did not account for the effect of any additive other than the hardener. Since a colorant was added to the silicone during the development of the arterial wall, it is important to evaluate whether this significantly influences the elastic modulus. To test this, dumbbell shaped samples, with and without any colorant, were cast and measured using the same method as described in the uniaxial tensile test. The coloured samples contained 200 drops⁵ of SilTone Fresh Blood colorant per kilo silicone. Samples without any additives were used as a reference.

⁵ The amount of colorant is expressed in drops, since the actual quantity used, was too small to be accurately weighed.

After collecting the data from the measurements, a Shapiro-Wilk and Levene's test were conducted in IBM SPSS Statistics. Table 12 provides an overview of the results of these tests. The results of the Shapiro-Wilk test indicate that the distribution of all the individual data sets does not significantly differ from a normal distribution. The results of the Levene's test indicate that equal variances between the groups can be assumed. Based on these results, an independent samples t-test was conducted to compare the mean elastic modulus of samples with a colorant to that of the reference samples. The results of the independent samples t-test indicate that the colorant does not have a significant influence on the stiffness of samples made from PlatSil Gel 25, as can be seen in table 12. The conclusions drawn during the material study are therefore still applicable to the final phantom.

Table 12. Results of the uniaxial tensile test, conducted to assess the effect of a colorant on the elastic modulus of PlatSil Gel 25.

Materials	Elastic modulus [MPa]	Shapiro-Wilk	Levene's test	Independent samples t-test
PG	0.3073 ± 0.0092	$W(5) = .911, p = .473$	$F(1,8) = .007, p = .936$	$t(8) = -.528, p = .612$
PG + C _{SIL}	0.3102 ± 0.0084	$W(5) = .938, p = .653$		

PG, PlatSil Gel 25; C_{SIL}, silicone colorant.

The elastic modulus is presented as mean ± SD; * significant at $p < 0.05$.

DISCUSSION

Based on the results of the evaluation, it can be concluded that the final phantom meets many of the formulated requirements. Nevertheless, it also revealed several areas of improvement. Perhaps most important are the improvements related to the imaging properties of the phantom. For example, the radiodensity of the arterial wall did not meet the requirement, as expected based on the results of the material study. It is therefore recommended to research other materials, or additives that could lower the radiodensity of the silicone currently used. However, the latter might result in an arterial network that is too fragile.

Despite the fact that the arterial wall was the only part of the phantom that did not meet the imaging requirement, another point of improvement was apparent. Namely, the radiodensity of the heart was not uniform throughout the tissue. This is due to the fact that the voxels did not contain an even concentration of BaSO₄. This problem also occurred in the non-calcified and calcified lesions, indicated by the relatively large standard deviation of their radiodensity. Additional efforts were taken to evenly disperse and reduce the grain size of the BaSO₄, since this problem also occurred during the material study. Nevertheless, it still persisted. One way to solve it is by using an additive that is soluble in silicone. This is the recommended solution, however such an additive is unknown to the author of this report. Another solution might be to use a non-soluble additive, which is less radiopaque than BaSO₄. Due to the lower radiodensity, such an additive would be used in higher concentrations when compared to BaSO₄, and therefore likely results in a more uniform radiodensity throughout the tissue. Based on the results of Sun et al. (2021), calcium carbonate seems to fit this requirement and could be researched as an alternative to BaSO₄.

In addition to the imaging properties, the geometrical properties of the phantom might also be improved in the future. Two of the optional arterial branch segments did not meet the requirement for the diameter of the lumen. However, it is assumed that the mould of the phantom can be easily modified to meet the requirement for these branch segments. Additionally, it is not considered a significant limitation, since these branch segments are optional and their enlarged lumens do not hinder the usability of the phantom. A more challenging area of improvement, might be the arterial wall thickness. Despite the fact that only 3 of the 28 measurements were larger than the required range, it indicates that considerable deviations from the target wall thickness can occur with the utilized

manufacturing method. This is not desirable, especially since the wall thickness cannot be evaluated directly without irreversibly damaging the phantom. Perhaps that additional experience with the brush-on technique could lead to a more consistent wall thickness. Nevertheless, it could require a significant amount of time to gain the necessary experience. A better solution might be to use a dip-spin coating technique, instead of the brush-on technique. This technique was already recommended to increase the efficiency of the manufacturing method, but might also improve the consistency of the wall thickness.

Finally, it is important to note that the guiding catheter and guidewire were not inserted by an interventional cardiologist. Although it was possible to advance a guidewire up to the LCx, it is unknown how this compares with a similar procedure performed on a real human. Before the phantom can serve as a realistic platform on which a basic PCI procedure can be performed, feedback from an experienced interventional cardiologist is essential. This feedback may form the foundation for a future project, in which the current phantom is further developed.

CONCLUSION

The aim of the evaluation was to assess and compare the final phantom with the requirements formulated at the start of this project. Based on the results, it can be concluded that all general requirements were met. Except for the arterial wall, all parts of the phantom also met their respective imaging requirement. However, the attenuation was not uniform throughout the parts of the phantom that contained BaSO₄, as was evident from the medical images and relatively large standard deviation of their radiodensity. Although this did not directly violate any requirement, it is considered an important area of improvement. As for the geometrical requirements, most of them were met, except for two optional branch segments where the lumen diameter was too large. Additionally, 3 out of the 28 measurements of the atrial wall did not meet the required thickness. Finally, the silicone used for the development of the arterial wall can only mimic the elastic modulus of healthy and atherosclerotic human coronary arteries in the longitudinal direction, not in the circumferential direction. In conclusion, the final phantom meets many of the formulated requirements, but there still remain areas of improvement that could be addressed during a future project.

6. DISCUSSION

This project was divided into three parts, namely the material study, the design and development of the phantom, and its evaluation. The aim of the material study was to identify the most suitable materials for the development of the phantom. These materials were primarily selected based on the results of several imaging tests. However, these tests were conducted using a CBCT scanner, instead of a MDCT scanner. This is an important limitation, since radiodensities obtained through CBCT are associated with a greater variability than those obtained through MDCT (Pauwels et al., 2015). The large variability of the results was also observed throughout this study. Some measures were taken in an attempt to negate this limitation. For example, larger sample sizes and volumes of interests were used, and most results were compared with those of other studies. Nevertheless, it is still recommended to use MDCT for future projects. This is especially important during measurements that are prone to a higher variability, or those in which the results are based on a relatively small number of voxels, as was the case with the measurements of the hollow cylindrical samples during the unenhanced material test.

During the second part of the project, the coronary artery network phantom was designed and developed. The initial results were promising, although the phantom still had to be evaluated. Furthermore, it was demonstrated that a water-soluble mould reduces design limitations when compared to a non-soluble mould, as was hypothesized at the beginning of the development phase. Nevertheless, the utilized manufacturing process still had some significant limitations, mainly regarding its efficiency. One way to increase the efficiency, is by improving the 3D-printing quality of the mould, which in turn reduces the necessary post-processing. Additionally, a dip-spin coating technique could be used instead of the brush-on technique, to coat the mould. This could not only reduce the required labour and time, but might also result in a more consistent arterial wall thickness. Finally, the rate at which the mould is dissolved and the method used to connect the arterial network to the heart should be improved. By addressing these inefficiencies, the threshold for using this manufacturing method will be greatly reduced, which could lead to a significant progression in the field of phantom development.

The final evaluation of the phantom demonstrated that many requirements were met, but it also revealed several areas of improvement. The varying radiodensity throughout the parts of the phantom containing BaSO₄, might be the most significant limitation. While this did not directly violate any requirement, it should be resolved to improve the imaging properties of the phantom. Additionally, the radiodensity of the arterial wall did not fall within the required range. In the future, this might be resolved through the use of an additive or by substituting the PlatSil Gel 25 with another material.

Furthermore, as part of the evaluation, a guidewire was inserted into the arterial network and advanced up to the LCx. Since this procedure was not performed by an interventional cardiologist, it is unknown how it compares to a similar procedure performed on a real human. Feedback from an experienced interventional cardiologist would be valuable for further development of the current phantom. However, before conducting any tests, it is recommended to incorporate a hemostatic valve into the arterial network. This would facilitate the introduction of medical equipment and make it more realistic. If a test with an interventional cardiologist is to be performed, one point of feedback that could be expected is regarding the friction between the medical equipment and the silicone. The friction might be significantly higher compared to what is experienced during the procedure on a real human. In such a case, SLIDE STD (Smooth-On, Inc.) could be added to the silicone during the manufacturing process to reduce the friction.

Finally, although this phantom was originally developed for researchers of Philips research, it might also serve as a beneficial tool for training medical students. However, a consultation with a cardiologist

revealed that such a training phantom should also be able to mimic blood flow. Currently, this is not incorporated into the phantom. As a result, once the phantom is filled with a fluid that mimics contrast-enhanced blood, the lumen remains continuously visible on X-ray images. This is in contrast with a real procedure, where the arterial lumen is visible for only a short duration, before the injected contrast agent is dispersed and becomes diluted. The continuous visibility of the lumen in a phantom without flow, would make such a training tool too simplistic according to the cardiologist. Addressing this issue could be an interesting and challenging topic for a future project.

7. CONCLUSION

During percutaneous coronary intervention, the coronary artery network is visualized using X-ray imaging and contrast injections. A major limitation associated with this method, is that it only generates 2D images. To overcome this, researchers of Philips Research are developing technologies that allow the implementation of 3D imaging data derived from coronary CT angiography in the catheterization laboratory. Throughout the development and validation of these novel technologies, a coronary artery network phantom could serve as a beneficial tool. Such a phantom should be anthropomorphic and have realistic imaging and mechanical properties. In addition, it should serve as a platform on which a basic PCI procedure can be performed. However, to the best of the author's knowledge and those involved in the project, there is currently no commercially or academically developed phantom that satisfies these criteria. As a result, the following objective was formulated for this project:

Design and develop an anthropomorphic coronary artery network phantom with realistic imaging and mechanical properties, that can be used to mimic both healthy and atherosclerotic human coronary arteries.

By utilizing a 3D-printed, water-soluble mould of the coronary artery network, and coating this with silicone, it was possible to manufacture a network with realistic geometrical properties. Based on the results of the material study, it was concluded that PlatSil Gel 25 was to be used for the development of the arterial wall. Unfortunately, its radiodensity was slightly too high, when compared to that in vivo. However, it was able to mimic the elastic modulus of both healthy and atherosclerotic human coronary arteries in the longitudinal direction. The radiodensity of the heart and the lesions did meet their formulated imaging requirement. Nevertheless, the consistency of the attenuation throughout these parts should be improved. Lastly, during the evaluation of the phantom, it was demonstrated that a guidewire can be inserted into the arterial network and manipulated up to the end of the LCx. This indicates the potential of the phantom to serve as a platform on which a PCI procedure can be performed.

This project demonstrated that the utilized manufacturing method and materials can be used to develop a healthy or atherosclerotic coronary artery network phantom. It can be concluded that the final phantom possesses geometrical, imaging and mechanical properties that are comparable to the tissues found in vivo. Nevertheless, several areas of improvement remain, which might form the foundation for a future project.

REFERENCES

- Arcaute, K., Palafox, G. N., Medina, F., & Wicker, R. B. (2003). Complex silicone aorta models manufactured using a dip-spin coating technique and water-soluble molds. *Proceedings of the 2003 Summer Bioengineering Conference*, 1093–1094.
- Arcaute, K., & Wicker, R. B. (2008). Patient-Specific Compliant Vessel Manufacturing Using Dip-Spin Coating of Rapid Prototyped Molds. *Journal of Manufacturing Science and Engineering*, 130(5). <https://doi.org/10.1115/1.2898839>
- Austen, W., Edwards, J., Frye, R., Gensini, G., Gott, V., Griffith, L., McGoon, D., Murphy, M., & Roe, B. (1975). A reporting system on patients evaluated for coronary artery disease. Report of the Ad Hoc Committee for Grading of Coronary Artery Disease, Council on Cardiovascular Surgery, American Heart Association. *Circulation*, 51(4), 5–40. <https://doi.org/10.1161/01.CIR.51.4.5>
- Bisighini, B., Di Giovanni, P., Scerrati, A., Trovalusci, F., & Vesco, S. (2022). Fabrication of Compliant and Transparent Hollow Cerebral Vascular Phantoms for In Vitro Studies Using 3D Printing and Spin–Dip Coating. *Materials*, 16(1), 166. <https://doi.org/10.3390/ma16010166>
- Brown, J. C., Gerhardt, T. E., & Kwon, E. (2024). *Risk Factors for Coronary Artery Disease*.
- Campbell, P. T., Mahmud, E., & Marshall, J. J. (2015). Interoperator and intraoperator (in)accuracy of stent selection based on visual estimation. *Catheterization and Cardiovascular Interventions*, 86(7), 1177–1183. <https://doi.org/10.1002/ccd.25780>
- Chanda, A., & Curry, K. (2018). Patient-Specific Biofidelic Human Coronary Artery Surrogates. *Journal of Mechanics in Medicine and Biology*, 18(05), 1850049. <https://doi.org/10.1142/S0219519418500495>
- Clouse, M. E., Sabir, A., Yam, C.-S., Yoshimura, N., Lin, S., Welty, F., Martinez-Clark, P., & Raptopoulos, V. (2008). Measuring Noncalcified Coronary Atherosclerotic Plaque Using Voxel Analysis with MDCT Angiography: A Pilot Clinical Study. *American Journal of Roentgenology*, 190(6), 1553–1560. <https://doi.org/10.2214/AJR.07.2988>
- Collet, C., Sonck, J., Leipsic, J., Monizzi, G., Buytaert, D., Kitslaar, P., Andreini, D., & De Bruyne, B. (2021). Implementing Coronary Computed Tomography Angiography in the Catheterization Laboratory. *JACC: Cardiovascular Imaging*, 14(9), 1846–1855. <https://doi.org/10.1016/j.jcmg.2020.07.048>
- Cortez, M. A., Quintana, R., & Wicker, R. B. (2007). Multi-step dip-spin coating manufacturing system for silicone cardiovascular membrane fabrication with prescribed compliance. *The International Journal of Advanced Manufacturing Technology*, 34(7–8), 667–679. <https://doi.org/10.1007/s00170-006-0649-5>
- Dodge, J. T., Brown, B. G., Bolson, E. L., & Dodge, H. T. (1992). Lumen diameter of normal human coronary arteries. Influence of age, sex, anatomic variation, and left ventricular hypertrophy or dilation. *Circulation*, 86(1), 232–246. <https://doi.org/10.1161/01.CIR.86.1.232>
- Gradus-Pizlo, I., Sawada, S. G., Wright, D., Segar, D. S., & Feigenbaum, H. (2001). Detection of subclinical coronary atherosclerosis using two-dimensional, high-resolution transthoracic echocardiography. *Journal of the American College of Cardiology*, 37(5), 1422–1429. [https://doi.org/10.1016/S0735-1097\(01\)01160-3](https://doi.org/10.1016/S0735-1097(01)01160-3)

- Gupta, C., Palimar, V., Saxena, A., & D'souza, A. (2014). A morphometric study of measurements of heart in adults and its relation with age and height of the individual: A post-mortem study. *CHRISMED Journal of Health and Research*, 1(4), 263. <https://doi.org/10.4103/2348-3334.143000>
- Hagita, T., Shiotani, S., Toyama, N., Tominaga, N., Miyazaki, H., & Ogasawara, N. (2022). Correlation between Hounsfield Unit values of blood in CT on immediate postmortem CT after cardiopulmonary resuscitation and antemortem hemoglobin levels. *Forensic Imaging*, 30. <https://doi.org/10.1016/j.fri.2022.200515>
- Inohara, T., Kohsaka, S., Spertus, J. A., Masoudi, F. A., Rumsfeld, J. S., Kennedy, K. F., Wang, T. Y., Yamaji, K., Amano, T., & Nakamura, M. (2020). Comparative Trends in Percutaneous Coronary Intervention in Japan and the United States, 2013 to 2017. *Journal of the American College of Cardiology*, 76(11), 1328–1340. <https://doi.org/10.1016/j.jacc.2020.07.037>
- Jin, H., Lee, S. Y., An, H. J., Choi, C. H., Chie, E. K., Wu, H., Park, J. M., Park, S., & Kim, J. (2022). Development of an anthropomorphic multimodality pelvic phantom for quantitative evaluation of a deep-learning-based synthetic computed tomography generation technique. *Journal of Applied Clinical Medical Physics*, 23(8). <https://doi.org/10.1002/acm2.13644>
- Kamaruddin, N., Rajion, Z. A., Yusof, A., & Aziz, M. E. (2016). *Relationship between Hounsfield unit in CT scan and gray scale in CBCT*. <https://doi.org/10.1063/1.4968860>
- Lai, M., Skyrman, S., Kor, F., Homan, R., El-Hajj, V. G., Babic, D., Edström, E., Elmi-Terander, A., Hendriks, B. H. W., & de With, P. H. N. (2022). Development of a CT-Compatible, Anthropomorphic Skull and Brain Phantom for Neurosurgical Planning, Training, and Simulation. *Bioengineering*, 9(10), 537. <https://doi.org/10.3390/bioengineering9100537>
- Litt, H. I., & Brody, A. S. (2001). BaSO₄-Loaded Agarose: A Construction Material for Multimodality Imaging Phantoms. *Academic Radiology*, 8(5), 377–383. [https://doi.org/10.1016/S1076-6332\(03\)80544-5](https://doi.org/10.1016/S1076-6332(03)80544-5)
- Mørup, S. D., Stowe, J., Precht, H., Gervig, M. H., & Foley, S. (2022). Design of a 3D printed coronary artery model for CT optimization. *Radiography*, 28(2), 426–432. <https://doi.org/https://doi.org/10.1016/j.radi.2021.09.001>
- Nieman, K., Cury, R. C., Ferencik, M., Nomura, C. H., Abbara, S., Hoffmann, U., Gold, H. K., Jang, I.-K., & Brady, T. J. (2006). Differentiation of Recent and Chronic Myocardial Infarction by Cardiac Computed Tomography. *The American Journal of Cardiology*, 98(3), 303–308. <https://doi.org/10.1016/j.amjcard.2006.01.101>
- Nikolaou, K., Knez, A., Sagmeister, S., Wintersperger, B. J., Boekstegers, P., Steinbeck, G., Reiser, M. F., & Becker, C. R. (2004). Assessment of Myocardial Infarctions Using Multidetector-Row Computed Tomography. *Journal of Computer Assisted Tomography*, 28(2), 286–292. <https://doi.org/10.1097/00004728-200403000-00021>
- Nilsson, D. P. G., Holmgren, M., Holmlund, P., Wåhlin, A., Eklund, A., Dahlberg, T., Wiklund, K., & Andersson, M. (2022). Patient-specific brain arteries molded as a flexible phantom model using 3D printed water-soluble resin. *Scientific Reports*, 12(1), 10172. <https://doi.org/10.1038/s41598-022-14279-7>
- Nygren, D. (2021). *MRAC capable phantom fluids: A study of hybrid phantom fluids for attenuation correction in PET/MRI and PET/CT*.

- Okuma, H., Gonoi, W., Ishida, M., Shiota, G., Shintani, Y., Abe, H., Fukayama, M., & Ohtomo, K. (2014). Comparison of Attenuation of Striated Muscle between Postmortem and Antemortem Computed Tomography: Results of a Longitudinal Study. *PLoS ONE*, *9*(11), e111457. <https://doi.org/10.1371/journal.pone.0111457>
- O'Reilly, M., Hoff, M., Friedman, S. D., Jones, J. F. X., & Cross, N. M. (2020). Simulating Tissues with 3D-Printed and Castable Materials. *Journal of Digital Imaging*, *33*(5), 1280–1291. <https://doi.org/10.1007/s10278-020-00358-6>
- Pauwels, R., Jacobs, R., Singer, S. R., & Mupparapu, M. (2015). CBCT-based bone quality assessment: are Hounsfield units applicable? *Dentomaxillofacial Radiology*, *44*(1). <https://doi.org/10.1259/dmfr.20140238>
- Perry, R., De Pasquale, C. G., Chew, D. P., Brown, L., Aylward, P. E., & Joseph, M. X. (2008). Changes in Left Anterior Descending Coronary Artery Wall Thickness Detected by High Resolution Transthoracic Echocardiography. *The American Journal of Cardiology*, *101*(7), 937–940. <https://doi.org/10.1016/j.amjcard.2007.11.053>
- Perry, R., Joseph, M. X., Chew, D. P., Aylward, P. E., & De Pasquale, C. G. (2013). Coronary Artery Wall Thickness of the Left Anterior Descending Artery Using High Resolution Transthoracic Echocardiography – Normal Range of Values. *Echocardiography*, *30*(7), 759–764. <https://doi.org/10.1111/echo.12136>
- Pfaffenberger, S., Bartko, P., Graf, A., Pernicka, E., Babayev, J., Lolic, E., Bonderman, D., Baumgartner, H., Maurer, G., & Mascherbauer, J. (2013). Size Matters! Impact of Age, Sex, Height, and Weight on the Normal Heart Size. *Circulation: Cardiovascular Imaging*, *6*(6), 1073–1079. <https://doi.org/10.1161/CIRCIMAGING.113.000690>
- Razi, T., Niknami, M., & Alavi Ghazani, F. (2014). Relationship between Hounsfield Unit in CT Scan and Gray Scale in CBCT. *Journal of Dental Research, Dental Clinics, Dental Prospects*, *8*(2), 107–110. <https://doi.org/10.5681/joddd.2014.019>
- Rodriguez-Martinez, A., Zhou, B., Sophiea, M. K., Bentham, J., Paciorek, C. J., Iurilli, M. L., Carrillo-Larco, R. M., Bennett, J. E., Di Cesare, M., Taddei, C., Bixby, H., Stevens, G. A., Riley, L. M., Cowan, M. J., Savin, S., Danaei, G., Chirita-Emandi, A., Kengne, A. P., Khang, Y.-H., ... Ezzati, M. (2020). Height and body-mass index trajectories of school-aged children and adolescents from 1985 to 2019 in 200 countries and territories: a pooled analysis of 2181 population-based studies with 65 million participants. *The Lancet*, *396*(10261), 1511–1524. [https://doi.org/10.1016/S0140-6736\(20\)31859-6](https://doi.org/10.1016/S0140-6736(20)31859-6)
- Russ, M., O'Hara, R., Nagesh, S. V. S., Mokin, M., Jimenez, C., Siddiqui, A. M. D., Bednarek, D., Rudin, S., & Ionita, C. (2015). Treatment planning for image-guided neuro-vascular interventions using patient-specific 3D printed phantoms. *Proc.SPIE*, *9417*, 941726. <https://doi.org/10.1117/12.2081997>
- Shepard, L. M., Sommer, K. N., Angel, E., Iyer, V., Wilson, M. F., Rybicki, F. J., Mitsouras, D., Molloy, S., & Ionita, C. N. (2019). Initial evaluation of three-dimensionally printed patient-specific coronary phantoms for CT-FFR software validation. *Journal of Medical Imaging*, *6*(02), 1. <https://doi.org/10.1117/1.JMI.6.2.021603>
- Silva, I. M. de C. C., Freitas, D. Q. de, Ambrosano, G. M. B., Bóscolo, F. N., & Almeida, S. M. (2012). Bone density: comparative evaluation of Hounsfield units in multislice and cone-beam

- computed tomography. *Brazilian Oral Research*, 26(6), 550–556. <https://doi.org/10.1590/S1806-83242012000600011>
- Sommer, K. N., Iyer, V., Kumamaru, K. K., Rava, R. A., & Ionita, C. N. (2020). Method to simulate distal flow resistance in coronary arteries in 3D printed patient specific coronary models. *3D Printing in Medicine*, 6(1), 19. <https://doi.org/10.1186/s41205-020-00072-7>
- Steinmann, A., Stafford, R. J., Sawakuchi, G., Wen, Z., Court, L., Fuller, C. D., & Followill, D. (2018). Developing and characterizing MR/CT visible materials used in QA phantoms for MRgRT systems. *Medical Physics*, 45(2), 773–782. <https://doi.org/10.1002/mp.12700>
- Stepniak, K., Ursani, A., Paul, N., & Naguib, H. (2019). Development of a phantom network for optimization of coronary artery disease imaging using computed tomography. *Biomedical Physics & Engineering Express*, 5(4), 045019. <https://doi.org/10.1088/2057-1976/ab2696>
- Stepniak, K., Ursani, A., Paul, N., & Naguib, H. (2020). Novel 3D printing technology for CT phantom coronary arteries with high geometrical accuracy for biomedical imaging applications. *Bioprinting*, 18, e00074. <https://doi.org/10.1016/j.bprint.2020.e00074>
- Sultana, J., Akhter, A., Choudhury, S., & Sultana, Z. (2011). A Descriptive Study of Different Dimensions of Postmortem Heart of Adult Bangladeshi People. *Jalalabad Medical Journal*, 8(1), 3–5.
- Sun, Z., Ng, C. K. C., Wong, Y. H., & Yeong, C. H. (2021). 3D-Printed Coronary Plaques to Simulate High Calcification in the Coronary Arteries for Investigation of Blooming Artifacts. *Biomolecules*, 11(9), 1307. <https://doi.org/10.3390/biom11091307>
- Yadegari, A., Safi, Y., Shahbazi, S., Yaghoutiazar, S., & Ghazizadeh Ahsaie, M. (2023). Assessment of CBCT gray value in different regions-of-interest and fields-of-view compared to Hounsfield unit. *Dentomaxillofacial Radiology*, 52(8). <https://doi.org/10.1259/dmfr.20230187>

APPENDIX

DEFINITIONS OF THE ARTERIAL SEGMENTS

Table 13. Definitions of the arterial segments present in the final phantom based on Dodge et al. (1992), and a comparison with the reporting system of the American Heart Association (AHA).

Segment	AHA¹	Description²
Right coronary artery		
RCA – 1	1	From its origin to the first RMA.
RCA – 2	2	From the first to the third RMA.
RCA – 3	3	From the third RMA to PDA.
RCA – 4	–	From the PDA to the end of the RCA.
Posterior descending artery		
PDA	4	Proximal most inferior wall branch that arises from junction of RCA – 3 and RCA – 4.
Left coronary artery		
LCA	5	From ostium to bifurcation of LCA into LAD and LCx.
Left anterior descending artery		
LAD – 1	6	From its origin at the LCA to the first septal artery.
LAD – 2	7	From the first to the third septal artery.
LAD – 3	8	From the third septal artery to the cardiac apex.
Diagonal branches		
D1	9	The first large branch arising from the LAD to supply the left ventricular anterior free wall.
D2	10	The second large branch arising from the LAD to supply the left ventricular anterior free wall.
Left circumflex artery		
LCx – 1	11	From its origin at the LCA to the first LMA
LCx – 2	13	From the first to the second LMA.
LCx – 3	13	From the second LMA to the end of the LCx.
Left marginal artery		
LMA	12	The first large branch arising from the LCx.

¹A comparison with the definitions used in the AHA reporting system, see Austen et al. (1975); ²These definitions originate from Dodge et al. (1992) and are based on a right dominant heart.

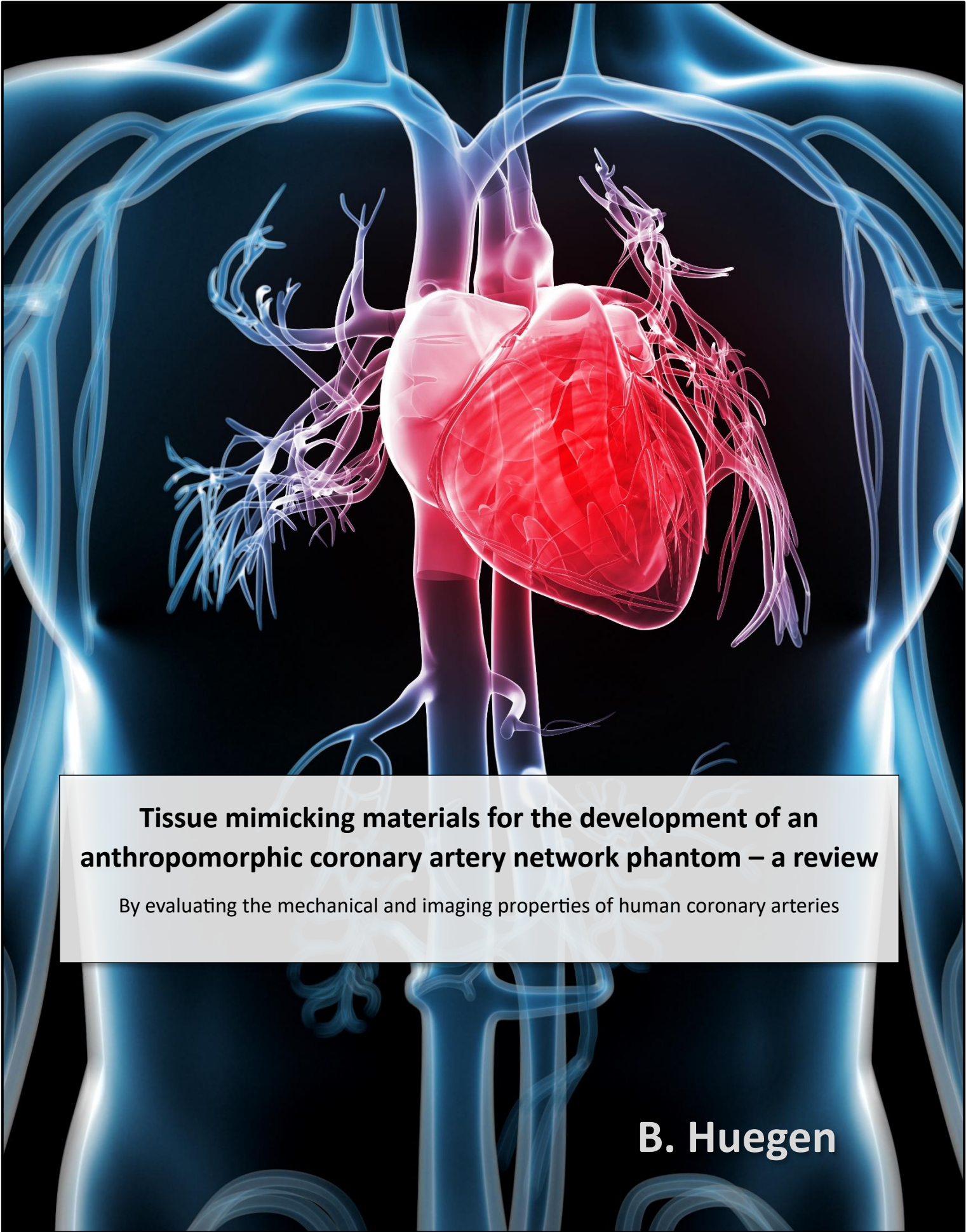
DATA PROCESSING SCRIPT – UNIAXIAL TENSILE TEST

```
1  %Written by Bjorn Huegen
2  %11-10-2023
3
4  clc
5  clf
6  clear all
7
8  %Parameters of the linear model for calibration of the load cell
9  a = 1.8183;
10 b = -0.0120;
11
12 %Initial sample dimensions
13 L0 = 25; %Test length of the dumbbell sample [mm]
14 t = 2.0; %Thickness of the dumbbell sample [mm]
15 W = 6.4; %Width of the narrow part of the dumbbell sample [mm]
16 A0 = t*W; %The initial cross-sectional area of the dumbbell sample [mm^2]
17
18 dx = 10; %Translation of the linear stage in which we are interested [mm]
19
20 %Load the data
21 d_0 = load("Data/Measurements/1 - 1.mat");
22
23 run_0 = d_0.(subsref(fieldnames(d_0),substruct('{}',{1}))).Y(5).Data;
24 x_0 = d_0.(subsref(fieldnames(d_0),substruct('{}',{1}))).Y(2).Data;
25 F_0 = d_0.(subsref(fieldnames(d_0),substruct('{}',{1}))).Y(1).Data;
26
27 %The starting index is based on the stRun vector
28 i_start = find(run_0, 1, "first");
29
30 %The ending index is based on when the linear stage has reached a certain
31 %position. Not on stRun, since the measurement might be manually stopped.
32 i_end = find(x_0 < x_0(i_start)-dx, 1, "first");
33
34 %Crop the position and force data
35 x_0 = x_0(i_start:i_end);
36 F_0 = F_0(i_start:i_end);
37
38 %Recalculate load cell output to force and applying a moving average filter
39 F_cal = a*F_0 + b; %N
40 F_cal = movmean(F_cal, 150);
41
42 %Engineering stress
43 Stress_eng = F_cal / A0; %MPa
44
45 %Engineering strain
46 L = -1*(x_0-x_0(1)) + L0;
47 Strain_eng = (L - L0) / L0;
48
49 %True strain
50 Strain_true = log(1 + Strain_eng);
51
52 %True stress (assuming incompressibility and all deformation occurring in
53 %the narrow part of the dumbbell sample)
54 Stress_true = Stress_eng .* (1 + Strain_eng);
55
56 %Find the last index of the region of interest (ROI)
57 i = find(Strain_true > 0.10, 1, "first");
```

```

58 %Make a linear approximation of the ROI
59 [P, S] = polyfit(Strain_true(1:i), Stress_true(1:i), 1);
60
61 %Plot the true stress vs. true strain + initial linear section
62 figure(1)
63 hold on
64 plot(Strain_true, Stress_true, 'LineWidth', 1.5)
65 Line = line([0, 0.1], [P(2), P(1)*0.1+P(2)], 'color', 'red', 'LineWidth',
66 1.5);
67 Line.Color(4) = 0.75;
68 sgtitle("True stress-strain curve (150 moving average)")
69 xlabel("True strain")
70 ylabel("True stress [MPa]")
71 legend('True stress vs true strain', 'linear approximation up to 0.1
72 strain')
73
74 %Young's Modulus
75 YoungsModulus = P(1)

```



Tissue mimicking materials for the development of an anthropomorphic coronary artery network phantom – a review

By evaluating the mechanical and imaging properties of human coronary arteries

B. Huegen

Tissue mimicking materials for the development of an anthropomorphic coronary artery network phantom – a review

By evaluating the mechanical and imaging properties of human coronary arteries

By

B. Huegen

Literature research in partial fulfilment of the requirements for the degree of

Master of Science

In BioMedical Engineering

At Delft University of Technology

April, 2023

Supervisors:

Prof. dr. J.J. van den Dobbelsteen

Prof. dr. B.H.W. Hendriks

Delft University of Technology

Delft University of Technology & Philips



ABSTRACT

Percutaneous coronary intervention (PCI) is a medical procedure aimed at revascularizing the coronary arteries. Since the introduction of PCI, significant technological and medical advancements have been made. To aid the development and pre-clinical trials of novel medical instruments, a coronary artery network phantom could serve as a beneficial tool. The use of a phantom would not only reduce the need for biological tissue, but also provide a more controlled and standardized testing environment. Despite the potential benefits, no literature exists that presents an overview of tissue mimicking materials (TMM's) that could be utilized during the development of such a phantom. Therefore, the aim of this literature review is to provide researchers with an overview of TMM's that could be used throughout the development of a coronary artery network phantom, designed for testing novel medical instruments and technologies developed for (complex) PCI.

Both the mechanical and imaging properties of coronary arteries have to be identified, in order to compare them with potential TMM's. More specifically, the elastic modulus in the longitudinal and circumferential direction and the degree of X-ray attenuation, expressed as a Hounsfield Unit (HU), are considered in this review. Systematic search methods were employed to retrieve relevant literature on these two properties. Based on the findings, the elastic moduli in longitudinal direction of healthy and atherosclerotic human coronary arteries ranges from 0.28 to 2.94 MPa and 0.4 to 5.63 MPa respectively. The elastic moduli in circumferential direction of both healthy and atherosclerotic coronary arteries ranges from 0.78 to 1.68 MPa and 1.13 to 4.11 MPa respectively. Only atherosclerotic coronary arteries were considered when identifying the imaging properties, since there was no literature available on healthy arteries that met the inclusion criteria. These atherosclerotic lesions are categorized as either lipid-rich, fibrotic or calcific. The Hounsfield units for these lesions ranges from 34 to 104 HU, 67 to 106 HU and from 377.2 to 1160 HU for lipid-rich, fibrotic and calcified lesions respectively.

According to several review articles, six different TMM's are nowadays commonly used for the development of soft tissue phantoms, namely agar, agarose, gelatine, PVA, PVC and silicone. Additional searches were employed to find relevant literature on the mechanical and imaging properties of these materials. The findings suggest that all included materials could be used to mimic the HU values of lipid-rich, fibrotic and calcified lesions. In the case of the latter, additives should be utilized to increase the HU values of the TMM's. Contrary to the imaging properties, not all materials are suited to mimic the in-vivo mechanical properties of human coronary arteries. Only PVC and silicone could be used to mimic the complete ranges of elastic moduli in longitudinal and circumferential direction of healthy and atherosclerotic arteries. Agar, agarose and PVA can be used to mimic the elastic moduli in longitudinal direction of healthy and atherosclerotic human coronary arteries. Agarose can also mimic the elastic modulus in circumferential direction of healthy coronary arteries. Gelatine was the only included material that had insufficient mechanical properties to mimic the elastic moduli of the healthy and atherosclerotic coronary arteries in any direction. Based on these results, silicone, PVC, PVA, agar and agarose can all be used for the development of an anthropomorphic coronary network phantom with realistic mechanical and imaging properties.

TABLE OF CONTENTS

ABSTRACT	II
LIST OF TABLES	IV
LIST OF ABBREVIATIONS	V
1. INTRODUCTION.....	1
2. METHOD.....	2
2.1 Mechanical properties.....	2
2.2 Imaging properties	3
2.3 Materials.....	4
3. RESULTS.....	5
3.1 Mechanical properties.....	5
3.2 Imaging properties	9
3.3 Materials.....	11
4. DISCUSSION	14
4.1 Mechanical properties.....	14
4.2 Imaging properties	16
4.3 Materials.....	17
5. CONCLUSION	18
REFERENCES.....	20

LIST OF TABLES

Table 1: Inclusion criteria used for evaluating the literature on mechanical properties.	3
Table 2: Inclusion criteria used for evaluating the literature on imaging properties.	4
Table 3: Overview of the Young's moduli in longitudinal direction of healthy and atherosclerotic human coronary arteries found during the systematic search. The Young's moduli are expressed as a mean \pm SD; \bar{E}_I = low stiffness region; \bar{E}_{II} = high stiffness region; ¹ = refers to the number of donors, since the exact number of samples per donor was unknown; ² = this value was not explicitly mentioned in the paper, but instead determined based on an included graph.	5
Table 4: Overview of the Young's moduli in circumferential direction of healthy and atherosclerotic human coronary arteries found during the systematic search. The Young's moduli are expressed as a mean \pm SD; M = male; F = female; 1 – 6 = refers to the different group ages used in the study; LAD = left anterior descending (artery); RCA = right coronary artery; ¹ = refers to the number of donors, since the exact number of samples per donor was unknown; ² = this value was not explicitly mentioned in the paper, but instead determined based on an included graph.	8
Table 5: Overview of the Hounsfield units of different types of atherosclerotic human coronary arteries found during the systematic search. The Hounsfield units are expressed as mean \pm SD, or median (min. – max.) values, depending on the notation that was used in the respective study; ¹ = this value was not explicitly mentioned in the paper, but instead determined based on an included graph.	9

LIST OF ABBREVIATIONS

AHA	American Heart Association
CABG	Coronary artery bypass grafting
CAD	Coronary artery disease
CCTA	Coronary CT angiography
CT	Computed tomography
GS	Google Scholar
HU	Hounsfield unit
LAD	Left anterior descending (artery)
LCA	Left coronary artery
NSTEMI	Non-ST-elevation myocardial infarction
PCI	Percutaneous coronary intervention
PVA	Polyvinyl alcohol
PVC	Polyvinyl chloride
RCA	Right coronary artery
SAD	Stage of atherosclerosis development
SCAD	Stable coronary artery disease
SD	Standard deviation
STEMI	ST-elevation myocardial infarction
TMM	Tissue mimicking material
VH-IVUS	Virtual histology intravascular ultrasound
WoS	Web of Science (core collection)

1. INTRODUCTION

Coronary artery disease (CAD) is the leading cause of mortality worldwide (Ralapanawa & Sivakanesan, 2021). In 2015 alone, CAD resulted in approximately 8.9 million deaths (Zhang et al., 2018). This imposes a large burden on the global healthcare sector and has a significant economic impact. CAD is typically caused by an accumulation of plaque within the tunica intima of the arterial wall, commonly known as atherosclerosis. This accumulation of plaque leads to a narrowing, or stenosis, of the lumen. Significant stenosis of the coronary arteries will lead to a reduction or a complete stop of the flow of oxygen to the myocardium and other anatomical structures, including the superior vena cava and the semilunar valves (Burris & Shoukfeh, 2015). Myocardial ischemia will in turn lead to malfunctioning of the heart and, in severe cases, complete heart failure.

Percutaneous coronary intervention (PCI) is one of the two main coronary revascularization procedures. The other revascularization procedure is known as coronary artery bypass grafting (CABG). Based on the 2018 guidelines on myocardial revascularization and the 2021 guideline for coronary artery revascularization, four clinical indications can be identified that qualify for PCI. These indications are stable coronary artery disease (SCAD), unstable angina, non-ST-elevation myocardial infarction (NSTEMI) and ST-elevation myocardial infarction (STEMI) (Lawton et al., 2022; Neumann et al., 2019). The primary aim of PCI is to dilate or open a stenosed or occluded coronary artery respectively. This is usually achieved by inflating a balloon within the affected artery, balloon angioplasty, followed by implanting a stent to ensure that the artery stays open.

Since the introduction of PCI, significant technological and medical advancements have been made. Some of these advancements led to a reduction of the post-procedural risks, such as the introduction of the drug-eluting stent (Piccolo et al., 2019). Other advancements enabled the treatment of more complex lesions, including but not limited to, bifurcation, calcified and thrombotic lesions. During the development and pre-clinical trials of these novel medical instruments, a coronary artery network phantom could serve as a beneficial tool. The use of such a phantom would reduce the use of animal and human tissue, providing a more ethical alternative. Furthermore, it could provide a more controlled and standardized testing environment. However, commercially available phantoms may have disadvantages, including high prices, lack of customizability or incorrect material properties. As such, researchers might want to design and develop their own in-house phantom. Currently, there is no literature review available that provides researchers with an overview of the tissue mimicking materials (TMM's) that could be used during the development of a coronary artery phantom. Such an overview could help researchers make a more informed decision regarding which material to use and reduce the required research time. Because of these advantages, the aim of this literature review is to provide an overview of TMM's for the development of an anthropomorphic coronary artery network, by answering the following research question:

What different tissue mimicking materials can be used in the development of an anthropomorphic coronary artery network phantom, designed for testing novel medical instruments and technologies developed for (complex) PCI?

2. METHOD

In order to answer the main research question, the following three sub-questions have been formulated:

- I. *What is the elastic modulus in longitudinal and circumferential direction of healthy and atherosclerotic human coronary arteries?*
- II. *What is the degree of X-ray attenuation, expressed as a Hounsfield Unit, of atherosclerotic human coronary arteries?*
- III. *What different tissue mimicking materials are currently used for the development of soft tissue phantoms?*

The first sub-question is related to the required mechanical properties of the tissue mimicking materials. Although there are several different mechanical properties that could be considered, this review focuses on the elastic moduli in the longitudinal and circumferential direction of the coronary arteries. This property was chosen, because it can quantify the relationship between the stresses applied during a medical procedure and the strain of the arterial wall. Moreover, this property can be measured with ease and is frequently utilized when describing material properties. The latter is important, since the findings have to be compared with the mechanical properties of different TMM's.

The second sub-question focuses on the degree of X-ray attenuation of atherosclerotic human coronary arteries, expressed as a Hounsfield Unit (HU). It is essential to have knowledge of the degree of X-ray attenuation, since X-ray based imaging techniques (e.g., fluoroscopy and coronary CT angiography [CCTA]) are commonly employed during PCI. The amount of X-ray attenuation can be expressed using different metrics, including a linear attenuation coefficient or the Hounsfield scale. The latter is actually based on the linear attenuation coefficient and was chosen for this review, since it is commonly used in literature. Initially, the aim was to consider the imaging properties of healthy human coronary arteries, as well as atherosclerotic ones. However, a minimal amount of literature on healthy arteries was found throughout the search phase and none that also met the inclusion criteria. As a result, healthy coronary arteries have been excluded from this sub-question.

The aim of the final sub-question is to provide an overview of TMM's that are currently utilized for the development of soft tissue phantoms. Information on both the elastic moduli and HU value of these TMM's will also be included in this section. Including this information, allows one to compare the properties of the TMM's with the mechanical and imaging properties required to mimic either healthy or atherosclerotic human coronary arteries.

2.1 Mechanical properties

A systematic search method was employed in order to retrieve the required literature for answering the first sub-question. This search method minimizes the chance of missing relevant articles related to the sub-question. Three multidisciplinary databases were utilized for the retrieval of literature, namely Google Scholar (GS), Scopus and Web of Science Core Collection (WoS). The following search string was used across all three databases:

("elastic modulus" OR "young's modulus" OR "tensile modulus" OR "stiffness") AND ("human coronary arteries")

All the results from Scopus and WoS were evaluated for relevance, based on the inclusion criteria listed below. Because of the large number of results that GS provided, only the articles from the first five pages, sorted by relevance, were evaluated.

Inclusion criteria

Table 1 presents a complete overview of the inclusion criteria used to assess the found literature, based on their relevance. Given the limited number of relevant results and the fact that measurements of elastic moduli are not susceptible to becoming outdated, a relatively large search window was utilized. This search window was initially set to 20 years, but this did not result in enough relevant literature on the elastic moduli in the circumferential direction. As a result, the search window was increased to 25 years, which provided an additional study. It should be noted that the elastic modulus of human coronary arteries can differ significantly from that of animals. For example, a study conducted by van Andel et al. (2003) showed large differences between the stress-strain curves of human and porcine coronary arteries, both in the longitudinal and circumferential direction. Hence, only literature that focuses on human coronary arteries was included in this systematic literature review. Furthermore, the included literature had to focus on the general elastic modulus of the arteries. Studies that focused on the local mechanical properties, as determined by micro-indentation tests, or mechanical properties of the individual layers of the arterial wall were excluded. Two examples of such studies are those by Holzapfel et al. (2005) and Rezvani-Sharif et al. (2019). This criterion was based on the assumption that most anthropomorphic coronary artery network phantoms will only simulate the general mechanical properties, due to the technical difficulties associated with developing a phantom with varying local mechanical properties. Finally, the included studies must provide a clear description of their measurement method and results. This is essential in order to assess the scientific value of a particular study.

Table 14: Inclusion criteria used for evaluating the literature on mechanical properties.

Inclusion criteria

- Published between 1998 and March of 2023
- Written in English
- Complete access to the article
- Journal article (including reviews) or conference paper
- The study focuses on healthy and atherosclerotic human coronary arteries.
- The study focuses on the general elastic modulus, in either the longitudinal or circumferential direction.
- The study provides a clear description of the measurement method and results.

2.2 Imaging properties

Once again, a systemic search method in combination with the three aforementioned multidisciplinary databases was employed in order to retrieve the required literature for the second sub-question. The following search string was used across all three databases:

("Hounsfield unit" OR "CT number" OR "X-ray attenuation" OR "radiodensity") AND ("human coronary arteries")

All the results from Scopus and WoS were evaluated for relevance, based on the inclusion criteria listed below. Because of the large number of results that GS provided, only the articles from the first five pages, sorted by relevance, were evaluated.

Inclusion criteria

Table 2 presents a complete overview of the inclusion criteria used to assess the found literature, based on their relevance. A search window of 20 years was utilized, in order to retrieve sufficient literature. There are various CT scan parameters that can influence the measured HU value. Two particularly important parameters are the tube potential and tube current. Only studies that utilized a tube potential of 120 kV during their measurements were included in this review. At such a high tube potential, the tube current has a negligible effect on the measured HU value (Afifi et al., 2020). It is also important to focus on only a single tube potential, since this parameter in itself has a substantial effect on the HU value (Afifi et al., 2020). Moreover, 120 kV is a typical value for the tube potential during CT scans of the heart, making it a suitable criterion (Feuchtner et al., 2010; Tanami et al., 2010). Finally, the included studies must provide a clear description of their measurement method and results. This is essential in order to assess the scientific value of a particular study.

Table 15: Inclusion criteria used for evaluating the literature on imaging properties.

Inclusion criteria

- Published between 2003 and March of 2023
- Written in English
- Complete access to the article
- Journal article (including reviews) or conference paper
- The study focuses on atherosclerotic human coronary arteries.
- The study conducted their measurements with a tube potential of 120 kV.
- The study provides a clear description of the measurement method and results.

2.3 Materials

For this section of the review, no systematic search method was employed, since such a method would presumably not provide added benefit when compared to a more general search method. Instead, several review articles were used in order to provide an overview of the most important and widely utilized TMM's in the development of soft tissue phantoms. These review articles were retrieved from GS, by utilizing the following search string:

"Tissue mimicking materials"

The results were sorted by relevance and filtered to only include review articles from 2018 to March of 2023, to ensure that the information would be current. The following search strings were utilized as a first step for finding literature on the elastic moduli and HU value of the found TMM's:

- ("elastic modulus" OR "young's modulus" OR "tensile modulus" OR "stiffness") AND ("phantom") AND ("... **type of material** ...")
- ("Hounsfield unit" OR "CT number" OR "X-ray attenuation" OR "radiodensity") AND ("phantom") AND ("... **type of material** ...")

If necessary, additional and more specific search strings were used to retrieve relevant information about a particular TMM.

3. RESULTS

The search methods described in the previous chapter were employed to find relevant studies on the respective topics. This chapter aims to provide the reader with a short overview of the found literature, including possible methods, results and conclusions. For more in-depth information of these studies, one should always consult the original source.

3.1 Mechanical properties

The search method for the mechanical properties of human coronary arteries as described in the method section of this review, resulted in eight unique scientific studies. After further assessing these studies, it was determined to exclude one of them from this literature review. This study was conducted by Kural et al. (2012) and measured the elastic modulus in both the longitudinal and circumferential direction by means of a biaxial tension test. The results deviated much from the other studies and the paper did not provide an in-depth discussion of possible reasons which could explain this. One such reason could be the use of engineering stress and engineering strain to calculate the Young's moduli, as opposed to true stress and strain values. This would result in lower moduli, although it is unlikely that this explanation fully accounts for the deviation. Furthermore, the study conducted measurements on a small sample size and there is no simple relationship between the uniaxial and biaxial elastic moduli for non-linear materials (Kural et al., 2012). As such, the study was excluded from this review. From the remaining studies that were included in this overview, four focused exclusively on the elastic modulus of the coronary arteries in the longitudinal direction, two focused exclusively on the properties in the circumferential direction and one study conducted measurements in both directions. Table 3 and 4 present an overview of the found Young's moduli in the longitudinal and circumferential direction respectively.

Longitudinal direction

All of the studies that measured the elastic modulus of coronary arteries in the longitudinal direction, utilized a uniaxial tensile test setup for this. The strain was measured using video cameras, and some studies combined this with digital calliper measurements. In order to increase the repeatability of the stress-strain curves, most studies employed a mechanical preconditioning protocol. Only the study conducted by Karimi et al. (2013) did not describe the use of such a preconditioning routine. All tissue samples were preserved in a saline solution and most of these were stored at 4-5 °C. Only Jankowska et al. (2015) did not provide information about the temperature at which the samples were stored. All but one study explicitly stated that the samples were harvested within 5 hours post-mortem. Again, Jankowska et al. (2015) did not provide any information about this. Both Jankowska et al. (2015), Karimi et al. (2013) and Karimi et al. (2017b), stated that the measurements were conducted within 24 hours after excision. Furthermore, all studies used relatively low strain rates, from 1 up to 5 mm/min. Karimi et al. (2017a) also performed measurements with higher strain rates, up to 50 mm/min, to study the influence of the strain rate on the elastic moduli of human coronary arteries.

Jankowska et al. (2015) measured a total of 27 samples of the left and right coronary arteries (LCA and RCA respectively) without side branches. These samples were harvested from 18 patients, aged between 50 and 84 years old. All samples were categorized based on visual and histological observation. These samples were either categorized as healthy (in the study referred to as 'SAD 0'), or atherosclerotic. The atherosclerotic samples were further divided into three groups with increasing severity, ranging from 'SAD I' to 'SAD III' (corresponding with 'atherosclerotic – mild' to 'atherosclerotic - severe' in table 3). The stress-strain curves were obtained from the true stress (i.e., Cauchy stress) and engineering strain values. The tangent moduli of elasticity were determined in a low and high stiffness region (i.e., \bar{E}_I and \bar{E}_{II} respectively), which were separated by a transition point on the curve. This transition point was located at a point on the curve which has the maximum normal distance to

an imaginary line drawn between the origin and the end of the curve. The exact point within these regions at which the tangent moduli are determined is unknown.

Table 16: Overview of the Young's moduli in longitudinal direction of healthy and atherosclerotic human coronary arteries found during the systematic search. The Young's moduli are expressed as a mean \pm SD; \bar{E}_I = low stiffness region; \bar{E}_{II} = high stiffness region; ¹ = refers to the number of donors, since the exact number of samples per donor was unknown; ² = this value was not explicitly mentioned in the paper, but instead determined based on an included graph.

Study	Tissue type	Description	Sample size	Young's Modulus [MPa]
(Jankowska et al., 2015)	Healthy	\bar{E}_I	1	2.85
		\bar{E}_{II}		20.96
	Atherosclerotic – mild	\bar{E}_I	7	0.40 \pm 0.20
		\bar{E}_{II}		4.51 \pm 4.29
	Atherosclerotic – moderate	\bar{E}_I	6	0.56 \pm 0.30
		\bar{E}_{II}		5.63 \pm 3.44
Atherosclerotic – severe	\bar{E}_I	13	1.45 \pm 1.79	
	\bar{E}_{II}		3.31 \pm 2.84	
(Karimi et al., 2013)	Healthy	Physiological	14	1.48 \pm 0.24
		Maximum		1.55 \pm 0.26
	Atherosclerotic	Physiological	8	3.77 \pm 0.38
		Maximum		4.53 \pm 0.43
(Karimi et al., 2017a)	Healthy	5 mm/min	3	0.28 ²
		20 mm/min		0.55 \pm 0.06
		50 mm/min		1.20 ²
	Atherosclerotic	5 mm/min	3	5.15 ²
		20 mm/min		1.42 ²
		50 mm/min		13.1 \pm 0.64
(Karimi et al., 2017b)	Healthy		8 ¹	8.33
	Atherosclerotic		8 ¹	14.27 ²
(Karimi et al., 2019)	Healthy		6	2.94 \pm 2.61
	Atherosclerotic		6	0.75 \pm 0.58

Karimi et al. (2013) measured 14 healthy and 8 atherosclerotic human coronary arteries, harvested from proximal or distal branchless segments. The mean age of the two groups was 38.07 ± 8.58 and 65.50 ± 10.33 years respectively. Both true stress and true strain values were used to obtain the stress-strain curves. Based on these stress-strain curves, a physiological and maximum elastic modulus were determined. The physiological modulus was derived from a part of the curve between 80 and 120 mmHg (corresponding to approximately 10.6 and 16 kPa), which is almost linear (Duprey et al., 2010). The maximum elastic modulus corresponded to the maximum slope of the curve. According to the study, the atherosclerotic arteries had significantly higher physiological and maximum Young's moduli compared to that of healthy coronary arteries ($p < 0.05$).

The aim of the study conducted by Karimi et al. (2017a) was to investigate the potential effect of the strain rate on the stiffness of coronary arteries, as measured with uniaxial tensile tests. In total, 9 healthy and 9 atherosclerotic samples were used. Both groups were further divided into three equally sized groups, each subjected to a different strain rate. The stress was defined as a Cauchy or true stress. Based on the article, it was unclear which definition for the strain was used. The elastic modulus was obtained from a region referred to as the "elastic deformation region", which is bounded by the origin and 30% of the strain failure. Finally, this study showed that the strain rate can have a significant effect on the measured stiffness of atherosclerotic human coronary arteries ($p < 0.05$).

Karimi et al. (2017b) measured both the longitudinal and circumferential stiffness of samples harvested from 8 healthy and 8 atherosclerotic male donors, with a mean age of 43.8 ± 18.4 and 59.1 ± 14.1 respectively. The exact number of samples that were collected per donor is not mentioned in the paper. True stress and engineering strain were used to obtain the stress-strain curves of the measured samples. Subsequently, the Young's modulus was determined on the basis of the initial linear section of the respective curve. Karimi et al. (2017b) concluded that atherosclerotic coronary arteries are significantly stiffer than healthy ones, regardless of the loading direction ($p < 0.005$).

The final paper included in this section of the review is that of Karimi et al. (2019). The samples originated from 6 healthy and 6 atherosclerotic male individuals, aged 51 ± 12 and 56 ± 13 years respectively. A single sample was retrieved per donor. It is unknown which definition for strain was used. The stress values were expressed as true stress values and the elastic modulus was determined based on the initial slope of the stress-strain diagram. The results of this study showed that healthy coronary arteries are significantly stiffer than that of atherosclerotic arteries ($p < 0.05$).

Circumferential direction

There were three studies that measured the stiffness of human coronary arteries in the circumferential direction. Karimi et al. (2017b) was analysed in the previous section and will therefore not be covered in this one. Both Tajaddini et al. (2005) and Kasjanovs et al. (1999) used a test setup in which the arteries were pressurized and subsequent change in the arterial diameter was measured. Such a measurement is also known as a distensibility test and the results can be used to calculate a circumferential elastic modulus. During the measurements, the intravascular pressure was increased from 0 to 260 mmHg (Tajaddini et al., 2005), or from 0 to 240 mmHg (Kasjanovs et al., 1999) in steps of 20 mmHg. Between the 20 mmHg increments, the arteries were given time to stabilize. As with most uniaxial tensile tests, the arteries were preconditioned to obtain a more repeatable mechanical response. Throughout the tests, the arteries were mounted inside a chamber containing a saline solution at approximately 37°C, in order to replicate in vivo conditions. Finally, both studies measured their samples within 24 hours post-mortem.

Tajaddini et al. (2005) measured 51 samples of moderately occluded (i.e., a plaque burden $< 50\%$), non-calcified atherosclerotic left anterior descending (LAD) arteries. The results of the hyperglycaemic group were excluded from this review. Therefore, only the results of 32 samples are considered, 17 of which belonged to a young group with a mean age of 43.8 ± 3.3 and 15 belonged to an older group with a mean age of 58.8 ± 8.6 years. These LAD arteries were not removed from their extravascular tissue. Instead, a portion of myocardium that contained the LAD was dissected from the heart. During the measurements, the myocardium acted as a natural support structure for the LAD arteries. Based on the results of the distensibility tests, the mid-wall circumferential stress was calculated using an equation for thick-walled cylinders. The circumferential strain was defined as the change of the mid-wall radius in comparison to the initial mid-wall radius. This was calculated within a physiological pressure range from 60 to 140 mmHg. Next, the Young's modulus was determined from the stress-strain curve within the physiological pressure range. The results revealed that the arterial wall of moderately occluded atherosclerotic LAD arteries was significantly stiffer in the older group compared to the young group ($p < 0.05$).

The study conducted by Kasjanovs et al. (1999) included 121 male and 84 female donors, which were divided into 6 groups according to their age. The three youngest groups, ranging from 0 to 19 years old, did not show signs of atherosclerosis. The three older groups, ranging from 20 to 80 years old, did show signs of atherosclerosis. On average, the atherosclerosis development progressed from mild to more severe with the increasing group age. In the paper it is stated that the mechanical properties of the proximal and distal parts of the RCA and LAD artery were tested for each donor. Despite this, only the

mean elastic moduli of the proximal parts of both arteries in men were explicitly stated in a table. The elastic moduli of both arteries for the female groups were included in a graph, although it is unclear whether these values represent measurements for the proximal or distal parts. Contrary to Tajaddini et al. (2005), the circumferential stresses were calculated using an equation for thin-walled cylinders. The circumferential stretch ratio was used to express the strain. All elastic moduli were determined at a circumferential stress of 0.1 MPa, which corresponded to an intravascular pressure of 200 to 240 mmHg.

Table 17: Overview of the Young's moduli in circumferential direction of healthy and atherosclerotic human coronary arteries found during the systematic search. The Young's moduli are expressed as a mean \pm SD; M = male; F = female; 1 – 6 = refers to the different group ages used in the study; LAD = left anterior descending (artery); RCA = right coronary artery; ¹ = refers to the number of donors, since the exact number of samples per donor was unknown; ² = this value was not explicitly mentioned in the paper, but instead determined based on an included graph.

Study	Tissue type	Description	Sample size	Young's modulus [MPa]	
(Tajaddini et al., 2005)	Atherosclerotic - moderate	Young	17	1.41 \pm 0.72	
		Old	15	3.09 \pm 2.47	
(Karimi et al., 2017b)	Healthy		8 ¹	4.14 ²	
	Atherosclerotic		8 ¹	15.38	
(Kasjanovs et al., 1999)	Healthy	M, 1, LAD	9	1.17 \pm 0.41	
		M, 1, RCA		1.06 \pm 0.24	
		M, 2, LAD	15	1.12 \pm 0.26	
		M, 2, RCA		1.64 \pm 0.28	
		M, 3, LAD	15	0.90 \pm 0.48	
		M, 3, RCA		1.22 \pm 0.68	
	Atherosclerotic – mild	M, 4, LAD	34	1.57 \pm 0.58	
		M, 4, RCA		2.00 \pm 0.78	
	Atherosclerotic – moderate	M, 5, LAD	27	2.19 \pm 0.74	
		M, 5, RCA		2.08 \pm 0.64	
	Atherosclerotic – severe	M, 6, LAD	21	4.11 \pm 0.89	
		M, 6, RCA		2.85 \pm 0.76	
	Healthy	F, 1, LAD	5	1.21 ²	
				F, 1, RCA	1.12 ²
			5	0.80 ²	
				F, 2, RCA	0.78 ²
			5	0.90 ²	
				F, 3, RCA	0.90 ²
		Atherosclerotic – mild	F, 4, LAD	28	1.22 ²
			F, 4, RCA		1.13 ²
Atherosclerotic – moderate		F, 5, LAD	22	1.32 ²	
		F, 5, RCA		1.63 ²	
Atherosclerotic – severe		F, 6, LAD	19	1.62 ²	
		F, 6, RCA		3.49 ²	

3.2 Imaging properties

The search method for the imaging properties of human coronary arteries as described in the method section of this review, resulted in seven unique scientific studies. Six of those studies conducted measurements on ex vivo tissue, while only Obaid et al. (2013) performed in vivo measurements. Table 5 presents an overview of the found literature and corresponding results. The results presented in the table are either expressed as mean \pm standard deviation (SD), or median (minimum – maximum) values, depending on the notation used in the respective study. In this review, the different atherosclerotic lesions are preferably categorized as either lipid-rich, fibrotic or calcific. All but one of the included studies used this classification directly, or utilized the classification of the American Heart Association (AHA) described by Stary et al. (1995). According to the classification of the AHA, type Vb (or VII) lesions correspond to calcified lesions and type Vc (or VIII) to fibrous ones. Type IV, Va (or V) and VI lesions are considered to be lipid-rich, which is similar to the classification used by Galonska et al. (2008).

Table 18: Overview of the Hounsfield units of different types of atherosclerotic human coronary arteries found during the systematic search. The Hounsfield units are expressed as mean \pm SD, or median (min. – max.) values, depending on the notation that was used in the respective study; ¹ = this value was not explicitly mentioned in the paper, but instead determined based on an included graph.

Study	Tissue type	Description	Sample size	Hounsfield unit
(Halliburton et al., 2006)	Noncalcified	Pre-enhanced	22	-3.4 \pm 31.2
		Peak enhanced		82.9 \pm 81.6
	Mixed calcified	Pre-enhanced	8	195.9 \pm 307.6
		Peak enhanced		222.9 \pm 296.6
	Densely calcified	Pre-enhanced	2	234.9 \pm 60.2
		Peak enhanced		377.2 \pm 10.7
(Galonska et al., 2008)	Lipid-rich	Type IV	4	50 (33 – 59)
		Type V	24	44 (26 – 63)
		Type VI	5	40 (36 – 67)
	Fibrous	Type VIII	21	67 (37 – 124)
	Calcified	Type VII	82	1089 (333 – 1944)
	(Tanami et al., 2010)	Lipid-rich		39
Fibrotic			30	27.1 \pm 5.0
Calcified			24	780 \pm 574
(Chopard et al., 2010)	Lipid-rich		20	70 \pm 41
	Fibrous		42	83 \pm 35
	Calcified		21	966 \pm 473
(Henzler et al., 2011)	Lipid-rich	Type IV	7	34 (19 – 43) ¹
		Type Va	12	45 (26 – 70) ¹
	Calcified	Type Vb	31	1160 (430 – 1895) ¹
(Leschka et al., 2010)	Lipid-rich	Type IV	25	55 \pm 12
		Type V	66	34 \pm 19
		Type VI	20	104 \pm 84
	Fibrous	Type VIII	43	91 \pm 16
	Calcified	Type VII	60	501 \pm 402
	(Obaid et al., 2013)	Lipid-rich	Necrotic core	35
Fibrous			34	106 (0 – 294)
Calcified			39	770 (358 – 1587)

All of the studies that used ex vivo tissue for their measurements, classified the lesions based on histopathological analysis. The study conducted by Obaid et al. (2013) classified the lesions with means of virtual histology intravascular ultrasound (VH-IVUS), since histopathological analysis of in vivo tissue is not possible. Most studies explicitly stated that they tried to minimize the time between passing of the donors and conducting the measurements, to avoid changes of the tissue properties. Contrast agent was also widely employed among the included literature. Only Tanami et al. (2010) conducted measurements without perfusing the coronary arteries with contrast agent. Based on the mean and median values found in the studies, the attenuation within the coronary lumen ranged from 276 to 364 HU across the studies that employed a contrast agent. Moreover, different reconstruction kernels were used among the studies.

Halliburton et al. (2006) measured both the pre-enhanced and peak-enhanced HU values of atherosclerotic coronary arteries. Based on the findings it was concluded that the pre-enhanced HU values were significantly lower compared to the peak-enhanced HU values, of both non-calcified and densely calcified lesions ($p < 0.0001$ and $p = 0.0274$ respectively). This effect was not found for mixed calcified lesions. Galonska et al. (2008) found a significant difference in attenuation between non-calcified lesions (i.e., lipid-rich and fibrous lesions) and calcified lesions ($p < 0.001$). The calcified lesions displayed higher HU values than the non-calcified ones. The same study also found a significant difference in attenuation between lipid-rich and fibrous lesions, despite the overlap between the two ranges ($p < 0.001$). In this case, the HU values for lipid-rich lesions were on average lower than that of fibrous ones. Obaid et al. (2013) also found significant differences between the three types of lesions while performing in vivo measurements ($p < 0.01$). Both Chopard et al. (2010) and Leschka et al. (2010) only found significant differences in attenuation between the calcified and non-calcified lesions ($p < 0.05$ and $p < 0.001$ respectively), but not between lipid-rich and fibrotic lesions.

3.3 Materials

According to literature, the following six TMM's are nowadays widely used for the fabrication of soft tissue phantoms (P. Li et al., 2018; McGarry et al., 2020; Rajeshkumar et al., 2020):

- Agar
- Agarose
- Gelatine
- Polyvinyl alcohol (PVA)
- Polyvinyl chloride (PVC)
- Silicone

These TMM's can be classified as biopolymers or synthetic polymers. Biopolymer-based (i.e., agar, agarose and gelatine) materials commonly have high fractions of water. Because of this, they have relatively similar mechanical properties to soft tissues (McGarry et al., 2020). However, these high water contents make the TMM's prone to bacterial growth and dehydration (McGarry et al., 2020; Rajeshkumar et al., 2020). Bacterial growth can be prevented by irradiating a phantom and thereby sterilizing it, or utilizing an antifungal agent such as benzalkonium chloride (De Brabandere et al., 2006; Souza et al., 2016). Dehydration of the TMM could be prevented or decelerated by storing the phantom properly. For example, one could store an agar phantom in distilled water for up to three months with minimal changes in mechanical properties (Manickam et al., 2014b).

PVA is a synthetic polymer, but unlike the other synthetic polymers (i.e., PVC and silicone), it is dissolved in water to fabricate a TMM. It therefore shares a lot of its properties with the biopolymers. Both PVC and silicone based TMM's are generally more stable over time, since they are not dissolved in water. The downside of these materials is that their mechanical properties, such as the friction coefficient, differ more from that of soft tissues compared to the materials that are dissolved in water (W. Li et al., 2016). Both biopolymers and synthetic polymers can be mixed with additives, to modify the properties of the TMM. For instance, barium sulphate or calcium carbonate can be used to increase the x-ray attenuation of a TMM (Lai et al., 2022; Litt & Brody, 2001; Sun et al., 2021).

Agar and agarose

Agar is a biopolymer derived from algae and is used for a wide range of applications across multiple professional fields. For the development of a phantom, agar is typically dissolved in deionized water and poured into a mould. The concentration of agar in a solution has a significant impact on the elastic modulus of the material. Manickam et al. (2014a) conducted uniaxial compression tests on multiple TMM samples, with varying concentrations of agar. A strain rate of 0.5 mm/min was utilized during the uniaxial tests and the Young's moduli were determined in the initial linear region of the engineering stress-strain curves. The agar concentrations ranged from 1.7 to 6.6 wt% and the elastic modulus increased from 50 to 450 kPa respectively. Samples with a higher concentration of agar were not included in the study, since they were too brittle to withstand the maximum strain of 15% applied throughout the measurements.

Agarose is one of the two main components that make up agar, the other being agarpectin. Similar to agar, agarose is typically dissolved in deionized water. Furthermore, a TMM made from agarose also becomes stiffer and more brittle with increasing concentrations of agarose (Teixeira & Martins, 2020). Subhash et al. (2011) conducted measurements of different agarose samples, using a uniaxial tensile testing setup. The samples had agarose concentrations ranging from 1.5 to 4.0 wt% and the elastic modulus increased from approximately 0.2 to 1.0 MPa. However, unlike the elastic modulus, the HU value exhibits only slight changes with increasing concentrations of agarose. Litt and Brody (2001)

demonstrated that the HU value ranged from approximately 20 to 35 HU for samples with agarose concentrations of 0.7 to 6.0 wt%.

Gelatine

Gelatine is commonly derived from collagen through a process known as hydrolysis. For many, gelatine might be known as a thickening agent used in the food industry, but it is also frequently used for the fabrication of phantoms. Like all the other biopolymers, gelatine is typically dissolved in deionized water and the elastic modulus of a sample increases as the concentration of gelatine increases. Shaaer et al. (2021) employed ultrasound elastography to determine the Young's modulus of multiple samples with varying concentrations of gelatine. The study found that the stiffness ranged from 7 up to 100 kPa for samples with 3 to 12 g of gelatine per 100 ml of water. However, these samples also contained small amounts of graphite and it is unknown what effect this may have had on the findings. Another study, conducted by Hall et al. (1997), found comparable results by measuring the elastic modulus using a uniaxial compression test. The elastic modulus ranged from 4.8 up to 158 kPa for gelatine concentrations from 30 g/L up to 180 g/L. In addition to gelatine, these samples contained formaldehyde, which was shown to increase the stiffness of the tested samples. Finally, Anugrah et al. (2020) demonstrated that the CT numbers, measured with a tube potential of 120 kV, for composite hydrogels containing 16 to 28% gelatine were approximately 80 HU. Besides gelatine, these composites also consisted of PVA and particle board.

PVA

PVA is the only synthetic polymer included in this list that is dissolved in water in order to fabricate a TMM. It therefore shares a lot of its properties with the biopolymers. Two important parameters that influence the stiffness of a TMM made from PVA, are the concentration of PVA in the solution and the number of freeze-thaw cycles. An increase in either one of these parameters results in an increase of the stiffness. Malone et al. (2020) conducted uniaxial tensile tests of 10 and 15 wt% PVA samples that underwent two freeze-thaw cycles. The Young's modulus was determined based on the initial linear section of the engineering stress-strain curves. The elastic modulus was found to be approximately 62 kPa for the 10 wt% sample, while this increased to a mean of 320 kPa for the 15 wt% samples. Lai et al. (2022) measured the X-ray attenuation of 4% PVA solutions. The average attenuation value of these samples was 3 HU. Based on the article, it is unclear which CT scan parameters were used during these measurements.

PVC

A TMM based on PVC typically comprises a mixture of PVC and a softener, such as diethyl hexyl adipate or dioctyl terephthalate. Hungr et al. (2012) measured the elastic modulus in compression of various premixed polymer-softener mixtures, from which the exact mixing ratio was not provided by their supplier. The stiffest mixture was found to have a Young's modulus of 200 kPa, based on the initial linear section of the stress-strain curve. The Hounsfield units ranged from -20 for the softest mixture to 110 for the second stiffest mixture. He et al. (2019) also conducted uniaxial measurements of PVC samples, but unlike Hungr et al. (2012), they prepared their own polymer-softener solutions and measured the elastic modulus in tension. It was found that the elastic modulus increased from 7.65 to 12.38 MPa as the PVC-softener ratios increased from 10.9 to 16.7 g of PVC per 100 ml of softener. A tube voltage of 120 kV was utilized, to determine the CT number of the PVC samples. It was found that the HU value increased from -10 to 110 as the PVC-softener ratios increased from 7.9 to 23.1 g of PVC per 100 ml of softener.

Silicone

There are many different types of silicone available, covering a wide range of mechanical properties. An important mechanical property that indicates the hardness of a silicone, is the shore value. Although there is no unique and exact relationship between the shore value and the elastic modulus, an estimation can be made based on the results of different studies. Some studies that can be used for this purpose are those by Gent (1958), Meththananda et al. (2009) and Qi et al. (2003). Based on these studies, one could conclude that the different types of silicone also cover a wide range of elastic moduli (i.e., less than 1 MPa to well over 10 MPa). Some studies have measured the elastic modulus of a silicone directly. For example, Engers et al. (2020) used a silicone known as 'Dragon Skin 30' to fabricate a vein for a venepuncture phantom. The Young's modulus of this materials was determined to be 797 kPa. Another study measured the X-ray attenuation expressed as a Hounsfield unit of a platinum-cured silicone. These measurements were conducted with a tube potential of 120 kV and the results showed that the material had a HU value of 65 (Mørup et al., 2022).

4. DISCUSSION

The aim of this chapter is to critically evaluate and merge the findings presented in the previous chapter. Through this process, potential topics for future research and improvements have been identified. This information is especially suitable for researcher that are going to conduct future studies on mechanical and imaging properties of human coronary arteries. Furthermore, the limitations of this review and their implications for the interpretation of the results are also discussed.

4.1 Mechanical properties

When testing the mechanical properties of biological tissues, it is important to ensure that the ex vivo tissues closely resemble the in vivo properties. The studies included in this literature review employed several measures to maintain the in vivo mechanical properties and increase the repeatability of the measurements. For instance, most studies minimized the time between excision and measurement, as prolonged refrigeration time has a significant influence on the elastic modulus of arterial tissue (Stemper et al., 2007). It was also common practice to minimize the time between passing of the donor and excision. Furthermore, the included studies commonly prevented the samples from dehydrating throughout testing, by spraying or fully immersing them in a saline solution. Karimi et al. (2017a) showed that strain rate can also have a significant effect on the elastic modulus of atherosclerotic human coronary arteries during uniaxial tensile testing. As such, it is beneficial that all included studies used slow and comparable strain rates. Additionally, preconditioning routines were frequently employed to ensure repeatable results.

Longitudinal direction

Despite the measures described above, it remains very difficult to compare the results of different studies directly. One reason for this is the existence of different definitions for stress and strain. For instance, true stress values are always higher than their engineering equivalent, while true strain values are lower than their engineering equivalent. Consequently, elastic moduli calculated using true stress and strain values are higher than those calculated using engineering stress and strain values. Since both healthy and atherosclerotic human coronary arteries can be considered incompressible, it is not difficult to approximate the true stress values during uniaxial tensile tests (Karimi et al., 2016). Moreover, the strain in tensile testing of coronary arteries can become quite large, thus making true strain the more accurate definition to use. It might therefore be beneficial to standardize the use of true stress and strain when conducting uniaxial tensile tests of coronary arteries in future studies.

Arteries exhibit a nonlinear stress-strain relationship, which makes it difficult to compare Young's moduli across different studies. This is due to the fact that each study can calculate the moduli at different stress or strain levels, resulting in varying values. According to literature, the nonlinear stress-strain curve obtained from tensile testing arteries commonly has a J-shape (Claes et al., 2010). One could differentiate between two regions within this curve, an initial compliant and almost linear region at lower strain values and a stiffer region at higher strain values (Holzapfel, 2006). Jankowska et al. (2015) determined the elastic moduli in both the low and high stiffness region. It is assumed that the physiological moduli determined by Karimi et al. (2013) are based on the low stiffness region, while the maximum moduli are based on the high stiffness region. The other three studies determined their elastic moduli based on the initial section of the curve. As such, these moduli are considered to be determined in the low stiffness region.

The elastic moduli in the longitudinal direction of healthy and atherosclerotic human coronary arteries found in literature ranged from 0.28 to 20.96 MPa and 0.4 to 14.27 MPa respectively. For further analyses and discussion, certain results will be excluded from these ranges. First, the results based on

a single healthy sample of Jankowska et al. (2015) will be excluded, due to the small sample size and high value of the measured modulus. Second, the measurement conducted by Karimi et al. (2017a) of an atherosclerotic coronary artery at a strain rate of 50 mm/min is excluded. This is based on the conclusion that such a high strain rate has a significant impact on the measured results of atherosclerotic coronary arteries (Karimi et al., 2017a). Finally, the results of Karimi et al. (2017b) are also assumed to be outliers, since the found moduli are more than twice as large as the next largest modulus. The article has been thoroughly checked for possible reasons that could explain these results, but none were found. Therefore, it was determined to exclude this study as well. The elastic moduli in the longitudinal direction of healthy and atherosclerotic human coronary arteries found in the remaining literature ranged from 0.28 to 2.94 MPa and 0.4 to 5.63 MPa respectively. These ranges include results that are based on the low and high stiffness region of coronary arteries.

Circumferential direction

In order to calculate the circumferential stress based on the results of a distensibility test, either an equation for thin or thick-walled cylinders could be used. The equation for thin-walled cylinders is generally utilized when the ratio between the diameter and the thickness of the wall is greater than 20. If this ratio is less than 20, the variation of circumferential stress in the radial direction of the wall is assumed to be significant. Since coronary arteries commonly have a diameter to wall thickness ratio of less than 20, the equation for thick-walled cylinders would be better suited for calculating the circumferential stress (Dodge et al., 1992; Fayad et al., 2000; Gradus-Pizlo et al., 2003; Raut et al., 2017). It is unclear why Kasjanovs et al. (1999) utilized the thin-walled equation for calculating the circumferential stresses, but this can be considered as a valid point of criticism.

The elastic moduli in the circumferential direction of healthy and atherosclerotic human coronary arteries found in literature ranged from 0.78 to 4.14 MPa and 1.13 to 15.38 MPa respectively. However, the results of Karimi et al. (2017b) will be excluded from these ranges, since the moduli were more than twice as large as the next largest modulus. Based on the remaining literature, the elastic moduli in the circumferential direction of healthy and atherosclerotic human coronary arteries ranged from 0.78 to 1.64 MPa and 1.13 to 4.11 MPa respectively.

The findings suggest that atherosclerotic human coronary arteries are generally stiffer than healthy ones in both the longitudinal and circumferential direction, although there is an overlap between the ranges of the two groups. This is consistent with the results found by Karimi et al. (2013) and Karimi et al. (2017b). However, it should be noted that the age difference between the healthy and atherosclerotic groups in these studies was quite large. This could have influenced the results, since arterial stiffness also increases with age, independently of atherosclerotic disease (Boesen et al., 2015; Tajaddini et al., 2005). In contrast, Karimi et al. (2019) concluded that healthy coronary arteries are stiffer than atherosclerotic ones. Therefore, caution should be exercised when interpreting these results. Nevertheless, a large review study does show that atherosclerotic carotid arteries are significantly stiffer than healthy carotid arteries (Boesen et al., 2015). These combined findings, might suggest that atherosclerotic coronary arteries are indeed stiffer than healthy ones. This assumption could be used by researchers during the development of a coronary artery network phantom. However, one should have some reservation regarding this statement and always evaluate their phantom through expert judgement.

4.2 Imaging properties

All the included studies that measured the HU value of ex vivo tissue, classified the lesions using histopathological analysis. This method for classifying lesions is generally considered to be the gold standard for post-mortem classification (Chopard et al., 2010; Halliburton et al., 2006; Henzler et al., 2011; Nikolaou et al., 2004; Obaid et al., 2013; Schroeder et al., 2004). Only one of the included studies measured the imaging properties of in vivo tissue. In such a case, it is not possible to classify the lesion using histopathological analysis. Instead, VH-IVUS was utilized to classify these lesions. In a second part of the study, ex vivo tissue was classified using both VH-IVUS and histopathological analysis to compare the results and determine the accuracy of VH-IVUS. The findings indicated that VH-IVUS was able to correctly identify lesions with an accuracy equal to or greater than 74%, depending on the type of lesion. While this is a reasonable level of accuracy, it could still have impacted the results of the study. For instance, the study found significant differences in HU values among the three types of lesions during in vivo measurements ($p < 0.01$). Perhaps this result is due to the limited accuracy of VH-IVUS.

There are different parameters that can influence the measured HU value during a CT scan. Previous studies have found that the tube potential, tube current, use of contrast agent and type of reconstruction kernel can all have a significant effect on the degree of attenuation (Achenbach et al., 2010; Afifi et al., 2020; Barreto et al., 2008; Cademartiri et al., 2005, 2007; Davis et al., 2018a; Halliburton et al., 2006). In order to increase the comparability of the results, only studies that utilized a tube potential of 120 kV were included in this review. Additionally, at such a high tube potential the tube current seems to have a minimal effect on the measured attenuation value (Afifi et al., 2020). The effect of the different reconstruction kernels was not considered in this review. However, by comparing the results of different studies and the findings in this review, it is assumed that the influence of the reconstruction kernel on the attenuation value is relatively minor. Gantry rotation time and collimation were also not considered in this review, as they did not have a significant influence on the measured results (Davis et al., 2018b; Jeong et al., 2019). It should be noted that, despite the efforts made to identify the main parameters that influence the attenuation values during a CT scan, there remains the possibility that other relevant parameters may have been overlooked.

Based on the found mean and median HU values, the ranges for lipid-rich, fibrotic and calcified lesions were 23.1 to 104 HU, 27.1 to 106 HU and 234.9 to 1160 HU respectively. The results of the noncalcified and mixed calcified group from the study conducted by Halliburton et al. (2006) were excluded from these ranges, since they did not correspond to the preferred categorization used in this review. One could also consider the ranges without including the results from Tanami et al. (2010) and the pre-enhanced densely calcified results from Halliburton et al. (2006), since the use of contrast agent significantly influences the measurements. In that case, the ranges for lipid-rich, fibrotic and calcified lesions would be 34 to 104 HU, 67 to 106 HU and 377.2 to 1160 HU respectively. These ranges are considered throughout further discussion.

Five of the included studies reported a significant difference between the HU values for non-calcified and calcified lesions, which is also evident from the findings in this review. None of the included studies contradicted these results. However, the literature is not as clear about the difference in HU values between lipid-rich and fibrotic lesions. Both Galonska et al. (2008) and Obaid et al. (2013) reported significantly lower HU values for lipid-rich lesions compared to fibrotic ones. In contrast, Tanami et al. (2010), Chopard et al. (2010) and Leschka et al. (2010) did not find significant differences between the two types of lesions. The results in this review also showed a large overlap in HU values between the two groups, although the average value is somewhat higher for the fibrotic group. These results suggests that the HU value of fibrotic lesions might be significantly larger than that of lipid-rich ones, however the difference would be rather small.

4.3 Materials

Before discussing the different materials included in this review, it is important to note that the information presented in this section is by no means complete and should therefore only serve as a guidance or starting point for further research. For example, only six different materials have been considered in this review. Although these six materials are widely used for the development of soft tissue phantoms, there are other materials and many additives that one could also consider. Furthermore, some studies even developed composite hydrogels in order to combine properties of different materials. Another limitation of this review, is the fact that the fabrication process of the materials has not been considered. Parameters such as temperature, time and mixing rates may influence the imaging and mechanical properties of a material. Finally, the information in this review was limited by the available literature. For instance, no literature was found on the elastic modulus of samples with a PVA concentration of more than 15%. This deficiency of literature can make it difficult or even impossible to draw conclusions, but it also creates opportunities for future research.

The found HU values for the various materials were all within the acceptable range to mimic lipid-rich and fibrotic lesions. Not all included studies explicitly stated the CT parameters, specifically the tube potential and tube current, that were used during the measurements. However, the tube potential and tube current do not seem to have a large influence on HU values between -20 and 110, as were included in this study (Afifi et al., 2020). No literature was found on the HU value of an agar solution. Since agarose is one of the two main components of agar, it is assumed that their X-ray attenuation values are comparative. There was also no literature found on the HU value of a gelatine and water mixture. Instead, a study that measured the attenuation of a composite hydrogel containing 16 to 28% gelatine was included. Again, it was assumed that the results of this study resembled the HU value of a gelatine and water mixture sufficiently. In order to mimic calcified lesions with the materials included in this review, one should increase the attenuation values by using an additive such as barium sulphate or calcium carbonate.

Agar and agarose can be used to mimic the elastic moduli in longitudinal direction of healthy and atherosclerotic human coronary arteries. Agarose could even be used to mimic the elastic modulus in circumferential direction of healthy coronary arteries. However, it is likely not practicable to increase the elastic moduli of an agar or agarose solutions beyond the values stated in this review by only increasing their concentrations, since both would become too brittle (Manickam et al., 2014a; Teixeira & Martins, 2020). The found stiffness ranges for gelatine were not high enough to mimic any of the elastic moduli of either healthy or atherosclerotic coronary arteries. Even the samples that contained formaldehyde, which increases the stiffness, were not stiff enough. It is unknown whether increasing the gelatine concentrations beyond that of the included studies will lead to adverse effects.

The stiffest PVA sample found in literature contained 15 wt% PVA, had undergone two freeze-thaw cycles and its elastic modulus was 320 kPa. This would only be sufficient to mimic the elastic modulus in the longitudinal direction of healthy coronary arteries. Nevertheless, the stiffness of PVA solutions increases with the number of freeze-thaw cycles. For example, Malone et al. (2020) showed that the stiffness of a 10 wt% PVA sample can be increased by more than 100%, by increasing the number of freeze-thaw cycles from 2 to 6. Based on this, one could assume that with a sufficient number of freeze-thaw cycles, a 15 wt% PVA sample could also be used to mimic the elastic modulus in the longitudinal direction of an atherosclerotic coronary artery. Finally, only PVC and silicone could be used to mimic the complete ranges of elastic moduli in longitudinal and circumferential direction of healthy and atherosclerotic arteries. These are also the only two materials included in this review that are not dissolved in water when fabricating the TMM.

5. CONCLUSION

An anthropomorphic coronary artery network phantom could be a beneficial tool during the development and pre-clinical trials of a novel medical instrument developed for percutaneous coronary intervention. The aim of this review was to provide researchers with an overview of different tissue mimicking materials that could be used throughout the development of such a phantom, by answering the following research question:

What different tissue mimicking materials can be used in the development of an anthropomorphic coronary artery network phantom, designed for testing novel medical instruments and technologies developed for (complex) PCI?

There were three sub-questions formulated, that would assist with answering the main question. The first sub-question focused on the mechanical properties of healthy and atherosclerotic human coronary arteries:

What is the elastic modulus in longitudinal and circumferential direction of healthy and atherosclerotic human coronary arteries?

Based on the found literature, the elastic moduli in longitudinal direction of healthy and atherosclerotic human coronary arteries ranged from 0.28 to 2.94 MPa and 0.4 to 5.63 MPa respectively. The elastic moduli in circumferential direction of both healthy and atherosclerotic coronary arteries ranged from 0.78 to 1.68 MPa and 1.13 to 4.11 MPa respectively. The second sub-question focused on the imaging properties of atherosclerotic coronary arteries:

What is the degree of X-ray attenuation, expressed as a Hounsfield Unit, of atherosclerotic human coronary arteries?

The different types of atherosclerotic lesions were categorized as either lipid-rich, fibrotic or calcified. The Hounsfield units for these lesions ranged from 34 to 104 HU, 67 to 106 HU and from 377.2 to 1160 HU for lipid-rich, fibrotic and calcified lesions respectively. The aim of the third sub-questions was to provide an overview of tissue mimicking materials that are currently used for the development of soft issue phantoms and include information on both the elastic moduli and HU values for these materials:

What different tissue mimicking materials are currently used for the development of soft tissue phantoms?

Six different TMM's were addressed in this review, namely agar, agarose, gelatine, PVA, PVC and silicone. All included materials could be used to mimic the HU values of lipid-rich, fibrotic and calcified lesions. In the case of the latter, additives should be used to increase the HU values of the TMM's. Contrary to the imaging properties, not all materials were suited to mimic the in-vivo mechanical properties of human coronary arteries. Only PVC and silicone could be used to mimic the complete ranges of elastic moduli in longitudinal and circumferential direction of healthy and atherosclerotic arteries. Agar, agarose and PVA can all be used to mimic the elastic moduli in longitudinal direction of healthy and atherosclerotic human coronary arteries. Agarose can also mimic the elastic modulus in circumferential direction of healthy coronary arteries. Gelatine was the only included material that had insufficient mechanical properties to mimic the elastic moduli of the healthy and atherosclerotic coronary arteries in any direction.

Based on all the results, the main research question can be answered. Silicone, PVC, PVA, agar and agarose can all be used for the development of an anthropomorphic coronary network phantom with realistic mechanical and imaging properties. PVA, agar and agarose are probably the more favourable

options from a mechanical point of view, since they commonly have high fractions of water. As such, they generally have comparable mechanical properties to soft tissues (McGarry et al., 2020). As a final remark it is important to note that the information in this review is by no means complete. The list of possible materials and ways of processing them is too extensive to consider it all. Furthermore, the information in this review was also limited by the available literature. This review should therefore only serve as a guidance or starting point for researchers, and further in-depth research on specific materials might be required.

REFERENCES

- Achenbach, S., Boehmer, K., Pflederer, T., Ropers, D., Seltmann, M., Lell, M., Anders, K., Kuettner, A., Uder, M., Daniel, W. G., & Marwan, M. (2010). Influence of slice thickness and reconstruction kernel on the computed tomographic attenuation of coronary atherosclerotic plaque. *Journal of Cardiovascular Computed Tomography*, 4(2), 110–115. <https://doi.org/https://doi.org/10.1016/j.jcct.2010.01.013>
- Afifi, M. B., Abdelrazek, A., Deiab, N. A., Abd El-Hafez, A. I., & El-Farrash, A. H. (2020). The effects of CT x-ray tube voltage and current variations on the relative electron density (RED) and CT number conversion curves. *Journal of Radiation Research and Applied Sciences*, 13(1), 1–11. <https://doi.org/https://doi.org/10.1080/16878507.2019.1693176>
- Anugrah, M. A., Suryani, S., Ilyas, S., Mutmainna, I., Fahri, A. N., Jusmawang, & Tahir, D. (2020). Composite gelatin/Rhizophora SPP particleboards/PVA for soft tissue phantom applications. *Radiation Physics and Chemistry*, 173, 108878. <https://doi.org/https://doi.org/10.1016/j.radphyschem.2020.108878>
- Barreto, M., Schoenhagen, P., Nair, A., Amatangelo, S., Milite, M., Obuchowski, N. A., Lieber, M. L., & Halliburton, S. S. (2008). Potential of dual-energy computed tomography to characterize atherosclerotic plaque: ex vivo assessment of human coronary arteries in comparison to histology. *Journal of Cardiovascular Computed Tomography*, 2(4), 234–242. <https://doi.org/https://doi.org/10.1016/j.jcct.2008.05.146>
- Boesen, M. E., Singh, D., Menon, B. K., & Frayne, R. (2015). A systematic literature review of the effect of carotid atherosclerosis on local vessel stiffness and elasticity. *Atherosclerosis*, 243(1), 211–222. <https://doi.org/https://doi.org/10.1016/j.atherosclerosis.2015.09.008>
- Burris, A. C., & Shoukfeh, M. (2015). Basic Coronary Artery Anatomy and Histology. In A. E. Abbas (Ed.), *Interventional Cardiology Imaging: An Essential Guide* (pp. 1–12). Springer London. https://doi.org/10.1007/978-1-4471-5239-2_1
- Cademartiri, F., La Grutta, L., Runza, G., Palumbo, A., Maffei, E., Mollet, N. R. A., Bartolotta, T. V., Somers, P., Knaapen, M., Verheye, S., Midiri, M., Hamers, R., & Bruining, N. (2007). Influence of convolution filtering on coronary plaque attenuation values: observations in an ex vivo model of multislice computed tomography coronary angiography. *European Radiology*, 17(7), 1842–1849. <https://doi.org/10.1007/s00330-006-0548-z>
- Cademartiri, F., Mollet, N. R., Runza, G., Bruining, N., Hamers, R., Somers, P., Knaapen, M., Verheye, S., Midiri, M., Krestin, G. P., & de Feyter, P. J. (2005). Influence of intracoronary attenuation on coronary plaque measurements using multislice computed tomography: observations in an ex vivo model of coronary computed tomography angiography. *European Radiology*, 15(7), 1426–1431. <https://doi.org/10.1007/s00330-005-2697-x>
- Chopard, R., Bussel, L., Motreff, P., Rioufol, G., Tabib, A., Douek, P., Meyronet, D., Revel, D., & Finet, G. (2010). How reliable are 40 MHz IVUS and 64-slice MDCT in characterizing coronary plaque composition? An ex vivo study with histopathological comparison. *The International Journal of Cardiovascular Imaging*, 26(4), 373–383. <https://doi.org/10.1007/s10554-009-9562-y>
- Claes, E., Atienza, J. M., Guinea, G. V, Rojo, F. J., Bernal, J. M., Revuelta, J. M., & Elices, M. (2010). Mechanical properties of human coronary arteries. *2010 Annual International Conference of the*

IEEE Engineering in Medicine and Biology, 3792–3795.
<https://doi.org/10.1109/IEMBS.2010.5627560>

- Davis, A. T., Palmer, A. L., Pani, S., & Nisbet, A. (2018a). Assessment of the variation in CT scanner performance (image quality and Hounsfield units) with scan parameters, for image optimisation in radiotherapy treatment planning. *Physica Medica*, 45, 59–64.
<https://doi.org/10.1016/j.ejmp.2017.11.036>
- Davis, A. T., Palmer, A. L., Pani, S., & Nisbet, A. (2018b). Assessment of the variation in CT scanner performance (image quality and Hounsfield units) with scan parameters, for image optimisation in radiotherapy treatment planning. *Physica Medica*, 45, 59–64.
<https://doi.org/10.1016/j.ejmp.2017.11.036>
- De Brabandere, M., Kirisits, C., Peeters, R., Haustermans, K., & Van den Heuvel, F. (2006). Accuracy of seed reconstruction in prostate postplanning studied with a CT- and MRI-compatible phantom. *Radiotherapy and Oncology*, 79(2), 190–197.
<https://doi.org/https://doi.org/10.1016/j.radonc.2006.04.009>
- Dodge, J. T., Brown, B. G., Bolson, E. L., & Dodge, H. T. (1992). Lumen diameter of normal human coronary arteries. Influence of age, sex, anatomic variation, and left ventricular hypertrophy or dilation. *Circulation*, 86(1), 232–246. <https://doi.org/10.1161/01.CIR.86.1.232>
- Duprey, A., Khanafer, K., Schlicht, M., Avril, S., Williams, D., & Berguer, R. (2010). In Vitro Characterisation of Physiological and Maximum Elastic Modulus of Ascending Thoracic Aortic Aneurysms Using Uniaxial Tensile Testing. *European Journal of Vascular and Endovascular Surgery*, 39(6), 700–707. <https://doi.org/https://doi.org/10.1016/j.ejvs.2010.02.015>
- Engers, M., Stewart, K. W., Liu, J., & Pott, P. P. (2020). Development of a realistic venepuncture phantom. *Current Directions in Biomedical Engineering*, 6(3), 402–405.
<https://doi.org/10.1515/cdbme-2020-3104>
- Fayad, Z. A., Fuster, V., Fallon, J. T., Jayasundera, T., Worthley, S. G., Helft, G., Aguinaldo, J. G., Badimon, J. J., & Sharma, S. K. (2000). Noninvasive In Vivo Human Coronary Artery Lumen and Wall Imaging Using Black-Blood Magnetic Resonance Imaging. *Circulation*, 102(5), 506–510.
<https://doi.org/10.1161/01.CIR.102.5.506>
- Feuchtner, G. M., Jodocy, D., Klauser, A., Haberfellner, B., Aglan, I., Spoeck, A., Hiehs, S., Soegner, P., & Jaschke, W. (2010). Radiation dose reduction by using 100-kV tube voltage in cardiac 64-slice computed tomography: A comparative study. *European Journal of Radiology*, 75(1), e51–e56.
<https://doi.org/https://doi.org/10.1016/j.ejrad.2009.07.012>
- Galonska, M., Ducke, F., Kertesz-Zborilova, T., Meyer, R., Guski, H., & Knollmann, F. D. (2008). Characterization of Atherosclerotic Plaques in Human Coronary Arteries With 16-Slice Multidetector Row Computed Tomography by Analysis of Attenuation Profiles. *Academic Radiology*, 15(2), 222–230. <https://doi.org/https://doi.org/10.1016/j.acra.2007.09.007>
- Gent, A. N. (1958). On the Relation between Indentation Hardness and Young's Modulus. *Rubber Chemistry and Technology*, 31(4), 896–906. <https://doi.org/10.5254/1.3542351>
- Gradus-Pizlo, I., Bigelow, B., Mahomed, Y., Sawada, S. G., Rieger, K., & Feigenbaum, H. (2003). Left anterior descending coronary artery wall thickness measured by high-frequency transthoracic and epicardial echocardiography includes adventitia. *The American Journal of Cardiology*, 91(1), 27–32. [https://doi.org/https://doi.org/10.1016/S0002-9149\(02\)02993-4](https://doi.org/https://doi.org/10.1016/S0002-9149(02)02993-4)

- Hall, T. J., Bilgen, M., Insana, M. F., & Krouskop, T. A. (1997). Phantom materials for elastography. *IEEE Transactions on Ultrasonics, Ferroelectrics and Frequency Control*, *44*(6), 1355–1365. <https://doi.org/10.1109/58.656639>
- Halliburton, S. S., Schoenhagen, P., Nair, A., Stillman, A., Lieber, M., Murat Tuzcu, E., Geoffrey Vince, D., & White, R. D. (2006). Contrast enhancement of coronary atherosclerotic plaque: a high-resolution, multidetector-row computed tomography study of pressure-perfused, human ex-vivo coronary arteries. *Coronary Artery Disease*, *17*(6). https://journals.lww.com/coronary-artery/Fulltext/2006/09000/Contrast_enhancement_of_coronary_atherosclerotic.9.aspx
- He, Y., Qin, S., Dyer, B. A., Zhang, H., Zhao, L., Chen, T., Zheng, F., Sun, Y., Shi, L., Rong, Y., & Qiu, J. (2019). Characterizing mechanical and medical imaging properties of polyvinyl chloride-based tissue-mimicking materials. *Journal of Applied Clinical Medical Physics*, *20*(7), 176–183. <https://doi.org/10.1002/acm2.12661>
- Henzler, T., Porubsky, S., Kayed, H., Harder, N., Krissak, U. R., Meyer, M., Sueselbeck, T., Marx, A., Michaely, H., Schoepf, U. J., Schoenberg, S. O., & Fink, C. (2011). Attenuation-based characterization of coronary atherosclerotic plaque: Comparison of dual source and dual energy CT with single-source CT and histopathology. *European Journal of Radiology*, *80*(1), 54–59. <https://doi.org/https://doi.org/10.1016/j.ejrad.2010.07.024>
- Holzapfel, G. A. (2006). Determination of material models for arterial walls from uniaxial extension tests and histological structure. *Journal of Theoretical Biology*, *238*(2), 290–302. <https://doi.org/https://doi.org/10.1016/j.jtbi.2005.05.006>
- Holzapfel, G. A., Sommer, G., Gasser, C. T., & Regitnig, P. (2005). Determination of layer-specific mechanical properties of human coronary arteries with nonatherosclerotic intimal thickening and related constitutive modeling. *American Journal of Physiology-Heart and Circulatory Physiology*, *289*(5), H2048–H2058. <https://doi.org/10.1152/ajpheart.00934.2004>
- Hung, N., Long, J.-A., Beix, V., & Troccaz, J. (2012). A realistic deformable prostate phantom for multimodal imaging and needle-insertion procedures. *Medical Physics*, *39*(4), 2031–2041. <https://doi.org/10.1118/1.3692179>
- Jankowska, M. A., Bartkowiak-Jowska, M., & Bedzinski, R. (2015). Experimental and constitutive modeling approaches for a study of biomechanical properties of human coronary arteries. *Journal of the Mechanical Behavior of Biomedical Materials*, *50*, 1–12. <https://doi.org/https://doi.org/10.1016/j.jmbbm.2015.05.021>
- Jeong, D.-K., Lee, S.-S., Kim, J.-E., Huh, K.-H., Yi, W.-J., Heo, M.-S., & Choi, S.-C. (2019). Effects of energy level, reconstruction kernel, and tube rotation time on Hounsfield units of hydroxyapatite in virtual monochromatic images obtained with dual-energy CT. *Imaging Science in Dentistry*, *49*(4), 273–279. <https://doi.org/10.5624/isd.2019.49.4.273>
- Karimi, A., Navidbakhsh, M., Shojaei, A., & Faghihi, S. (2013). Measurement of the uniaxial mechanical properties of healthy and atherosclerotic human coronary arteries. *Materials Science and Engineering: C*, *33*(5), 2550–2554. <https://doi.org/https://doi.org/10.1016/j.msec.2013.02.016>
- Karimi, A., Rahmati, S. M., Sera, T., Kudo, S., & Navidbakhsh, M. (2017a). A combination of experimental and numerical methods to investigate the role of strain rate on the mechanical

- properties and collagen fiber orientations of the healthy and atherosclerotic human coronary arteries. *Bioengineered*, 8(2), 154–170. <https://doi.org/10.1080/21655979.2016.1212134>
- Karimi, A., Rahmati, S. M., Sera, T., Kudo, S., & Navidbakhsh, M. (2017b). A Combination of Constitutive Damage Model and Artificial Neural Networks to Characterize the Mechanical Properties of the Healthy and Atherosclerotic Human Coronary Arteries. *Artificial Organs*, 41(9), E103–E117. <https://doi.org/https://doi.org/10.1111/aor.12855>
- Karimi, A., Razaghi, R., & Koyama, M. (2019). A patient-specific numerical modeling of the spontaneous coronary artery dissection in relation to atherosclerosis. *Computer Methods and Programs in Biomedicine*, 182, 105060. <https://doi.org/https://doi.org/10.1016/j.cmpb.2019.105060>
- Karimi, A., Sera, T., Kudo, S., & Navidbakhsh, M. (2016). Experimental verification of the healthy and atherosclerotic coronary arteries incompressibility via Digital Image Correlation. *Artery Research*, 16, 1–7. <https://doi.org/https://doi.org/10.1016/j.artres.2016.08.002>
- Kasjanovs, V., Ozolanta, I., & Purina, B. (1999). Features of biomechanical properties of human coronary arteries. *Mechanics of Composite Materials*, 35(2), 155–168. <https://doi.org/10.1007/BF02257246>
- Kural, M. H., Cai, M., Tang, D., Gwyther, T., Zheng, J., & Billiar, K. L. (2012). Planar biaxial characterization of diseased human coronary and carotid arteries for computational modeling. *Journal of Biomechanics*, 45(5), 790–798. <https://doi.org/https://doi.org/10.1016/j.jbiomech.2011.11.019>
- Lai, M., Skyrman, S., Kor, F., Homan, R., El-Hajj, V. G., Babic, D., Edström, E., Elmi-Terander, A., Hendriks, B. H. W., & de With, P. H. N. (2022). Development of a CT-Compatible, Anthropomorphic Skull and Brain Phantom for Neurosurgical Planning, Training, and Simulation. *Bioengineering*, 9(10), 537. <https://doi.org/10.3390/bioengineering9100537>
- Lawton, J. S., Tamis-Holland, J. E., Bangalore, S., Bates, E. R., Beckie, T. M., Bischoff, J. M., Bittl, J. A., Cohen, M. G., DiMaio, J. M., Don, C. W., Fremes, S. E., Gaudino, M. F., Goldberger, Z. D., Grant, M. C., Jaswal, J. B., Kurlansky, P. A., Mehran, R., Metkus, T. S., Nnacheta, L. C., ... Zwischenberger, B. A. (2022). 2021 ACC/AHA/SCAI Guideline for Coronary Artery Revascularization: A Report of the American College of Cardiology/American Heart Association Joint Committee on Clinical Practice Guidelines. *Journal of the American College of Cardiology*, 79(2), e21–e129. <https://doi.org/https://doi.org/10.1016/j.jacc.2021.09.006>
- Leschka, S., Seitun, S., Dettmer, M., Baumüller, S., Stolzmann, P., Goetti, R., Scheffel, H., Feuchtner, G., Wunnicke, K., Wildermuth, S., Oehlschlegel, C., Marincek, B., Jochum, W., & Alkadhi, H. (2010). Ex vivo evaluation of coronary atherosclerotic plaques: Characterization with dual-source CT in comparison with histopathology. *Journal of Cardiovascular Computed Tomography*, 4(5), 301–308. <https://doi.org/https://doi.org/10.1016/j.jcct.2010.05.016>
- Li, P., Yang, Z., & Jiang, S. (2018). Tissue mimicking materials in image-guided needle-based interventions: A review. *Materials Science and Engineering: C*, 93, 1116–1131. <https://doi.org/https://doi.org/10.1016/j.msec.2018.09.028>
- Li, W., Belmont, B., Greve, J. M., Manders, A. B., Downey, B. C., Zhang, X., Xu, Z., Guo, D., & Shih, A. (2016). Polyvinyl chloride as a multimodal tissue-mimicking material with tuned mechanical and

- medical imaging properties. *Medical Physics*, 43(10), 5577–5592.
<https://doi.org/10.1118/1.4962649>
- Litt, H. I., & Brody, A. S. (2001). BaSO₄-Loaded Agarose: A Construction Material for Multimodality Imaging Phantoms. *Academic Radiology*, 8(5), 377–383.
[https://doi.org/https://doi.org/10.1016/S1076-6332\(03\)80544-5](https://doi.org/https://doi.org/10.1016/S1076-6332(03)80544-5)
- Malone, A. J., Cournane, S., Naydenova, I. G., Fagan, A. J., & Browne, J. E. (2020). Polyvinyl alcohol cryogel based vessel mimicking material for modelling the progression of atherosclerosis. *Physica Medica*, 69, 1–8. <https://doi.org/https://doi.org/10.1016/j.ejmp.2019.11.012>
- Manickam, K., Machireddy, R. R., & Seshadri, S. (2014a). Characterization of biomechanical properties of agar based tissue mimicking phantoms for ultrasound stiffness imaging techniques. *Journal of the Mechanical Behavior of Biomedical Materials*, 35, 132–143.
<https://doi.org/https://doi.org/10.1016/j.jmbbm.2014.03.017>
- Manickam, K., Machireddy, R. R., & Seshadri, S. (2014b). Study of ultrasound stiffness imaging methods using tissue mimicking phantoms. *Ultrasonics*, 54(2), 621–631.
<https://doi.org/https://doi.org/10.1016/j.ultras.2013.08.018>
- McGarry, C. K., Grattan, L. J., Ivory, A. M., Leek, F., Liney, G. P., Liu, Y., Miloro, P., Rai, R., Robinson, A., Shih, A. J., Zeqiri, B., & Clark, C. H. (2020). Tissue mimicking materials for imaging and therapy phantoms: a review. *Physics in Medicine & Biology*. <https://doi.org/10.1088/1361-6560/abbd17>
- Meththananda, I. M., Parker, S., Patel, M. P., & Braden, M. (2009). The relationship between Shore hardness of elastomeric dental materials and Young's modulus. *Dental Materials*, 25(8), 956–959. <https://doi.org/https://doi.org/10.1016/j.dental.2009.02.001>
- Mørup, S. D., Stowe, J., Precht, H., Gervig, M. H., & Foley, S. (2022). Design of a 3D printed coronary artery model for CT optimization. *Radiography*, 28(2), 426–432.
<https://doi.org/https://doi.org/10.1016/j.radi.2021.09.001>
- Neumann, F.-J., Sousa-Uva, M., Ahlsson, A., Alfonso, F., Banning, A. P., Benedetto, U., Byrne, R. A., Collet, J.-P., Falk, V., Head, S. J., Jüni, P., Kastrati, A., Koller, A., Kristensen, S. D., Niebauer, J., Richter, D. J., Seferović, P. M., Sibbing, D., Stefanini, G. G., ... Group, E. S. C. S. D. (2019). 2018 ESC/EACTS Guidelines on myocardial revascularization. *European Heart Journal*, 40(2), 87–165.
<https://doi.org/10.1093/eurheartj/ehy394>
- Nikolaou, K., Becker, C. R., Muders, M., Babaryka, G., Scheidler, J., Flohr, T., Loehrs, U., Reiser, M. F., & Fayad, Z. A. (2004). Multidetector-row computed tomography and magnetic resonance imaging of atherosclerotic lesions in human ex vivo coronary arteries. *Atherosclerosis*, 174(2), 243–252.
<https://doi.org/https://doi.org/10.1016/j.atherosclerosis.2004.01.041>
- Obaid, D. R., Calvert, P. A., Gopalan, D., Parker, R. A., Hoole, S. P., West, N. E. J., Goddard, M., Rudd, J. H. F., & Bennett, M. R. (2013). Atherosclerotic Plaque Composition and Classification Identified by Coronary Computed Tomography. *Circulation: Cardiovascular Imaging*, 6(5), 655–664.
<https://doi.org/10.1161/CIRCIMAGING.112.000250>
- Piccolo, R., Bona, K. H., Efthimiou, O., Varenne, O., Baldo, A., Urban, P., Kaiser, C., Remkes, W., Räber, L., de Belder, A., van 't Hof, A. W. J., Stankovic, G., Lemos, P. A., Wilsgaard, T., Reifart, J., Rodriguez, A. E., Ribeiro, E. E., Serruys, P. W. J. C., Abizaid, A., ... Valgimigli, M. (2019). Drug-eluting or bare-metal stents for percutaneous coronary intervention: a systematic review and

- individual patient data meta-analysis of randomised clinical trials. *The Lancet*, 393(10190), 2503–2510. [https://doi.org/https://doi.org/10.1016/S0140-6736\(19\)30474-X](https://doi.org/https://doi.org/10.1016/S0140-6736(19)30474-X)
- Qi, H. J., Joyce, K., & Boyce, M. C. (2003). Durometer Hardness and the Stress-Strain Behavior of Elastomeric Materials. *Rubber Chemistry and Technology*, 76(2), 419–435. <https://doi.org/10.5254/1.3547752>
- Rajeshkumar, G., Vishnupriyan, R., & Selvadeepak, S. (2020). Tissue Mimicking Material an Idealized Tissue Model for Clinical Applications: A Review. *Materials Today: Proceedings*, 22, 2696–2703. <https://doi.org/https://doi.org/10.1016/j.matpr.2020.03.400>
- Ralapanawa, U., & Sivakanesan, R. (2021). Epidemiology and the Magnitude of Coronary Artery Disease and Acute Coronary Syndrome: A Narrative Review. *Journal of Epidemiology and Global Health*, 11(2), 169. <https://doi.org/10.2991/jegh.k.201217.001>
- Raut, B. K., Patil, V. N., & Cherian, G. (2017). Coronary artery dimensions in normal Indians. *Indian Heart Journal*, 69(4), 512–514. <https://doi.org/10.1016/j.ihj.2017.01.009>
- Rezvani-Sharif, A., Tafazzoli-Shadpour, M., & Avolio, A. (2019). Progressive changes of elastic moduli of arterial wall and atherosclerotic plaque components during plaque development in human coronary arteries. *Medical & Biological Engineering & Computing*, 57(3), 731–740. <https://doi.org/10.1007/s11517-018-1910-4>
- Schroeder, S., Kuettner, A., Leitritz, M., Janzen, J., Kopp, A. F., Herdeg, C., Heuschmid, M., Burgstahler, C., Baumbach, A., Wehrmann, M., & Claussen, C. D. (2004). Reliability of Differentiating Human Coronary Plaque Morphology Using Contrast-Enhanced Multislice Spiral Computed Tomography: A Comparison With Histology. *Journal of Computer Assisted Tomography*, 28(4). https://journals.lww.com/jcat/Fulltext/2004/07000/Reliability_of_Differentiating_Human_Coronary.3.aspx
- Shaaer, A., Alrashidi, S., Chung, H., Loblaw, A., Morton, G., Paudel, M., Tseng, C.-L., & Ravi, A. (2021). Multipurpose ultrasound-based prostate phantom for use in interstitial brachytherapy. *Brachytherapy*, 20(6), 1139–1145. <https://doi.org/https://doi.org/10.1016/j.brachy.2021.07.003>
- Souza, R. M., Santos, T. Q., Oliveira, D. P., Souza, R. M., Alvarenga, A. V., & Costa-Felix, R. P. B. (2016). Standard operating procedure to prepare agar phantoms. *Journal of Physics: Conference Series*, 733, 012044. <https://doi.org/10.1088/1742-6596/733/1/012044>
- Sтары, H. C., Chandler, A. B., Dinsmore, R. E., Fuster, V., Glagov, S., Insull, W., Rosenfeld, M. E., Schwartz, C. J., Wagner, W. D., & Wissler, R. W. (1995). A Definition of Advanced Types of Atherosclerotic Lesions and a Histological Classification of Atherosclerosis. *Circulation*, 92(5), 1355–1374. <https://doi.org/10.1161/01.CIR.92.5.1355>
- Stemper, B. D., Yoganandan, N., Stineman, M. R., Gennarelli, T. A., Baisden, J. L., & Pintar, F. A. (2007). Mechanics of Fresh, Refrigerated, and Frozen Arterial Tissue. *Journal of Surgical Research*, 139(2), 236–242. <https://doi.org/10.1016/j.jss.2006.09.001>
- Subhash, G., Liu, Q., Moore, D. F., Ifju, P. G., & Haile, M. A. (2011). Concentration Dependence of Tensile Behavior in Agarose Gel Using Digital Image Correlation. *Experimental Mechanics*, 51(2), 255–262. <https://doi.org/10.1007/s11340-010-9354-2>

- Sun, Z., Ng, C. K. C., Wong, Y. H., & Yeong, C. H. (2021). 3D-Printed Coronary Plaques to Simulate High Calcification in the Coronary Arteries for Investigation of Blooming Artifacts. *Biomolecules*, *11*(9), 1307. <https://doi.org/10.3390/biom11091307>
- Tajaddini, A., Kilpatrick, D. L., Schoenhagen, P., Tuzcu, E. M., Lieber, M., & Vince, D. G. (2005). Impact of age and hyperglycemia on the mechanical behavior of intact human coronary arteries: an ex vivo intravascular ultrasound study. *American Journal of Physiology-Heart and Circulatory Physiology*, *288*(1), H250–H255. <https://doi.org/10.1152/ajpheart.00646.2004>
- Tanami, Y., Ikeda, E., Jinzaki, M., Satoh, K., Nishiwaki, Y., Yamada, M., Okada, Y., & Kuribayashi, S. (2010). Computed Tomographic Attenuation Value of Coronary Atherosclerotic Plaques With Different Tube Voltage: An Ex Vivo Study. *Journal of Computer Assisted Tomography*, *34*(1). https://journals.lww.com/jcat/Fulltext/2010/01000/Computed_Tomographic_Attenuation_Value_of_Coronary.11.aspx
- Teixeira, A. M., & Martins, P. (2020). Mechanical characterisation of an organic phantom candidate for breast tissue. *Journal of Biomaterials Applications*, *34*(8), 1163–1170. <https://doi.org/10.1177/0885328219895738>
- van Andel, C. J., Pistecky, P. V., & Borst, C. (2003). Mechanical properties of porcine and human arteries: implications for coronary anastomotic connectors. *The Annals of Thoracic Surgery*, *76*(1), 58–64. [https://doi.org/https://doi.org/10.1016/S0003-4975\(03\)00263-7](https://doi.org/https://doi.org/10.1016/S0003-4975(03)00263-7)
- Zhang, G., Yu, C., Zhou, M., Wang, L., Zhang, Y., & Luo, L. (2018). Burden of Ischaemic heart disease and attributable risk factors in China from 1990 to 2015: findings from the global burden of disease 2015 study. *BMC Cardiovascular Disorders*, *18*(1), 18. <https://doi.org/10.1186/s12872-018-0761-0>